

**A NANO-HILIC-MS PLATFORM FOR SEPARATION AND  
CHARACTERIZATION OF GLYCOPROTEINS**

by

**Charles Robert Bupp II**

**A Dissertation**

*Submitted to the Faculty of Purdue University*

*In Partial Fulfillment of the Requirements for the degree of*

**Doctor of Philosophy**



Department of Chemistry

West Lafayette, Indiana

August 2020

**THE PURDUE UNIVERSITY GRADUATE SCHOOL**  
**STATEMENT OF COMMITTEE APPROVAL**

**Dr. Mary Wirth, Chair**

Department of Chemistry

**Dr. Kavita Shah**

Department of Chemistry

**Dr. Scott McLuckey**

Department of Chemistry

**Dr. Hilkka Kenttämää**

Department of Chemistry

**Approved by:**

Dr. Christine Hrycyna

*To my best friend and loving wife, Abriti*

## ACKNOWLEDGMENTS

First and foremost, I would like to thank my Advisor, Professor Mary J. Wirth, for her constant support and patient mentoring. Through her guidance, I learned more about analytical chemistry than I could have possibly imagined.

I owe a debt of gratitude to Professor Pete Palmer for converting me from a budding biochemist to a diehard analytical chemist, and for the guidance he has provided through my undergraduate years and beyond.

I would like to thank the other members of my thesis committee, Professors Kavita Shah, Scott McLuckey, and Hilkka Kenttämä for their time and their assistance.

I have been fortunate enough to work with many talented, knowledgeable, and friendly individuals during my time in the Wirth lab. I would like to especially thank Edwin, Cameron, Aaron, Ty, Yun, Nick, Yiyang, Rachel, Tamika, and Jonathan for making the lab a more spirited place. This was a much-needed boost during all the long days and late nights.

I would also like to thank my mother and Amubuwa, whose continued encouragement brought me to graduate school and helped me complete the journey. This process would not have been possible without the unwavering support of my amazing wife, Abriti, and for that I will be eternally grateful. Finally, I would like to thank my daughter, Sanya, and son, Randall, for the inspiration they gave me to work hard toward finishing my degree as soon as possible, and for being (mostly) well behaved throughout my writing process.



## TABLE OF CONTENTS

LIST OF TABLES .....	8
LIST OF FIGURES .....	9
LIST OF ABBREVIATIONS .....	13
ABSTRACT.....	15
CHAPTER 1. INTRODUCTION .....	16
1.1 Liquid Chromatography .....	16
1.1.1 Fundamentals of Liquid Chromatography .....	16
1.1.2 The Theoretical Plate as a Model .....	17
1.1.3 Resolution .....	19
1.1.4 Particle Morphology .....	20
1.2 Protein Liquid Chromatography .....	21
1.2.1 Contributions to Peak Broadening from the A-term.....	25
Broadening by the Instrument .....	25
Nonuniform Column Packing .....	26
Effect of Protein Heterogeneity on Measurement of A.....	27
1.2.2 Contribution from the B term: diffusion through porous media.....	28
1.2.3 Contributions to the C term .....	30
Poiseuille Flow Profile .....	31
Intraparticle Diffusion .....	34
1.2.4 Slow Desorption and Reduction of Tailing .....	39
1.3 Hydrophilic Interaction Liquid Chromatography .....	41
1.4 Nano-LC .....	43
1.5 Electrospray Ionization – Mass Spectrometry .....	44
1.6 Research Objectives.....	46
1.7 References.....	46
CHAPTER 2. MECHANISTIC ASPECTS OF HILIC SEPARATION OF GLYCANS AND GLYCOPROTEINS.....	54
2.1 Introduction.....	54
2.2 Experimental .....	55

2.2.1	Chemicals .....	55
2.2.2	Methods .....	55
	Glycan Sample Preparation .....	55
	Chromatographic Methods .....	57
	Molecular Modeling .....	57
2.3	Results and Discussion .....	57
2.4	Conclusion .....	65
2.5	References .....	65
CHAPTER 3. DEVELOPING A NANO-HILIC PLATFORM FOR SEPARATION OF Labeled Glycoproteins with Fluorescence Detection .....		69
3.1	Introduction .....	69
3.2	Experimental .....	70
3.2.1	Materials .....	70
3.2.2	Methods .....	71
	Sample Preparation .....	71
	Particle Preparation .....	72
	Ex-situ Polymer Modification .....	73
	Column Packing .....	75
	In-column Polymer Modification for Stainless-Steel Columns .....	77
	Capillary Column Packing .....	79
	In-capillary Silane Modification .....	80
	In-capillary Polymer Modification .....	82
	Fluorescence Microscopy .....	83
3.3	Results and Discussion .....	84
3.3.1	Bonded Phase Selection .....	84
3.3.2	On-column Focusing for NanoLC-Fluorescence Microscopy .....	85
3.3.3	Nano-HILIC Separation of Labeled Glycoproteins .....	88
3.4	Conclusion .....	93
3.5	References .....	93
CHAPTER 4. NANO-HILIC-MS FOR SEPARATION OF PROTEINS AND GLYCOPROTEINS ON THE SUB-FEMTOMOLE LEVEL .....		96

4.1	Introduction.....	96
4.2	Experimental .....	98
4.2.1	Materials .....	98
4.2.2	Methods .....	98
	Fluorescence Microscopy of Linked Needle Emitter.....	98
	Needle Emitter Preparation & Packing .....	99
	Bonded Phase Synthesis.....	103
	Mass Spectrometer Configuration.....	104
	IdeS Protease Digestion of the NIST mAb Standard .....	104
4.3	Results and Discussion .....	104
4.3.1	Broadening Introduced by Hollow Needle Emitter .....	104
4.3.2	Capillary Column with Integrated Emitter .....	106
4.3.3	nanoHILIC-MS Glycoprotein Separations .....	108
4.3.4	Analyte Identification .....	113
4.4	Conclusion .....	120
4.5	References.....	121
CHAPTER 5. FUTURE DIRECTIONS .....		126
5.1	Superficially Porous Particles .....	126
5.2	Copolymer Bonded Phase.....	129
5.3	Analysis of Therapeutic mAb Samples and Glycoprotein Biomarkers .....	131
5.4	References.....	133
PUBLICATION .....		135

## LIST OF TABLES

Table 1.1 Hypothesized Retention Mechanisms Responsible for HILIC Separations. Courtesy of Buszewski, et. al <sup>75</sup> .....	42
Table 2.1. Values for $m$ , the slope in Equation 2.3, for the RNase B glycovariants and free glycans .....	64
Table 2.2. Values for $k_0$ , the intercept in Equation 2.3, for the RNase B glycovariants and free glycans .....	64
Table 3.1. Slope data for the linear-fit trendlines illustrated in Figure 3.12.....	85
Table 4.1. Glycovariants identified in the NIST mAb standard with retention time corresponding to chromatogram in Figure 4.17. Expected mass calculated based upon observed $m/z$ for main (G0F) glycoform. Structure and percent composition based upon results from a NIST interlaboratory investigation <sup>34</sup> . .....	117

## LIST OF FIGURES

Figure 1.1. An illustration of the terms presented in the van Deemter equation .....	19
Figure 1.2 TEM micrographs of fully porous (left), non-porous (center), and superficially porous (right) silica particles, obtained using instrumentation in the Life Science Microscopy Facility at Purdue University .....	20
Figure 1.3. Log-linear plot of retention factor vs. volume fraction strong solvent, adapted from Snyder, et. al. <sup>25</sup> Copyright 1983, American Chemical Society. ....	22
Figure 1.4. A comparison of van Deemter plots for protein (top) and small-molecule (bottom) analytes separated using columns packed with porous (○) and non-porous (●) particles. Adapted with permission from DeStefano, et. al. <sup>29</sup> Copyright 2014, Elsevier. ....	24
Figure 1.5. Images of non-porous silica particles packed into capillaries. Figure A adapted with permission from Patel, et. al. <sup>33</sup> . Copyright 2004, American Chemical Society. Figure B adapted with permission from Wei, et. al. <sup>34</sup> . Copyright 2012, American Chemical Society. Figure C adapted with permission from Rogers, et. al. <sup>35</sup> . Copyright 2013, American Chemical Society. ....	27
Figure 1.6. Diagram illustrating the appearance of peak broadening caused by synthetic overlapping Gaussians (left, center) and the effect this has on the resulting van Deemter plot (right) .....	28
Figure 1.7. Data for capillary porosity ( $\epsilon$ ), the ratio of diffusion within the packed capillary vs. an open tubular capillary ( $D/D_0$ ), and the ratio for ionic current within the packed capillary vs. an open tubular capillary ( $i/i_0$ ). Adapted with permission from Rogers, et. al. <sup>40</sup> Copyright 2013, American Chemical Society. ....	30
Figure 1.8. Comparison of capillary (left) and traditional UHPLC (right) columns for separation of an IgG4-type monoclonal antibody and its aggregates. Adapted with permission from Rogers, et. al. <sup>43</sup> Copyright 2013, American Chemical Society. ....	32
Figure 1.9. Illustration of the structure of a 2 $\mu$ m fused-core particle. Adapted with permission from DeStefano, et. al. <sup>29</sup> Copyright 2014, Elsevier. ....	37
Figure 1.10. van Deemter plots for columns containing fused core (★) and fully porous (∇) particles. Adapted with permission from DeStefano, et. al. <sup>29</sup> Copyright 2014, Elsevier. ....	38
Figure 1.11. Comparison of the separation of mAb disulfide isoforms using columns containing particles of varying pore-size. From bottom to top: 1000 Å, 400 Å, and 300 Å. Adapted with permission from Wei, et. al. <sup>54</sup> Copyright 2017, Elsevier. ....	39
Figure 1.12. An illustration of the electrospray process used in analyte ionization for detection with a mass spectrometer. ....	45
Figure 2.1. Chromatograms for the gradient elution of free glycans (left) and intact glycoproteins (right). ....	58

Figure 2.2. van Deemter plots for isocratic separations of the free Man5 glycan and the intact RNase B (+Man5) glycoprotein using detection at $\lambda = 254$ nm and 280 nm, respectively. The shaded area indicates the typical working range, at 100 – 200 $\mu$ L/min.....	59
Figure 2.3. Deconvoluted mass spectrum for the purified RNase B (+Man5) glycoprotein .....	60
Figure 2.4. Chromatograms for a separation of the purified RNase B (+Man5) glycoprotein using UV absorbance (black) and mass spectrometry-based (red) detection methods .....	61
Figure 2.5. Log-log plots of retention factor as a function of mole fraction H <sub>2</sub> O for the free glycans of RNase B (left) and the intact glycovariants (right).....	62
Figure 3.1. Workflow for Labeling Protein with Small-molecule Fluorophore .....	72
Figure 3.2. AGET-ATRP Reaction Scheme .....	73
Figure 3.3. TEM Micrograph of particles before and after adding a polymer brush layer using surface-initiated polymerization .....	75
Figure 3.4. Stainless-steel Column Packing Setup .....	76
Figure 3.5. CAD drawing of custom-made column packing union.....	77
Figure 3.6. TEM image of particles with a PAAm brush layer from an in-column polymerization reaction (after depacking) .....	78
Figure 3.7. Photograph of capillary column packing hardware.....	80
Figure 3.8. Diagram of humidification chamber used for particle surface conditioning prior to in-capillary silane modification.....	81
Figure 3.9. Diagram of in-capillary silane reaction .....	82
Figure 3.10. Diagram of apparatus used for in-capillary polymer modification .....	83
Figure 3.11. Diagram of instrumentation used in fluorescence microscopy-based analyses .....	84
Figure 3.12. Snyder Plots for separation of RNase B glycoforms using a commercial amide column (left) compared with lab-made PHMAAm (center), and PAAm (right) columns. All are plotted over the same range to facilitate comparison.....	85
Figure 3.13. Image of the head of a packed capillary column with a segment of hollow capillary upstream, captured using an optical microscope at 11x. ....	86
Figure 3.14. False-color fluorescence images of labeled protein analytes under stacking conditions (top) and 10 minutes into the gradient elution (bottom). ....	87
Figure 3.15. False-color fluorescence image demonstrating the narrower zone width resulting from improved sample diluent composition .....	88
Figure 3.16. Structure of Alexa Fluor 488 fluorescent dye <sup>15</sup> .....	89
Figure 3.17. UV-visible chromatograms from a single analysis of an RNase B sample, post-labeling, with detection at different wavelengths. Labeled and unlabeled proteins absorb at 280 nm (red), but only the labeled proteins absorb at 495 nm (black) .....	89

Figure 3.18. UV chromatograms illustrate the difference in complexity between labeled RNase B modified using the standard protocol (red) and under-labeling conditions (black).....	90
Figure 3.19. Comparison of different gradient slopes for separation of labeled RNase B using a 3 cm PAAm-modified capillary— $\Delta B = 15\%$ over 30 minutes (left) and over 20 minutes (right) .	91
Figure 3.20. Comparison of different gradient start points for separation of labeled RNase B using a 3 cm PAAm-modified capillary, starting at 75%B (left) vs. 77%B (right) .....	91
Figure 3.21. Chromatograms obtained at different positions along the same capillary column ..	92
Figure 3.22. False-color fluorescence images of the chromatographic zone from RNase B (+Man5) at different positions along the same capillary column (top to bottom: 1 cm, 2 cm, 3 cm.) The minor peak on the right is believed to be the same glycoprotein with an additional label .....	92
Figure 4.1. Diagram of setup used in imaging the tip of a hollow needle emitter, post-capillary	99
Figure 4.2. Photograph of capillary column (left) linked to a hollow needle emitter (right) using a PTFE sleeve .....	99
Figure 4.3. Diagram of the equipment used in surface humidification for the gas-phase silylation of needle emitter tips.....	100
Figure 4.4. Schematic of the apparatus utilized in packing needle emitters.....	102
Figure 4.5. An image of a fritted needle emitter, containing a 1 mm segment of PHMAAm-coated superficially porous particles. Captured using an optical microscope at 11x zoom.....	103
Figure 4.6. Chromatograms from separation of A488-labeled RNase B at the end of a capillary column before (left) and after (right) travelling through a linked needle emitter. Gradient elution was utilized, with 75-60% ACN + 0.1% FA, 0.025% TFA over 30 minutes.....	105
Figure 4.7. A magnified view of the first peak for each of the two chromatograms presented in Figure 4.6 .....	106
Figure 4.8. Commercial needle emitter packed without sonication.....	107
Figure 4.9. Unmodified commercial needle emitter, with the tip fractured during sonication...	107
Figure 4.10. Silanized needle emitter with a 1 mm frit composed of PHMAAm-coated SPP, and a packed bed of PAAm-coated nonporous particles. The visible gap is a result of constriction of the packed bed upon drying, resolved by rehydration of the packed bed or avoiding dehydration altogether. The tip is intact.....	108
Figure 4.11. Base peak chromatogram for nanoHILIC-MS separation of intact, unlabeled RNase A and RNase B glycoforms using a lab-made capillary column. A gradient of 75-65% ACN + 0.1% FA, 0.025% TFA is run over 30 minutes.....	109
Figure 4.12. Models of an intact IgG1 glycoprotein based on X-ray crystallography data <sup>39</sup> , generated with a “head on” perspective (top) and rotated 90° about the y-axis (bottom) .....	111
Figure 4.13. Model of the G1F glycan-bearing Fc fragment from an IdeS digestion of the NIST mAb <sup>38</sup> , based on X-ray crystallography data. Scale is 2x that of Figure 4.12.....	112

Figure 4.14. A comparison of base peak chromatograms for the NIST mAb Fc fragment, obtained using the nanoHILIC-MS platform (left) and using a commercial HILIC UHPLC column (right) .....	113
Figure 4.15. Mass spectra obtained over the entire 30-minute gradient for the NIST mAb (top) vs that obtained when limiting the time window to that of the peak for the G1F glycoform (bottom) .....	114
Figure 4.16. Deconvoluted mass spectrum for the G1F peak, generated using MagTran software to process the raw mass spectrum from Figure 4.15.....	114
Figure 4.17. Chromatogram from nanoHILIC-MS separation of the <i>IdeS</i> -digested NIST mAb standard. Mass-confirmed glycoform identities are presented in Table 4.1. A gradient of 78-63% ACN + 0.1% FA, 0.025% TFA was run over 30 minutes. ....	116
Figure 4.18. Extracted ion chromatogram for the Man5 glycoform (red) present the NIST mAb standard set against the base-peak chromatogram (black) from the same analysis .....	120
Figure 5.1. Chromatograms from separation of RNase B using columns with varying particle morphology—non-porous (left), superficially-porous (right), and fully-porous (right) with varying analyte mass—0.3 $\mu$ g (bottom), 1 $\mu$ g (middle), and 2 $\mu$ g (top).....	127
Figure 5.2. SEM micrograph of a superficially-porous particle before polymer modification ..	128
Figure 5.3. SEM micrograph of a superficially-porous particle after coating with a PHMAAm brush layer.....	129
Figure 5.4. Snyder Plots for RNase B glycoforms separated using PHMAAm (left) and PAAm (right) bonded phases .....	130
Figure 5.5. Diagram of a random copolymer comprised of AAm and HMAAm monomers.....	131
Figure 5.6. nanoHILIC-MS base peak chromatogram for separation of AFP glycovariants, using a gradient of 75% - 60% ACN (+0.1% FA, 0.025% TFA) over 30 minutes.....	132
Figure 5.7. nanoHILIC-MS base peak chromatogram for separation of PSA glycovariants, using a gradient of 75% - 60% ACN (+0.1% FA, 0.025% TFA) over 30 minutes.....	133



## LIST OF ABBREVIATIONS

A488	Alexa Fluor 488
AAm	Acrylamide
AFP	Alpha-fetoprotein
AGET	Activators Generated by Electron Transfer
ATRP	Atom Transfer Radical Polymerization
DoL	Degree of Labeling
DTT	Dithiothreitol
EIC	Extracted-ion Chromatogram
ESI	Electrospray Ionization
FA	Formic Acid
DMSO	Dimethylsulfoxide
EtOH	Ethanol
GlcNAc	N-Acetylglucosamine
FA	Formic Acid
Fab	Antigen-binding fragment
Fc	Fragment crystallizable region
FM	Fluorescence microscopy
FWHM	Full-width at half-maximum peak height
HILIC	Hydrophilic interaction liquid chromatography
HMAAm	Hydroxymethacrylamide
HPLC	High-performance liquid chromatography
IPA	Isopropanol
IdeS	Immunoglobulin-degrading enzyme from <i>Streptococcus pyogenes</i>
IgG	Immunoglobulin G
LC	Liquid chromatography
Man	Mannose
mAb	Monoclonal antibody
mBC	(chloromethyl)phenylethyl-dimethylchlorosilane
mC1	Trimethylchlorosilane

Me <sub>6</sub> TREN	Tris 2-(dimethylamino) ethyl amine
MS	Mass Spectrometry
NIST	National Institute of Standards and Technology
NPLC	Normal-phase liquid chromatography
PAAm	Polyacrylamide
PHMAAm	Polyhydroxymethacrylamide
PNGase	Peptide-N-Glycosidase
PTM	Post-translational modification
PSA	Prostate-specific antigen
RPLC	Reversed-phase liquid chromatography
SEM	Scanning electron microscope
SPE	Solid-phase extraction
SPP	Superficially-porous particles
tBC	(p-chloromethyl)phenyltrichlorosilane
tC1	Methyltrichlorosilane
TEM	Transmission electron microscope
TFA	Trifluoroacetic acid
UPLC	Ultra-performance liquid chromatography
UHPLC	Ultrahigh-performance liquid chromatography

## **ABSTRACT**

A nanoHILIC-MS platform was developed to provide a means for top-down and middle-up analysis of glycoproteins. A mechanistic approach was taken in evaluating characteristics of the stationary phase of the chromatography column. Results from this evaluation informed the selection of a polyacrylamide brush layer-based bonded phase, which was applied to nonporous silica nanoparticles. Fluorescence microscopy was used for direct analysis of labeled proteins during nanoHILIC separations, with the platform subsequently adapted for mass spectrometry-based detection of intact and semi-intact glycoproteins. It was found that the standard technique of linking a hollow needle emitter to the capillary chromatography column for mass spectrometry-based detection yielded an unacceptable level of band broadening, necessitating the development of a column with an integrated needle emitter. The resulting nanoHILIC-MS method yielded peak widths as sharp as 3.5 seconds, enabling ultra-sensitive detection and identification of 28 glycoforms of an IgG1 $\kappa$  monoclonal antibody standard.

## CHAPTER 1. INTRODUCTION

Part of this chapter is adapted from  
C. Bupp, M. Wirth, Annual Review of Analytical Chemistry, 2020, 13:13.1-13.18

### 1.1 Liquid Chromatography

#### 1.1.1 Fundamentals of Liquid Chromatography

Liquid Chromatography (LC) is an analytical technique that is regularly used to separate analytes based on their fundamental molecular properties. Although it is a well-established field, dating back more than a century,<sup>1</sup> it is one that has seen constant advances that make it more essential every year.

At the heart of a modern LC apparatus is the chromatography column, which contains the medium, or “stationary phase”, used to physically separate analytes in bands as they travel along the column. This separation occurs based on interactions between the analyte and the stationary phase, with more strongly-interacting analytes being retained on the column longer.

The scale of these chromatography columns spans many orders of magnitude. Industrial-scale applications can demand columns several meters in diameter, with flowrates often exceeding a liter per minute.<sup>2</sup> On the opposite end of the spectrum lie nano-scale columns, which have internal diameters on the order of tens of micrometers and are used with flowrates on the nanoliter per minute scale.<sup>3</sup>

The liquid passing through these columns is generally referred to as the “mobile phase” and typically relies on a pressure-driven flow.<sup>4</sup> Traditional liquid chromatography instruments utilized pumps capable of delivering flow with pressures up to approximately 50 bar.<sup>5</sup> The advent of High Performance Liquid Chromatography (HPLC) in the late 1960s introduced particles on the scale of several microns, requiring pumps capable of delivering flow up in upwards of several hundred bar.<sup>6</sup> Further improvements can be realized with ever-smaller particles, which will be discussed in more detail later in this chapter. Modern “Ultra-high Performance Liquid Chromatography” (UHPLC) systems utilizing columns with sub-2 $\mu\text{m}$  particle sizes require pumps which can deliver upwards of 1,000 bar in order to overcome the extraordinary backpressure these columns introduce<sup>7</sup>.

### 1.1.2 The Theoretical Plate as a Model

A common way to discuss the fundamental performance of a chromatography column is in the context of a “theoretical plate”, or simply “plate.” The plate can be imagined as a stage, where the analyte interacts with the surface of the stationary phase to reach a quasi-equilibrium condition. In this condition, a fraction of the analyte molecules adsorb to the stationary phase corresponding to the strength of the interaction. This fractional distribution is referred to as  $K$ , termed the equilibrium constant or partition coefficient.<sup>8</sup> Equation 1.1 describes  $K$  in terms of  $C_S$  and  $C_M$ , the concentration of analyte in the stationary and mobile phases, respectively.

$$K = \frac{C_S}{C_M}$$

Equation 1.1

The chromatographic band, or “zone” can be imagined as traveling along the column in a series of steps, where each plate represents a point where an absorbed analyte can be retained until it is transferred along to the next plate. This hypothetical process is illustrated in Figure 1.1. The retention of the zone along the way is quantitatively described as a “retention factor”,  $k$ , defined in terms of  $t_r$  and  $t_m$  (aka  $t_0$ ) which represent the time spent adsorbed to the stationary phase vs. the time in the mobile phase, respectively (Equation 1.2). Historically,  $k$  has also been written as  $k'$ , but this term has fallen out of use in recent years.<sup>9</sup>

$$k = \frac{t_r}{t_m}$$

Equation 1.2.

The retention factor can also be rewritten in terms of the equilibrium constant and the ratio of the physical volumes of stationary and mobile phases,  $V_s$  and  $V_M$  respectively (Equation 1.3). This ratio is also referred to as the “phase ratio”, or  $\Phi$ .<sup>10</sup>

$$k = K \left( \frac{V_S}{V_M} \right) = K\Phi$$

Equation 1.3.

The efficiency of a column is often described in terms of these theoretical plates, where the number of plates for a particular column is directly proportional to its efficiency. This nomenclature harkens back to countercurrent chromatography and fractional distillation, as the plate refers to a discrete zone within a distillation column where separation occurs.<sup>11</sup> The dimensionless number of theoretical plates can be calculated based upon Equation 1.4 where  $L$  is the length of the chromatographic column and  $H$  (also referred to as the “Height Equivalent of a Theoretical Plate”) is a term utilized in the van Deemter model<sup>12</sup> and defined in Equation 1.5.

$$N = \frac{L}{H}$$

Equation 1.4.

$$H = A + \frac{B}{v} + C \cdot v = A + \frac{2\gamma D}{v} + \omega_m \frac{d_p^2}{D} v + \omega_p \frac{d_p^2}{D} v + \frac{2k}{(1+k)} \tau_{des} v$$

Equation 1.5.

This fundamental equation, commonly known as the van Deemter Equation,<sup>12</sup> is a cornerstone in the mathematical description of chromatographic performance<sup>7</sup> and will be referenced multiple times in the remainder of this dissertation.

The first term in the van Deemter Equation,  $A$ , lumps together all contributions to broadening that are approximately independent of flow rate.<sup>13</sup> The  $B$  term is from diffusion along the separation axis.<sup>14</sup> Multiple phenomena contribute to  $C$ : (a) the distribution of velocities owing to the parabolic Poiseuille flow profile between particles, dictated by  $\omega_m$ ; (b) the delay in transport owing to the need for diffusion in and out of porous particles, dictated by  $\omega_{ip}$ ; and (c) slow

desorption of the analyte from the bonded phase back into the mobile phase, dictated by  $\tau_{\text{des}}$ . Figure 1.1 illustrates the sources of the terms above. A plot of plate height versus velocity,  $v$ , reveals the values of  $A$ ,  $B$ , and  $C$  if the velocity range is sufficient.

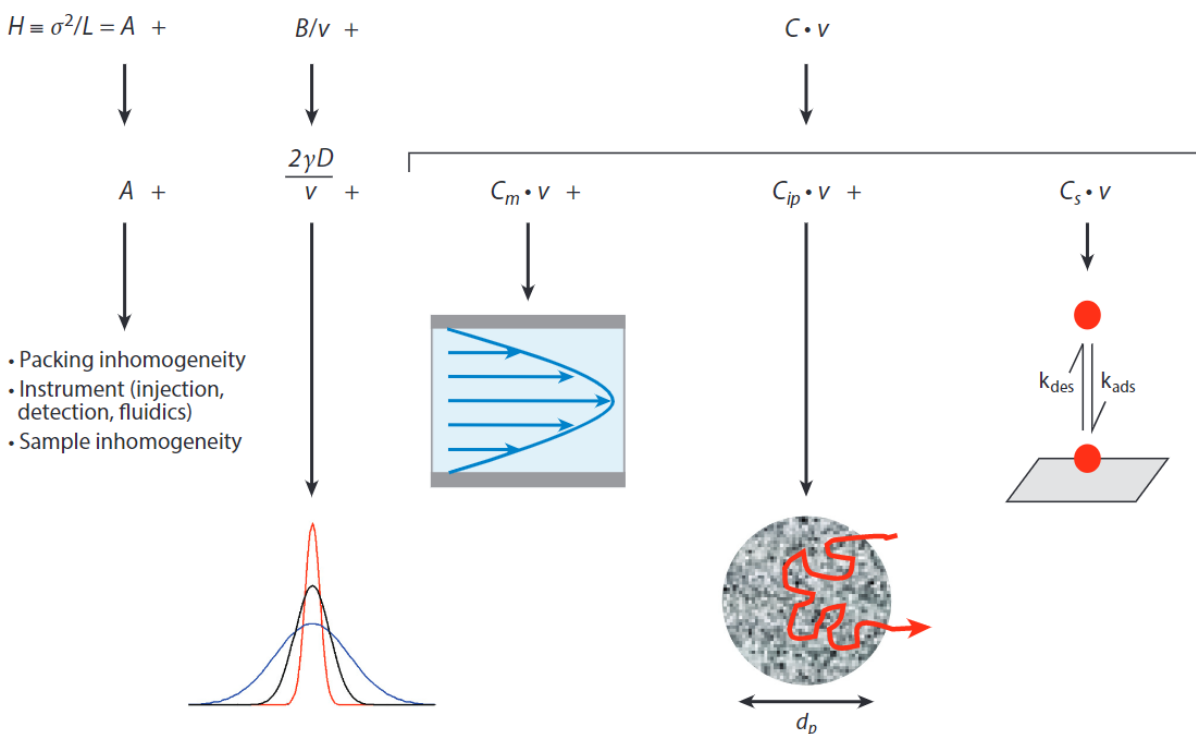


Figure 1.1. An illustration of the terms presented in the van Deemter equation

### 1.1.3 Resolution

The ultimate goal in any chromatographic separation is to achieve the optimum resolution in a given period of time. Resolution,  $R_s$ , in chromatography is defined by the ratio of peak separation,  $\Delta X$ , and the peak width at the base,  $4\sigma$ , where  $\sigma$  is the standard deviation:

$$R_s = \frac{\Delta X}{4\sigma}$$

Equation 1.6.

There are countless parameters in a chromatographic separation that can be adjusted in working to optimize resolution for a specific analyte or analytes. Method development is a

(typically-iterative) process that involves adjusting multiple parameters in order to maximize resolution for an analyte (or analytes) of interest.<sup>15</sup> The parameters are wide-ranging, including the composition of the mobile phase, the temperature at which the separation is performed, the mobile phase flowrate, the composition of the sample solution, and what is arguably the most important consideration: the design and selection of the chromatographic column itself.

#### 1.1.4 Particle Morphology

The stationary phase of a chromatography column is typically composed of many individual particles packed into the column via gravity or with the assistance of a high-pressure pump.<sup>16</sup> These particles are normally silica-based, with the surface of the particle functionalized with molecules that will selectively interact with the analytes-of-interest. This functional group is also referred to as the “bonded phase”.<sup>17</sup>

These silica particles are typically porous in nature, with the pores acting to increase the effective surface area of the particle.<sup>18</sup> This, in-turn, provides more sites where analytes can interact with the bonded phase. There are three basic classes of silica particle: fully-porous, non-porous, and superficially-porous (also known as “fused-core”, or “core-shell”) particles.<sup>19</sup> The latter consists of a non-porous “core” surrounded by multiple layers of smaller particles that give it a porous outer structure. TEM images of the three particle types can be seen in Figure 1.2.

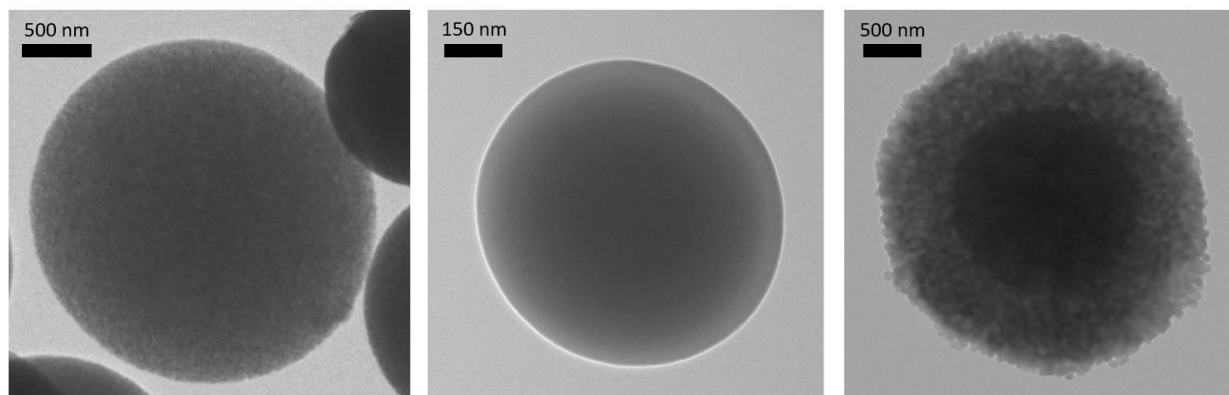


Figure 1.2 TEM micrographs of fully porous (left), non-porous (center), and superficially porous (right) silica particles, obtained using instrumentation in the Life Science Microscopy Facility at Purdue University



The C-term in the van Deemter Equation discussed in Section 1.1.2 illustrates the drawback of a porous particle; the slow diffusion into and out of the porous internal structure will cause band broadening. This process does not occur with non-porous silica, eliminating the  $\omega_{ip}$  term in the van Deemter equation for this type of particle. The core-shell particle provides a middle ground, as the maximum path-length a molecule can travel inside a porous shell is shorter than that for a fully-porous particle.<sup>19</sup>

## 1.2 Protein Liquid Chromatography

The analysis of protein mixtures has emerged as an area of intense research and invention due to two main drivers. First, the advent of genetic engineering gave rise to a new class of pharmaceuticals, termed biologics, which are made of proteins. Most notable are the therapeutic monoclonal antibodies (mAbs), which target diseases with high specificity.<sup>20, 21</sup> Five mAbs are now among the top 15 drugs in terms of sales.<sup>22</sup> Second, completion of the Human Genome Project spawned the field of proteomics, which entails the study of changes in gene expression due to metabolism, disease, therapeutics, or environment.<sup>23, 24</sup> The analysis of proteins for both pharmaceuticals and proteomics relies on a chemical separation combined with mass spectrometry. There has been much research activity and advancement in the technology for both separations and mass spectrometry of proteins to address the many challenges in protein analysis.

As described in Section 1.1.2, the van Deemter model is a standard tool for assessing the efficiency of a chromatography column. Although the literature is rife with van Deemter plots for small molecules, these are scarce for proteins. The reason is that the van Deemter equation applies to isocratic separations, i.e., separations where the mobile phase has a constant composition, whereas protein HPLC is invariably performed with gradient elution. Figure 1.3, which depicts plots of  $\log k$  versus fraction of organic phase,  $\phi$ , in the case of RPLC, helps to explain why gradient elution is needed. For small molecules, the slope is low, so one mobile phase composition will elute a wide range of compounds. For proteins, the slope is high and the intercepts differ, so a range of compositions is usually needed for elution on a reasonable timescale. The van Deemter equation does not apply to gradient elution because the velocity of the protein changes as it travels through the column,<sup>25</sup> whereas the van Deemter model requires a constant velocity of the analyte. Gradient elution also gives compression in the width of the peak because the leading side travels more slowly than the trailing side of the peak, where the solvent is stronger.<sup>26</sup> As a result of both

of these factors, peak widths for gradient elution generally remain constant even for long elution times, in contrast to peaks for isocratic elution, which broaden with elution time. Consequently, one cannot directly obtain efficiency data from most of the data in the literature for protein separations.

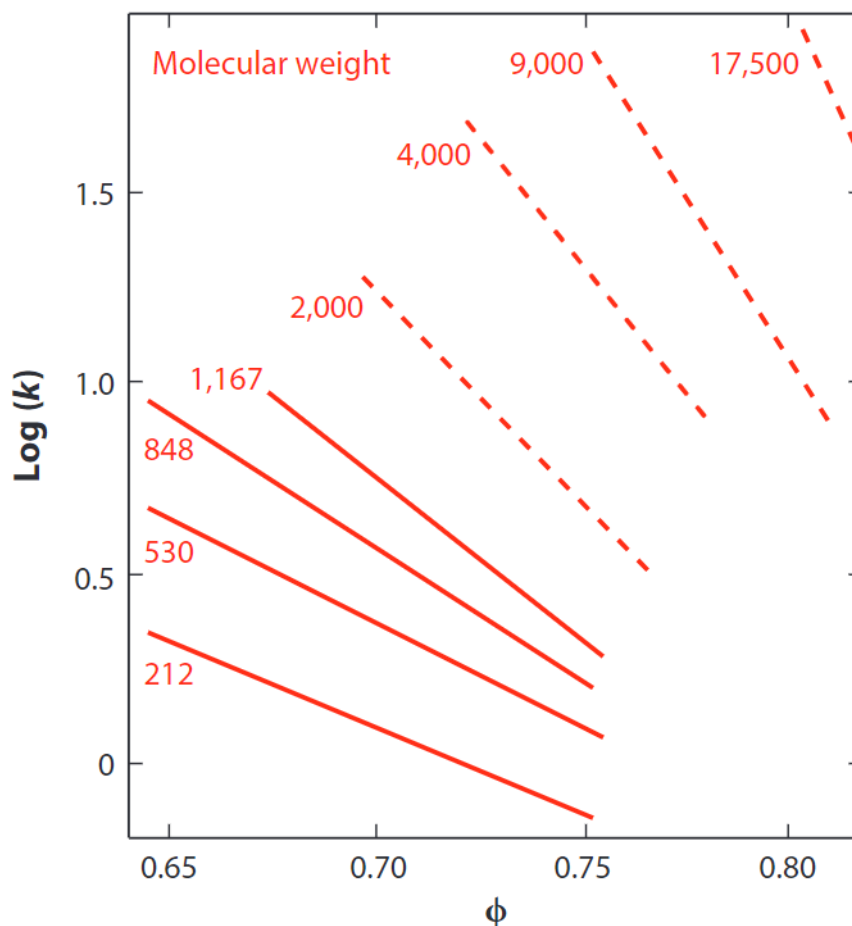


Figure 1.3. Log-linear plot of retention factor vs. volume fraction strong solvent, adapted from Snyder, et. al.<sup>25</sup> Copyright 1983, American Chemical Society.

Figure 1.4a shows an informative van Deemter plot for a protein, published by Wu et al.<sup>27</sup> The figure compares van Deemter plots for two columns using particles of the same 1.5- $\mu\text{m}$  diameter, one porous and the other nonporous, to assess the contribution from intraparticle diffusion. There is no rise in  $H$  at low velocity, indicating that the value of  $B/v$  is much smaller than  $A$  and  $C \cdot v$  over the velocity range. For the velocities typically used in protein separations, from 0.1 to 0.3 cm/s, the main contribution to the plate height is  $C$ . The plot illustrates that using nonporous

particles significantly lowers the value of  $C$ , with  $C \sim 34$  ms and  $\sim 20$  ms for the porous versus nonporous particles, respectively. For small molecules, Figure 1.4b shows  $C$  as more than an order of magnitude smaller, owing mainly to the diffusion coefficients of small molecules being much larger. The data, while noisy, report  $A \sim 7$   $\mu\text{m}$  for the proteins. For the small molecule,  $A$  must be smaller because the minimum  $H$  is typically on the order of 10  $\mu\text{m}$ .<sup>28</sup> A discussion of the  $A$  term shows that it has no dependence on molecular size or diffusion coefficient, and it is for a different reason that the  $A$  term is high for proteins in this case.

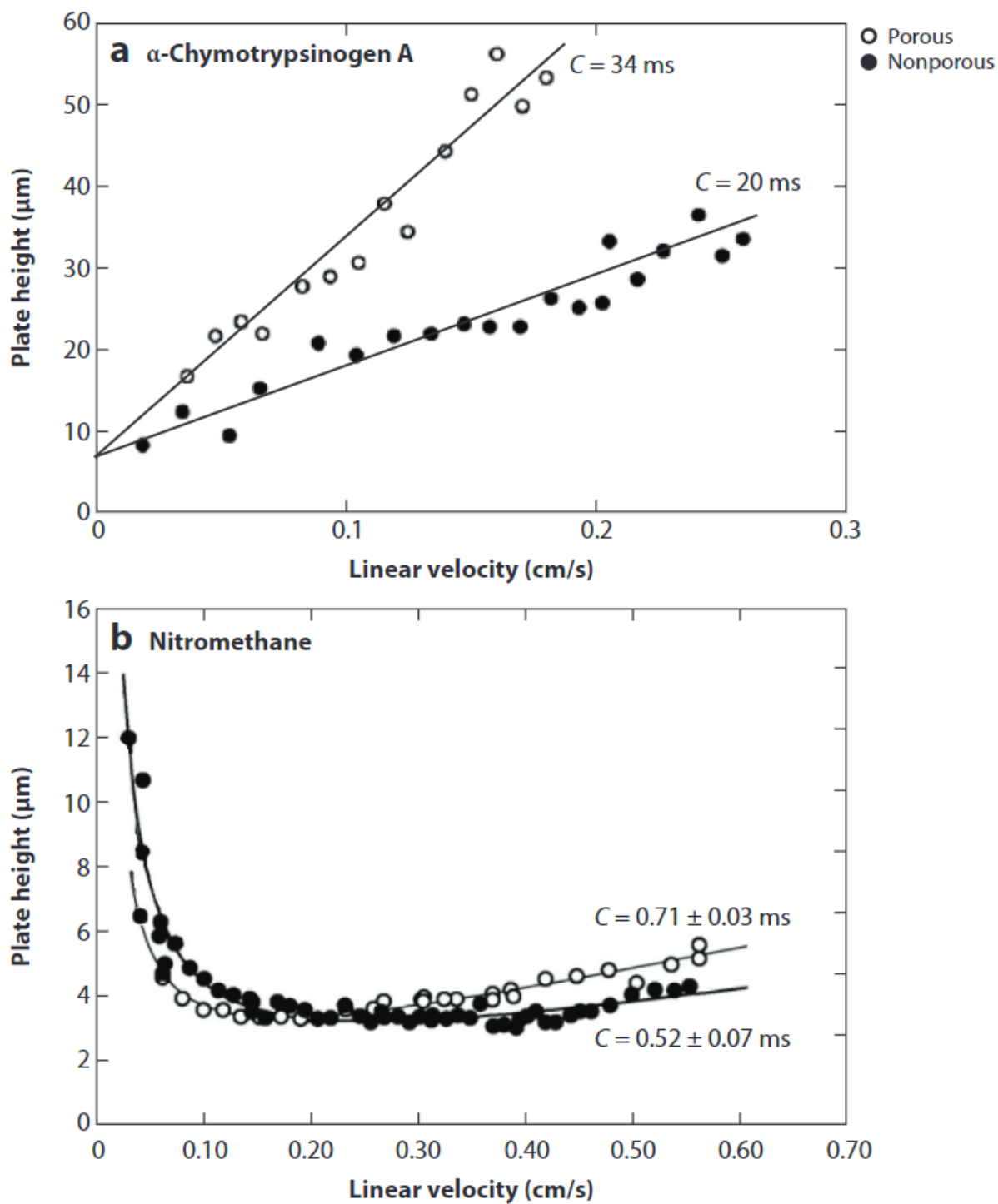


Figure 1.4. A comparison of van Deemter plots for protein (top) and small-molecule (bottom) analytes separated using columns packed with porous ( $\circ$ ) and non-porous ( $\bullet$ ) particles. Adapted with permission from DeStefano, et. al.<sup>29</sup> Copyright 2014, Elsevier.

### 1.2.1 Contributions to Peak Broadening from the A-term

The lower limit for plate height in protein RPLC is dictated by the A term in the van Deemter equation. While decreasing the flowrate can progressively lower the plate height by lessening the impact of the C term, the contributions from extra-column effects and eddy diffusion establish an absolute minimum value for H.

#### *Broadening by the Instrument*

In Figure 1.4, the largest contribution to A is the peak dispersion from the instrument itself. Its contribution is magnified for proteins compared to small molecules because protein separations are done using narrower column i.d. to allow for analysis of smaller amounts of valuable sample. The instrument used in the work of Wu et al.<sup>27</sup> has the current industry standard for low dispersion,  $\sigma_v \sim 2 \mu\text{L}$ . The column is also typical for proteins, with a short length of 50 mm and a narrow i.d. of 2.1 mm, making the column volume low. The porosity,  $\varepsilon$ , of the column is the ratio of the liquid volume to the geometric volume of the column, and this is typically 0.4. The limit has been shown by Schure et al. to be 0.36 for randomly packed particles.<sup>30</sup> If the column contributed nothing to broadening, then a peak broadened to 2  $\mu\text{L}$  by the instrument would give a plate height of 5.4  $\mu\text{m}$  if the column has a 2.1 mm i.d. and length of 50 mm, with  $\varepsilon = 0.4$  and  $k=2$ . The calculation is shown in Equation 1.7 for clarity:

$$A_{instr} = \frac{\left(0.002 \text{ cm}^3 / \pi \cdot (i.d./2)^2 \text{ cm}^2 \cdot \varepsilon\right)^2}{L \cdot (1+k)^2} = 5.4 \times 10^{-4} \text{ cm}$$

Equation 1.7

The calculation illustrates that under the best circumstance of only 2  $\mu\text{L}$  of dispersion from the instrument, it can contribute significantly to the overall A term at low velocity. Considering that the typical linear velocity is on the order of 0.25 cm/s (at 0.2 mL/min), k is usually larger than 2, and the plate height in Figure 1.4 is 35  $\mu\text{m}$  for the nonporous particles, it is clear that the A term from the instrument itself contributes little to peak broadening in a typical separation with a high performance instrument. Longer columns, in turn, would make the contribution even less significant.

While we conclude that the  $A$  term has only a small contribution to peak broadening for this low-dispersion instrument, the  $A$  term will become more important as the  $C$  term is decreased through advances in column materials. Further, one has a choice in configuring the instrument, which can easily increase its dispersion to become significant. There are three main contributions of the instrument to broadening, as detailed by de Vos et al.: (a) the injected volume, (b) the tubing inner diameter, and (c) the detection volume.<sup>31</sup> These factors need to be considered when broadening from the instrument is a limitation to efficiency.

### ***Nonuniform Column Packing***

The textbook description of the  $A$  term is the heterogeneity of the packed bed. Advances in the engineering of column packing have made it typically less significant than the instrument contribution, but future advances could make heterogeneity of the packed bed a significant factor again. Guiochon and coworkers<sup>32</sup> showed that packed beds are radially heterogeneous in packing density, giving slower flow near the walls. Radial heterogeneity of packing is visually depicted for a capillary in Figure 1.5a for 1- $\mu\text{m}$  silica particles.<sup>33</sup> The image from scanning electron microscopy (SEM) shows that the packing density is highest near the wall, giving more resistance to flow near the wall and, hence, a higher mobile phase velocity away from the walls. Our group showed that packing under sonication reduces the  $A$  term to the nanometer scale for capillaries,<sup>34</sup> and this is illustrated by the SEM image in Figure 1.5b for the case of 0.5- $\mu\text{m}$  nonporous silica particles. Figure 1.5c is a photograph of a capillary packed with mild sonication to maximize domain size, showing strong opalescence associated with crystalline packing. In summary, the 2.1-mm i.d. columns typically used for analytical protein separations currently give a relatively small  $A$  term, as evidenced by the van Deemter plot of Figure 1.4.

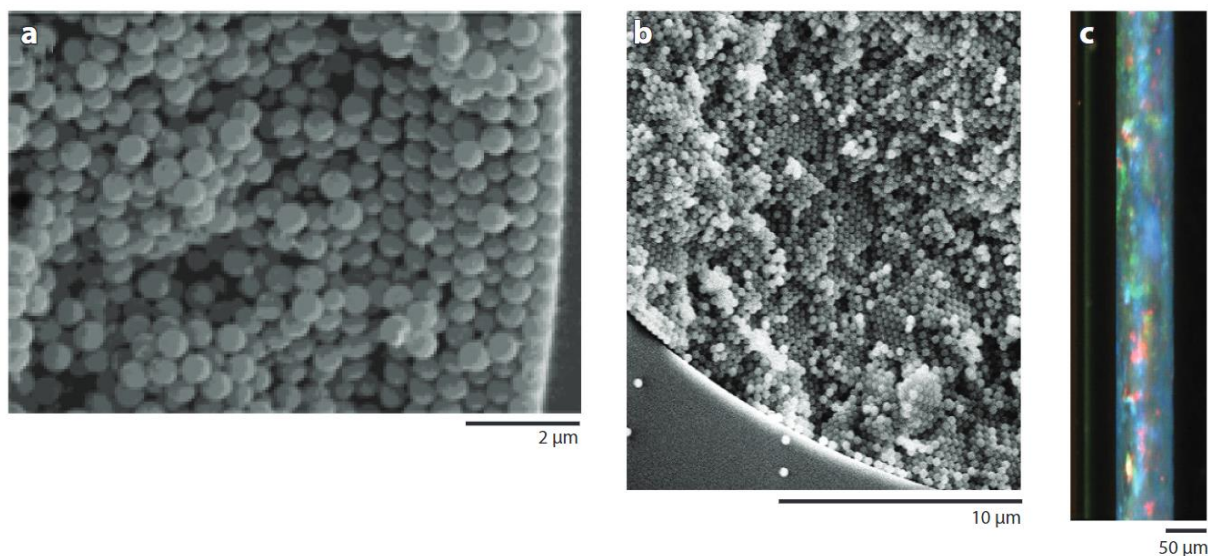


Figure 1.5. Images of non-porous silica particles packed into capillaries. Figure A adapted with permission from Patel, et. al.<sup>33</sup>. Copyright 2004, American Chemical Society. Figure B adapted with permission from Wei, et. al.<sup>34</sup>. Copyright 2012, American Chemical Society. Figure C adapted with permission from Rogers, et. al.<sup>35</sup>. Copyright 2013, American Chemical Society.

### *Effect of Protein Heterogeneity on Measurement of A*

The inevitable existence of proteoforms in the sample can make the column efficiency appear worse than it is. This is illustrated mathematically in Figure 1.6 by using synthetic Gaussians. If the proteoforms have slightly different retention factors, but not different enough to elute beyond the standard deviation of other proteoforms, the collection of peaks gives one broad peak that is wider than what the true column efficiency would give. A van Deemter plot in Figure 1.6 using the synthetic Gaussians illustrates that such a heterogeneous sample would report the correct value of  $C$ , but an erroneously high value of  $A$  by increasing the intercept. This is a possible way of assessing heterogeneity of a peak. Our group previously reported an unexpectedly high  $A$  term of 21  $\mu\text{m}$  for a hydrophilic interaction liquid chromatography (HILIC) separation of protein glycoforms.<sup>36</sup> It perplexed us at the time, but this simulation gives a likely explanation for the high  $A$  term.

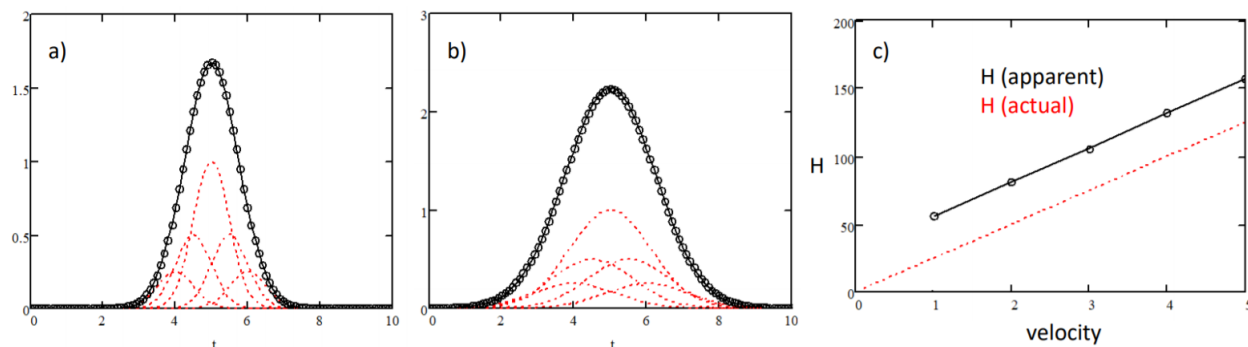


Figure 1.6. Diagram illustrating the appearance of peak broadening caused by synthetic overlapping Gaussians (left, center) and the effect this has on the resulting van Deemter plot (right)

### 1.2.2 Contribution from the B term: diffusion through porous media

Figure 1.1 had illustrated that the  $B$  term in the van Deemter equation is caused by molecular diffusion along the separation axis. Using the Stokes equation,  $\sigma^2 = 2Dt$ , and the mobile phase velocity,  $v = L/t_m$ , one arrives at  $\sigma^2 = 2D/v$  if diffusion only occurs in the mobile phase, i.e., during the time,  $t_m$ , it takes for the mobile phase to travel the length of the column. One adjustment needs to be made: the diffusion is obstructed because the volume of the mobile phase is not fully accessible to the analyte.

The obstruction factor is typically written as  $\gamma$ , which is a fraction between 0 and unity. Knox used GC measurements to show that  $\gamma = 0.6$  for nonporous glass beads, with variations in the next significant figure. Equation 1.8 neglects diffusion of adsorbed analytes, which can be a large factor for small molecules.<sup>37</sup> Proteins do not diffuse detectably when adsorbed, presumably due to the multiplicity of interactions with the bonded phase, therefore, Equation 1.8 only includes  $D$  for proteins in the mobile phase. For  $\gamma = 0.6$  and for a protein having  $D = 10^{-6} \text{ cm}^2/\text{s}$ ,  $H_B = 0.1 \text{ } \mu\text{m}$  at the relatively low linear velocity of  $0.1 \text{ cm/s}$ . This is below the noise on a van Deemter plot, explaining why there is no visible contribution of the  $B$  term for the protein in the van Deemter plot of Figure 1.4a. This section could be ended here, but diffusion is the molecular property that controls much of the  $C$  term, so it is important to understand how diffusion is obstructed in porous media. Most pertinent to the discussion is that diffusion into and out of porous particles, which is soon shown to contribute significantly to broadening, is also obstructed.



$$H_B = \frac{2\gamma D}{v}$$

Equation 1.8

In the materials literature, the obstruction factor is taken to be the porosity,  $\varepsilon$ , scaled by a tortuosity factor,  $q$ , which is approximately 0.7.<sup>38</sup> This concept applies broadly to mass transport, first recognized by James Clerk Maxwell in the nineteenth century for electric current through porous media<sup>39</sup>. Our group tested the idea of porosity unifying the obstruction of diffusion and of ionic current in chromatographic media.<sup>40</sup> A series of capillaries packed with particles of varying diameter was prepared. The value of  $\gamma$  was measured optically by diffusion of a small molecule, fluorescein, in the packed capillary versus in an open capillary. The porosity for each capillary was determined by measuring back pressure,  $\Delta P$ , as a function of mobile phase velocity, and calculating  $\varepsilon$  through the Kozeny-Carman equation:

$$\frac{\Delta P}{L} = \frac{180 \cdot \eta}{d_p^2} \frac{(1 - \varepsilon)^2}{\varepsilon^3} v$$

Equation 1.9

Further, ionic current was measured in the same packed versus open capillaries. There were no frits to add to the overall porosity. The three independent measurements of porosity were shown to agree, as illustrated in the graph of Figure 1.7. The experimental error obscures the small predicted effect of tortuosity on  $\gamma$ , hence  $\varepsilon$  is a reasonable approximation for  $\gamma$ . One can see that the porosity gradually increases with particle size since the larger particles do not pack as tightly, which also serves to illustrate why there is no set value of  $\gamma$ <sup>37</sup>.

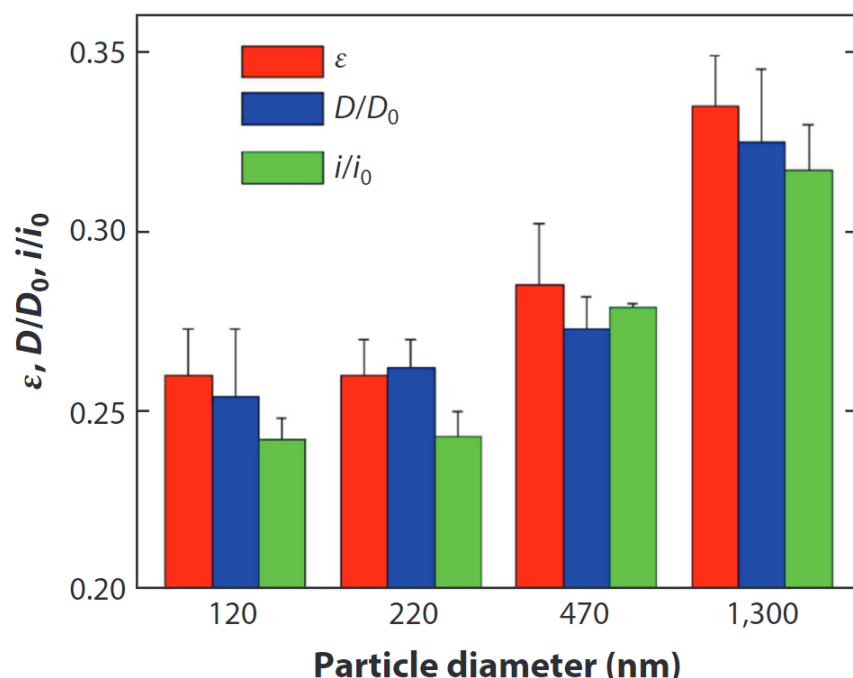


Figure 1.7. Data for capillary porosity ( $\epsilon$ ), the ratio of diffusion within the packed capillary vs. an open tubular capillary ( $D/D_0$ ), and the ratio for ionic current within the packed capillary vs. an open tubular capillary ( $i/i_0$ ). Adapted with permission from Rogers, et. al.<sup>40</sup> Copyright 2013, American Chemical Society.

The obstruction factor can become much smaller than  $\epsilon \cdot q$  when the interstitial space approaches the sizes of the molecules, which often happens for proteins.<sup>40</sup> A predictable decrease in diffusion is observed, and this will be discussed in more detail in the section on the contribution of intraparticle diffusion to the  $C$  term. The van Deemter plots of Figure 1.4 showed that the most urgent factor that needs attention is the  $C$  term. The plots also give a preview of one way to decrease the  $C$  term: use nonporous particles. This is detailed in the next subsection.

### 1.2.3 Contributions to the $C$ term

At higher flowrates, mass transport effects become the main contributors to peak broadening. While the advent of superficially porous and sub-2- $\mu\text{m}$  particles has lessened its impact, the  $C$  term remains a key consideration when working to reduce peak widths.

### ***Poiseuille Flow Profile***

The contribution from the Poiseuille flow profile,  $C_m$ , depicted in Figure 1.1, is unavoidable under pressure driven flow. It is the only contribution to  $C$  when particles are nonporous and desorption is fast. Since  $C_m$  appears to be significant based on the van Deemter plots of Figure 1.4, even for these sub-2- $\mu\text{m}$  particles, one might wonder if there is any room for improvement. Yan & Wang<sup>41</sup> used numerical simulations to determine how low of a plate height one could theoretically obtain if  $B$  and  $C_m$  were the only contributors to plate height. The simulations were for particles packed with face-centered cubic arrangement and no retention. The results indicated that the minimum plate height at optimal velocity is proportional to particle diameter when only  $B$  and  $C_m$  contribute to  $H$ :

$$H_{\min} = 0.084 \cdot d_p$$

Equation 1.10

Using this equation, for 1.5- $\mu\text{m}$  particles,  $H_{\min} = 140$  nm, which predicts about a 100-fold improvement in efficiency compared to that depicted in Figure 1.4a, offering potentially 10 times higher resolution for protein separations. Yan and Wang further showed in the same paper that slip flow decreases the factor in Equation 1.10 from 0.084 to 0.059 by virtue of decreasing the velocity distribution.<sup>41</sup> Schure et al. showed that the minimum plate height increases only by about factor of two when particles are randomly packed;<sup>30</sup> therefore, crystalline packing is not a requirement for large improvements in plate height. Theory thus points to the possibility of much higher efficiency.

One might then ask why people do not use even smaller nonporous particles to gain higher surface area to decrease overloading and to gain even lower plate heights. Particles of 0.5  $\mu\text{m}$  would have a threefold-higher surface area than 1.5- $\mu\text{m}$  particles and also give a minimum plate height predicted by Equation 1.10 to be only 42 nm. Nonporous particles of 0.47  $\mu\text{m}$  have been investigated in capillaries to assess the possible advantage. By using trifunctional silanes to hold the particles together,<sup>42</sup> no frit was needed. Further, instrumental broadening was greatly decreased by injection via diffusion and then using on-column fluorescence microscopy for detection. Figure 1.8 confirms that a dramatic the improvement is gained for separation of a monoclonal antibody

and its aggregates, comparing the 0.5- $\mu\text{m}$  particles in a capillary to porous 1.7- $\mu\text{m}$  particles in a 2.1/50-mm column.<sup>43</sup> The resolution is about fourfold higher for the 0.5- $\mu\text{m}$  particles. This could be further improved by injecting a smaller amount of protein because the asymmetric peaks indicate overloading for the 0.5- $\mu\text{m}$  nonporous particles. Nonetheless, the improvement is already dramatic.

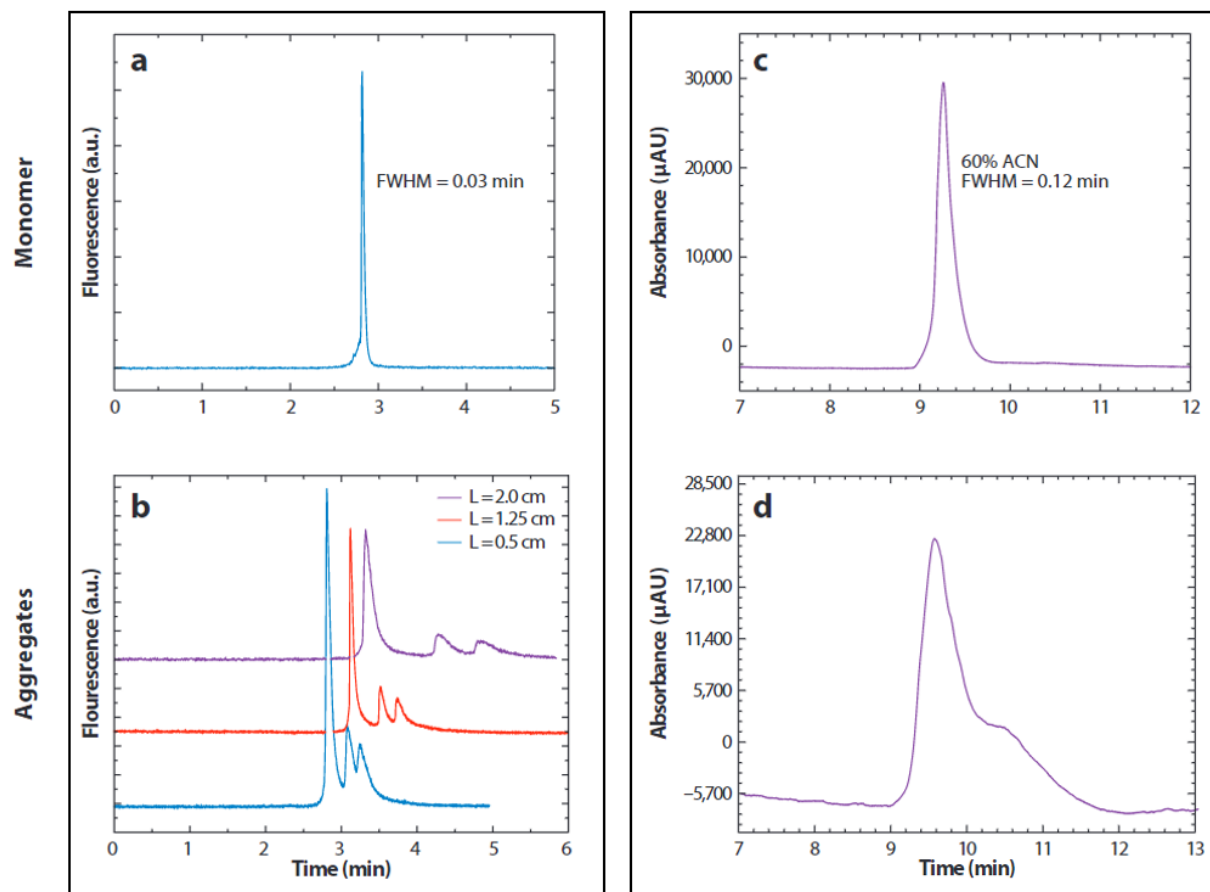


Figure 1.8. Comparison of capillary (left) and traditional UHPLC (right) columns for separation of an IgG4-type monoclonal antibody and its aggregates. Adapted with permission from Rogers, et. al.<sup>43</sup> Copyright 2013, American Chemical Society.

A plate height as small as 15 nm was observed for separation of labeled bovine serum albumin with a capillary packed with 0.47- $\mu\text{m}$  particles.<sup>44</sup> The plate height corresponds to  $0.032 \cdot d_p$ , which is more than twofold smaller than that predicted by the theory represented in Equation 1.10. The theory did not take into account the size of the protein, which causes further obstruction since the volume available to the protein is decreased. This was investigated quantitatively, showing that

the obstruction factor has a second term that become significant for such small particles.<sup>40</sup> The value of  $R$  is the local radius of the interstitial space and  $r$  is the radius of the protein. Using the idea that diffusion stops when the protein is in contact with the surface, we introduced the factor  $[(R - r)/R]^2$  to account for the volume fraction accessible to the protein when not in contact with the surface:

$$\gamma = \varepsilon \cdot \left( \frac{R - r}{R} \right)^2$$

Equation 1.11

The parentheses have the same factor as in Giddings' textbook description of the equilibrium constant for size exclusion chromatography, which equals the accessible volume fraction.<sup>45</sup> The value of  $R$  is assumed to be the hydrodynamic radius of the medium, which is the radius an open capillary would have if it had the same surface area to volume ratio as the packed bed.<sup>46</sup>

$$R = \frac{d_p}{3} \frac{\varepsilon}{1 - \varepsilon}$$

Equation 1.12

Using Equation 1.12 to obtain  $R$  for Equation 1.11, which describes obstructed diffusion well,<sup>40</sup> would reduce the proportionality constant to in Equation 1.10 to 0.068, still giving twofold disagreement between experiment and the numerical simulations. Beyond obstruction of diffusion, another consequence of finite protein size relative to the interstitial space is that the protein cannot diffuse all the way to the intersection points between particles due to its nonzero dimensions. These regions contribute the most to the plate height because they are furthest from the center of the flow stream. The numerical simulations that gave Equation 1.10 do not account for this factor in plate height; hence Equation 1.10 is an overestimate of  $H_{\min}$ .

Smaller particles 350 nm in diameter were shown to obstruct diffusion by an order of magnitude,<sup>34</sup> which is more obstruction than indicated by Equation 1.11 and Equation 1.12. Denaturation of the protein to increase its radius is one possible explanation for the surprise.

Another explanation is that the model for  $R$  in Equation 1.12 is not sufficiently accurate to avoid large errors in subtracting similar numbers in Equation 1.11. The 350-nm particles also gave a measured  $A$  term of  $0 \pm 1$  nm in electrochromatography, and no  $C$  term was detectable.<sup>34</sup> It would be interesting to investigate these very small particles for HPLC.

These studies show that when the interstitial space approaches molecular dimensions, extremely low plate heights are possible. But using such small particle increases back pressure. The back pressure problem is partially alleviated because these materials give slip flow, mentioned earlier, which enhances flow rate when the fluid is nonwetting on the surface.<sup>44</sup> A fivefold enhancement in flow rate was shown for water in capillaries packed with hydrophobic 0.5- $\mu$ m particles, and flow rate enhancement was shown to be inversely proportional to particle diameter.<sup>47</sup> Smaller particles would also increase surface area. New instrumentation would need to be designed to accrue the advantages of submicrometer silica particles in HPLC.

### ***Intraparticle Diffusion***

The van Deemter plots of Figure 1.4 compared porous and nonporous particles for a protein separation. Assuming that the only difference in  $C$  is from intraparticle diffusion, the plots illustrate visually that intraparticle diffusion contributes about twice as much to the  $C$  term as other contributions to  $C$ . This has made intraparticle diffusion a target for improving protein separations, and this improvement is much of the story of HPLC so far in the twenty-first century. Equation 1.5 described broadening from intraparticle diffusion as increasing with the ratio  $d_p^2/D$ , as one would intuitively expect from Stokes' law ( $\sigma^2 = 2Dt$ ), but with the proportionality factor  $\omega_{ip}$ :

$$H_{ip} = \omega_{ip} \frac{d_p^2}{D} v$$

Equation 1.13

Horvath & Lin<sup>48</sup> derived an expression for  $\omega_{ip}$  in terms of retention factor, the ratio of intraparticle porosity to total porosity,  $\psi$ , and tortuosity,  $q$ :

$$\omega_{ip} = \frac{\psi}{30 \cdot q \cdot (1 + \psi)^2}$$

Equation 1.14

Assuming tortuosity to be 0.7, as in the earlier discussion of obstructed diffusion,  $C_{ip}$  is calculated to be 4 ms for the 1.5- $\mu\text{m}$  particles and the usual approximation of  $D = 10^{-6}$ . The van Deemter plots of Figure 1.4 allow an estimation of  $C_{ip}$ . For the fully porous and nonporous particles, the estimated  $C$  values from the graph are 34 ms and 12 ms, respectively. The difference between the two  $C$  terms, 22 ms, equals the value of  $C_{ip}$  since contributions to  $H$  are additive. This assumes that the other factors affecting  $C$  are the same for the two columns. The disparity between the prediction from Equation 1.13 and the data in Figure 1.4a could be because of the data being obtained under conditions of retention, whereas the equation was derived for no retention. In addition, the equation does not account for obstruction due to the nonzero size of the protein relative to the pores.

Equation 1.13 illustrates why sub 2- $\mu\text{m}$  particles were introduced, and commercial columns were shown to approach the theoretically predicted improvements in efficiency.<sup>28</sup> The back pressure increases with the inverse square of particle diameter, as earlier illustrated by Equation 1.9. This necessitated the development of instruments with higher pump pressures. Instruments had pressure limits on the order of 4,000 psi, which is insufficient for the submicrometer particles. Newer instruments delivered pressures on the order of 10,000 psi, and the technique was initially called UPLC, then was called UHPLC, and is often called HPLC once again. With particle diameters being half that of the 3.5- $\mu\text{m}$  particles used with the HPLC instruments, logic would dictate that HPLC instruments should have delivered 16,000 psi. Only in the last few years have they reached such pressures; therefore, shorter columns, e.g., 5 cm, became common in UHPLC until recently. Equation 1.4 shows resolution to be proportional not just to  $H^{1/2}$  but to  $(H/L)^{1/2}$ . Because of pressure limits, the larger particles outperform smaller particles in resolution by virtue of column length. This is why larger particles are commonly used in proteomics. What the smaller particles do offer is speed: resolution per minute is higher. Also, sensitivity is higher with shorter columns since peaks broaden in proportion to  $L^{1/2}$ .

Instruments with increasing pressure have been introduced over the last decade. These can also cause problems: higher pressure changes retention times for proteins due to denaturation.<sup>49</sup>

Despite the higher pressure now available commercially, particle diameter has not decreased significantly. One reason is because frictional heating decreases efficiency, and this is noticeable for efficient small-molecule separations.<sup>50-52</sup> The power,  $W$ , used to force liquid to flow through the column by the pressure,  $P$ , at a volume flow rate,  $Q$ , releases the energy in the form of heat:

$$W = P \cdot Q$$

Equation 1.15

The walls of stainless-steel columns remain close to the thermostat temperature due to the high thermal conductivity of metal, giving rise to a temperature gradient from the center of the packed bed to the walls. Both the equilibrium constant for adsorption and the mobile phase viscosity depend on temperature, thus imparting a radial heterogeneity of retention times across the column, thereby decreasing column efficiency. Frictional effects are not noticeable for proteins because mass transport contributes more than frictional heating.<sup>53</sup> Frictional heating is decreased for slip flow, which occurs with submicrometer nonporous particles; for example, for a flow enhancement of 5 from slip flow, the frictional heating calculated from Equation 1.15 would be decreased by a factor of 5. The difficulty of making ever smaller porous particles, along with the onset of frictional heating for porous particles, has so far slowed the work in making smaller particles.

A bigger factor that has slowed efforts in making smaller porous particles was the commercialization of fused-core particles, illustrated in Figure 1.9. These particles decrease the distance for diffusion through the pores, giving a decrease in variance through Stokes' law. Because the distance for intraparticle diffusion is no longer strapped to particle size, larger particles can be used to allow longer columns without requiring higher pressures. The surface area is lower than that of totally porous particles but still higher than that for nonporous particles.



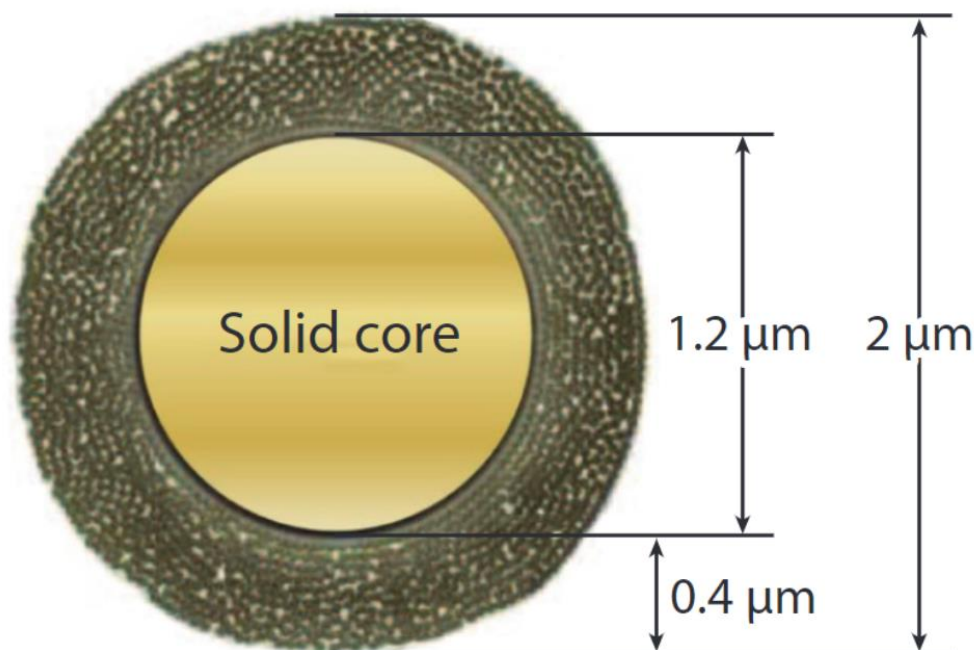


Figure 1.9. Illustration of the structure of a 2  $\mu\text{m}$  fused-core particle. Adapted with permission from DeStefano, et. al.<sup>29</sup> Copyright 2014, Elsevier.

A van Deemter plot in Figure 1.10 compares fused-core particles of with totally porous particles to illustrate that these give lower  $C$  terms than sub-2- $\mu\text{m}$  totally porous particles despite being larger in diameter. Specifically, comparing the curves for the totally porous 1.7- $\mu\text{m}$  particles (stars), with the 2.0- $\mu\text{m}$  fused-core particles for which the shell is shown to be 0.4  $\mu\text{m}$  thick (triangles), the  $C$  term is nearly fivefold lower for the fused core particles. This demonstrates the effect of the shorter diffusion distance in the fused particles. The minimum plate height is lower by almost a factor of two, and the optimal velocity is higher, giving more separation speed. The 2.7- $\mu\text{m}$  fused-core particles give similar efficiency to the 1.7- $\mu\text{m}$  totally porous particles but would allow a longer column length of  $(2.7/1.7)^2 = 2.5$ -fold for the same back-pressure, giving 2.5-fold more plates. It is clear why the fused-core particles are currently a dominant technology.

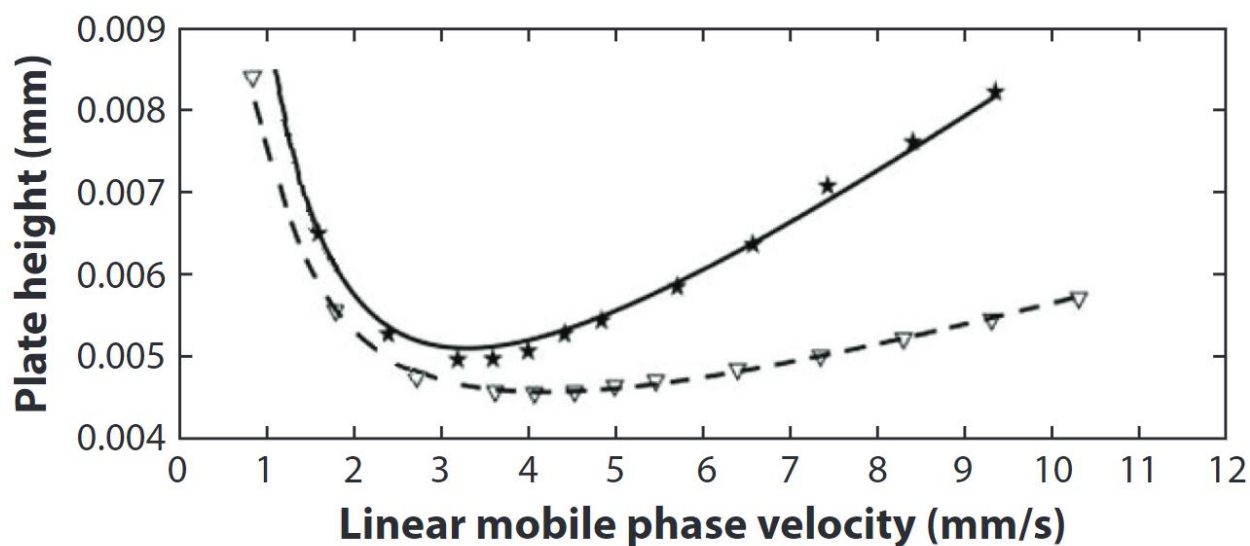


Figure 1.10. van Deemter plots for columns containing fused core (★) and fully porous (▽) particles. Adapted with permission from DeStefano, et. al.<sup>29</sup> Copyright 2014, Elsevier.

In the past, particles with an average pore size of 300 Å had been considered to be wide-pore particles, and these were widely used for protein HPLC. In size-exclusion chromatography, antibodies are mostly excluded from these particles. By the same token, they would be excluded from 300-Å RPLC particles, and likely even more excluded since denaturation by the organic solvent would increase their sizes. With the growth of mAbs in the pharmaceutical industry, it has become necessary to increase pore size, and this advance has been made recently. Fused-core particles with pore diameters large as 1,000 Å are now commercially available. The effect of pore diameter on mAb separation is shown in Figure 1.11. The progressively wider pores, from 300 to 400 to 1,000 Å, show progressively more proteoforms. One wonders whether wider pores yet would reveal even more.

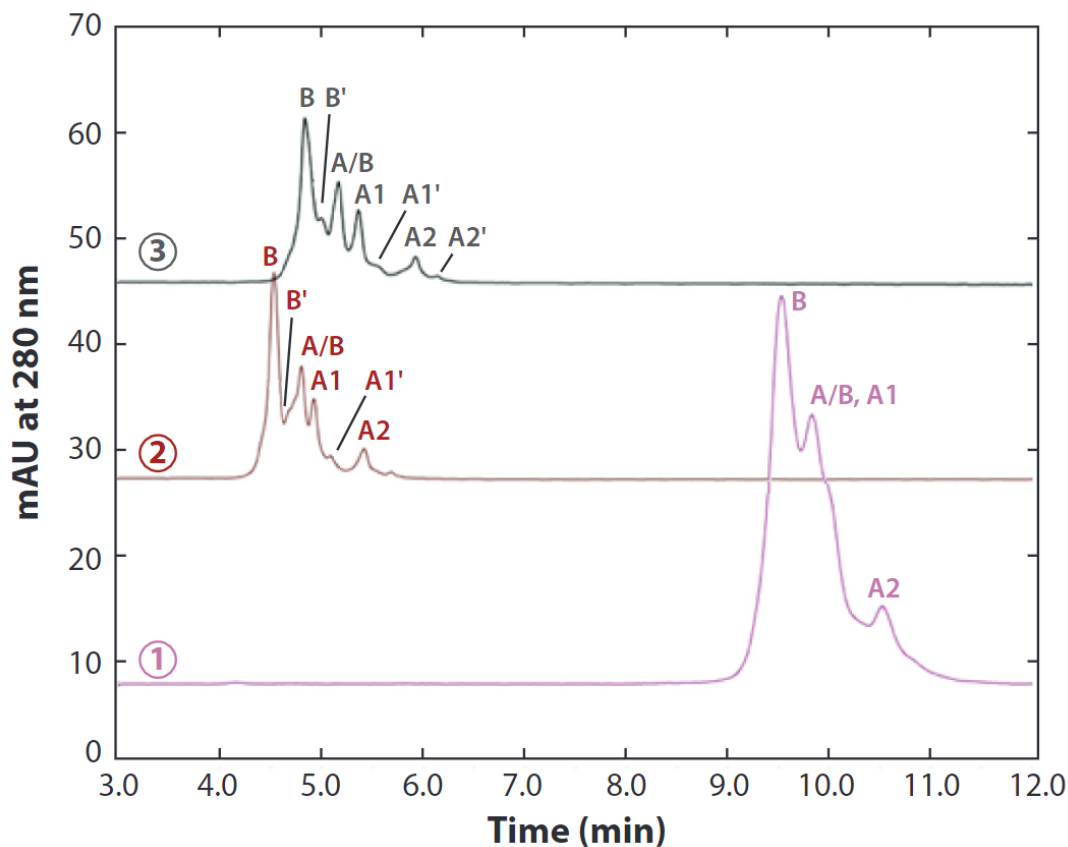


Figure 1.11. Comparison of the separation of mAb disulfide isoforms using columns containing particles of varying pore-size. From bottom to top: 1000 Å, 400 Å, and 300 Å. Adapted with permission from Wei, et. al.<sup>54</sup> Copyright 2017, Elsevier

#### 1.2.4 Slow Desorption and Reduction of Tailing

Giddings' textbook<sup>45</sup> provides an equation for the contribution to the plate height due to slow desorption from the bonded phase,  $H_s$ . The equation was derived using the random walk model and first order desorption kinetics, showing that  $H_s$  is proportional to the desorption time constant,  $\tau_{des}$ :

$$H_s = 2 \cdot \frac{k}{(1+k)^2} \tau_{des} v$$

Equation 1.16

Values for  $\tau_{\text{des}}$  of proteins are not well known, although single-molecule spectroscopy is beginning to provide these data.<sup>55</sup> Temperature studies of HPLC separations of mAbs show little if any change in peak width as temperature is changed from 40°C to 80°C, suggesting that  $C_s$  might not be a limiting factor for efficiency.<sup>56</sup> Further, in these same studies, selectivity decreases twofold from lowest to highest temperature over this range, indicating that lower temperature should give better resolution. Nevertheless, people use 80°C for mAb separations despite the lower resolution because quantitation is better, as indicated by a slight loss in peak area as temperature is lowered. In the results shown earlier for 0.5- $\mu\text{m}$  particles, the mAb separation was run at room temperature, yet no accumulation of protein was observed on the material in the fluorescence images. It could be that the trifunctional silanes yield less protein loss. Another possibility is suggested by the work of Eschelbach & Jorgenson: higher pressure gives higher protein recovery.<sup>57</sup> A third possibility is that the protein is lost on the frits or tubing rather than on the particles. The latter is documented to be the case in size exclusion chromatography, which is performed at lower temperatures.<sup>58</sup> Advances will likely bring HPLC of mAbs closer to room temperature for higher resolution, and it will be interesting to see how many proteoforms in Figure 1.11 will then be identified.

No discussion of  $C_s$  in RPLC would be complete without a mention of mixed-mode adsorption, which has been studied extensively for small molecules. On the silica surface, the low-abundance, isolated silanols that have low  $\text{pK}_a$  cause tailing because these give large equilibrium constants so that typical HPLC concentrations are in the nonlinear part of the Langmuir adsorption isotherm.<sup>59</sup> The isolated silanols also cause peak broadening even under nonoverloading conditions.<sup>60</sup> The isolated silanols were shown to be due to topographical asperities;<sup>61</sup> combining spectroscopic imaging and atomic force microscopy, no strong sites are observed in topographically smooth regions.<sup>62</sup> The trifunctional silanes discussed earlier were shown to block the dissociation of isolated silanols even on low quality silica that has large amounts of isolated silanols, provided that the amount of adsorbed water is controlled.<sup>63</sup> The unusually high efficiency of the mAb separation shown in Figure 1.8, obtained using trifunctional silanes and high-quality silica, indicates that the  $C_s$  term can be made negligible.

The isolated silanols, by virtue of their high acidity, have necessitated the use of trifluoroacetic acid (TFA) to neutralize the isolated silanols, thus minimizing peak broadening. TFA causes much lower sensitivity when using electrospray ionization for mass spectrometry due to its amphiphilic

structure and its propensity for ion pairing with proteins. For mass spectrometry, formic acid or acetic acid are preferred, but these have  $pK_a$  values that are several units above that for TFA, giving much poorer HPLC resolution due to peak broadening.<sup>64</sup> Difluoroacetic acid has been used as a compromise, giving HPLC performance almost as good as that of TFA, but ion suppression can be nearly as bad as that of TFA.<sup>65</sup> Polymer particles avoid this problem, but their high compressibility precludes a small-particle format.<sup>66</sup>

### 1.3 Hydrophilic Interaction Liquid Chromatography

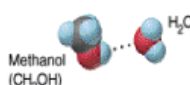
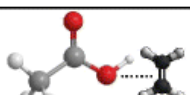
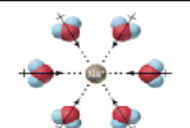
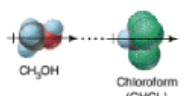
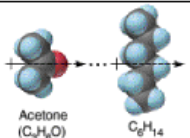
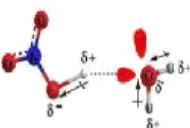
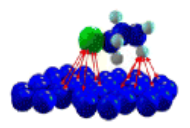
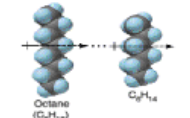
The early days of HPLC were marked by two competing separation types of chromatography: “normal-phase” and “reversed-phase”.<sup>67</sup> Normal-phase chromatography (NPLC) relies on a polar stationary phase, often bare silica, and uses an organic mobile phase. Compounds are eluted off of a NPLC column in order based on their polar character, with the least polar compounds seeing the shortest retention time.<sup>68</sup>

As its name suggests, reversed-phase HPLC (RPLC) employs an opposing type of chromatographic bonded phase. A RPLC column utilizes a hydrophobic stationary phase to selectively retain compounds based on their hydrophobicity, with compounds typically eluting in order starting with the least hydrophobic analyte.<sup>69</sup> Unlike NPLC, the mobile phase is not purely organic; it typically contains an aqueous component.<sup>70</sup> In this case, the aqueous component is considered a weak solvent, as increasing the fraction of aqueous solvent will lead to greater retention of the compounds on the column.<sup>71</sup> RPLC is by far the most popular separation mode for now,<sup>72</sup> being used for over 90% of all chromatographic separations as of 2019.<sup>73</sup>

In the 1990s, a new variety of chromatography emerged. Coined “Hydrophobic Interaction Liquid Chromatography”, or HILIC, this method utilizes a polar stationary phase like NPLC but uses an aqueous-organic mobile phase like with RPLC.<sup>71, 74</sup> In contrast with RPLC, increasing the concentration of water in the mobile phase leads to shorter retention times on a HILIC stationary phase.<sup>75</sup>

The underlying retention mechanism for HILIC is highly contested, and recent evidence suggests that it is significantly more complicated than that for RPLC.<sup>75, 76</sup> It is theorized that there may be a combination of factors involved, with the strength and character of different interactions based upon both the bonded phase and the analyte.<sup>77</sup> An exhaustive list of these interactions is provided by Kaliszan,<sup>78</sup> and summarized in Table 1.1 below:

Table 1.1 Hypothesized Retention Mechanisms Responsible for HILIC Separations. Courtesy of Buszewski, et. al.<sup>75</sup>

Type of interaction		Characterization	Energy [kJ·mol <sup>-1</sup> ]	Example system
Chemical interactions	Hydrogen bonding	formed between hydrogen of the protodonor group and atom being hydrogen acceptor, can be formed within the same molecule, as well as between two different	- (4 - 17)	 Methanol (CH <sub>3</sub> OH)
	Donor – acceptor interactions	occurs between pairs of electron donor (Lewis base) and acceptor (Lewis acid)	- (4 - 17)	
Physical interactions	Ion – dipole	ion acts on electrically neutral molecule; leads to a multicomponents	- (4 - 17)	
	Dipole – dipole	force between two electrically neutral particles, but having determined dipole moments	- (4 - 17)	
	Dipole-induced dipole	forces between the molecule possesses clear dipole moment and non-polar molecule	- (4 - 17)	
	Temporary dipole-induced dipole	two electrically neutral particles, if they come close together, will attract on the electrostatic forces way	- (4 - 17)	
Intermolecular interactions (Van der Waals forces)		weak forces of attraction between the fragments of individual molecules, declining rapidly with increasing distance between the interacting particles, do not lead to permanent connections	- (2 - 4)	
Hydrophobic interactions		forces operating in the aquatic environment between molecules with low affinity for water	- 4	

In recent years, HILIC has grown in popularity<sup>75</sup> for multiple reasons. Strongly hydrophilic molecules that would not be retained in RPLC separations can now be separated, a list which includes many key pharmaceutical compounds and biomarkers.<sup>79</sup> HILIC mobile phases generally contain >50% acetonitrile and are therefore low-viscosity, which lessens the need for ultra-high

pressure pumps.<sup>80</sup> These acetonitrile mixtures also tend to be more volatile than the typical RPLC mobile phase, and as a result provide greater sensitivity in liquid chromatography-mass spectrometry (MS) analyses<sup>79, 81</sup> for reasons that will be discussed later in this chapter.

## 1.4 Nano-LC

As is the case with so many technologies, there is a major push for miniaturization in the field of chromatography. Nano-scale HPLC and UHPLC techniques, commonly referred to as nanoLC, offer great promise in advancing the frontier of chromatographic methods

The main advantage provided by nano-scale separations over traditional HPLC analyses, is a drastic increase in sensitivity.<sup>82</sup> The increased sensitivity can be used to analyze precious samples with minimal waste. It can be leveraged to detect minority species present in complex mixtures, which is of great interest to biomedical researchers who must contend with the trouble of detecting biomarkers in human plasma that span a concentration range of twelve orders of magnitude.<sup>83</sup> Capillary-based nanoLC instrumentation coupled to mass spectrometer has been reported to identify in excess of 4,000 proteins from a single analysis,<sup>84</sup> with over 12,000 unique peptides identified in another study.<sup>85</sup>

The increase in sensitivity is largely due to the significant decrease in volumetric flowrate compared to standard HPLC techniques. While HPLC and UHPLC analyses are generally run at flowrates measured in hundreds of microliters to several milliliters per minute, nanoLC analyses utilize flowrates three to four orders-of magnitude lower.<sup>86</sup> To put this in perspective: with a typical flowrate on the order of 100 nanoliters per minute, it would take over six years to fill a 12 oz soda can.

An additional, and often overlooked, advantage to nano-scale separations is on the environmental side. Organic mobile phases are often extremely toxic and can be devastating to aquatic life in case of improper disposal.<sup>87</sup> Disposal costs for these solvents can be formidable, with the disposal cost of the commonly-used solvent acetonitrile greatly exceeding its purchase price.<sup>88</sup> By greatly decreasing the volume of mobile phase used, these concerns can be nearly eliminated.

While the advantages of nanoLC over traditional HPLC methods are numerous, there are still several significant drawbacks. When working with volumes this low, even microscopic void volumes can introduce broadening that renders separation impossible.<sup>89</sup> Nano-scale

instrumentation is typically more complex than that for traditional HPLC, which greatly increases prices and potential points of failure.<sup>90</sup> There is an additional cost in diminished reproducibility; retention time variability has been reported as increasing nearly two orders of magnitude when compared to standard-flow methods.<sup>91</sup> Clearly there is room for improvement in this nascent technique, and once these hurdles can be addressed there is no doubt that nanoLC will become a dominant technology in the world of analytical chemistry.

### 1.5 Electrospray Ionization – Mass Spectrometry

The coupling of mass spectrometry to HPLC separations enables a robust analysis that can provide a wealth of data. The ability to glean information about mass can prove invaluable in identifying and characterizing an analyte of interest. In addition, analytes that do not absorb UV photons and are thus invisible to photodetectors can often be monitored using a mass spectrometer as they elute off the column.<sup>92</sup> As a result, liquid chromatography-mass spectrometry (LCMS) instruments are a common fixture in modern analytical laboratories.

The most common means for interfacing a mass spectrometer to the eluent of a HPLC column is through electrospray ionization,<sup>93</sup> or “ESI”. This technique relies on a charged needle emitter through which the post-column mobile phase flows.<sup>94</sup> As the droplets are sprayed out of the emitter, (Figure 1.12) the concentration of charge on their surface increases through solvent evaporation.<sup>95</sup> Once the surface charge reaches a critical point, Coulomb fission occurs, splitting the droplet into multiple smaller, charged droplets.<sup>96</sup> This process repeats multiple times before the desolvated ions reach the inlet of the mass spectrometer, where they pass through ion optics on their way to the mass analyzer.



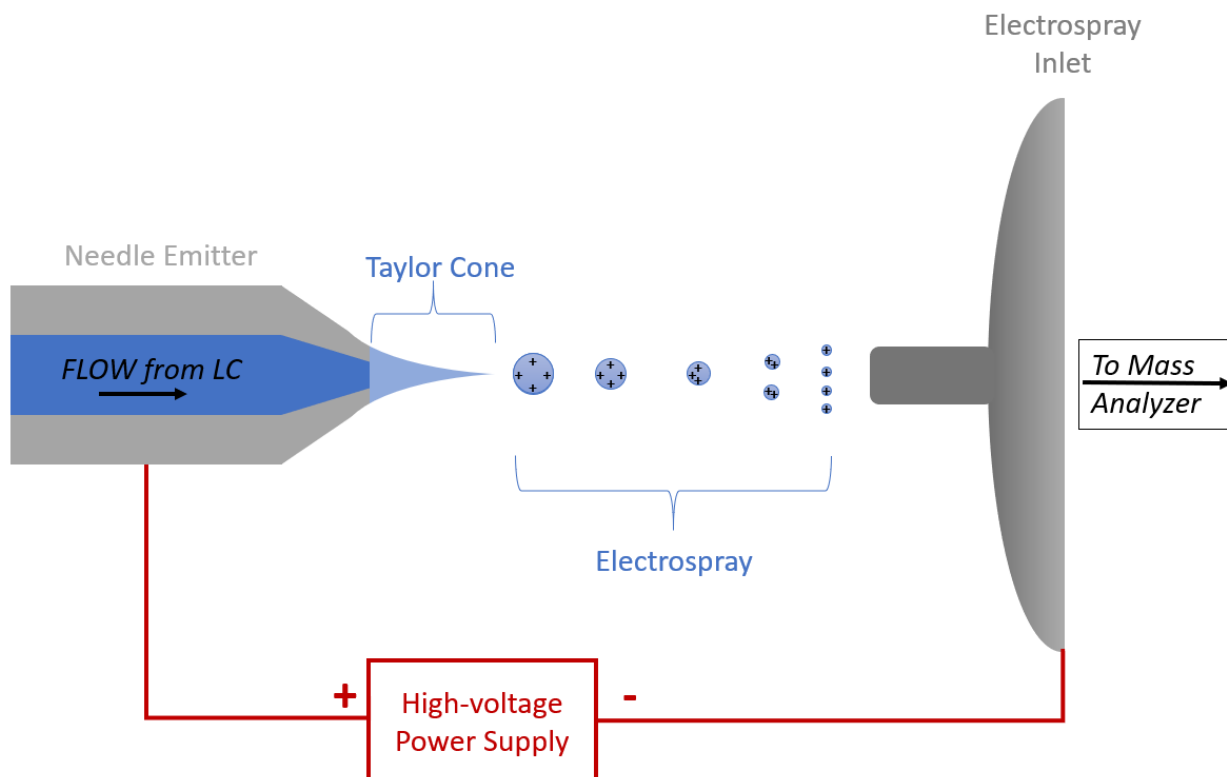


Figure 1.12. An illustration of the electrospray process used in analyte ionization for detection with a mass spectrometer.

As discussed earlier, HILIC typically relies on high concentrations of organic solvent in the mobile phase. Acetonitrile is significantly more volatile than water,<sup>97</sup> which increases the electrospray efficiency as the droplets undergo evaporation much quicker and more of the analyte ions are completely desolvated in the Taylor cone and liquid jet.<sup>98</sup> This presents a major advantage of using HILIC separation modes over traditional RPLC or ion-exchange chromatography methods which generally utilize a more aqueous, less volatile mobile phase.<sup>6</sup>

A key drawback that must be considered when using mass spectrometry-based detection is the limited ability to quantify the amount of analyte detected.<sup>99</sup> Ion suppression can be caused by other interfering species that co-elute with the analyte of interest, artificially decreasing the number of ions detected by the instrument.<sup>100</sup> Furthermore, ionization efficiencies can differ among molecular species,<sup>101</sup> so calibration curves should be created for each analyte. Despite these limitations, the utility of a mass spectrometry-based detection method cannot be overstated.

## 1.6 Research Objectives

The aim of this research was to develop a platform for separating and identifying intact glycoproteins at sub-femtomole levels. Separation of the glycoproteins was achieved using improved bonded phases for nanoHILIC, as discussed in Chapter 3. The platform was then adapted for use with mass spectrometry to enable identification and detection of intact, unlabeled proteins, which is presented in Chapter 4. Additional work is currently underway to utilize this platform in characterizing the purity of therapeutic proteins for quality control purposes.

## 1.7 References

1. Weil, H.; Williams, T. I., Early History of Chromatography. **1951**, *167* (4257), 906-907.
2. Siu, S. C.; Chia, C.; Mok, Y.; Pattnaik, P., Packing of Large-scale Chromatography Columns with Irregularly Shaped Glass Based Resins Using a Stop-flow Method. *American Institute of Chemical Engineers Biotechnol. Prog* **2014**, *30* (6), 1319-1325.
3. Gama, M. R.; Collins, C. H.; Bottoli, C. B. G., Nano-Liquid Chromatography in Pharmaceutical and Biomedical Research. *J Chromatogr Sci* **2013**, *51* (7), 694-703.
4. Zotou, A., An overview of recent advances in HPLC instrumentation. *Open Chemistry* **2012**, *10* (3).
5. Wilson, K.; Walker, J. M., Principles and techniques of biochemistry and molecular biology. In *Principles and techniques of biochemistry and molecular biology*, Cambridge University Press: Cambridge, UK, 2009.
6. Horvath, C. G.; Lipsky, S. R., Use of liquid ion exchange chromatography for the separation of organic compounds. *Nature* **1966**, *211* (5050), 748-9.
7. Swartz, M. E. *Ultra Performance Liquid Chromatography (UPLC): An Introduction*; 2005.
8. McQueen, C. A., *Comprehensive toxicology*. 2nd ed. ed.; Elsevier/Academic Press: Amsterdam, 2010.
9. The LC Handbook-Guide to LC Columns and Method Development. Agilent Technologies: USA, 2016.
10. Moldoveanu, S.; David, V., Estimation of the phase ratio in reversed-phase high-performance liquid chromatography. *Journal of Chromatography A* **2015**, *1381*, 194-201.
11. Barth, H. G., Chromatography Fundamentals, Part IV: Origin of Theoretical Plates—Fractional Distillation and Countercurrent Distribution Extractions. *LCGC North America* **2018**, *36* (8), 532-535.

12. Van Deemter, J. J.; Zuiderweg, F. J.; Klinkenberg, A., Longitudinal diffusion and resistance to mass transfer as causes of nonideality in chromatography. *Chemical Engineering Science* **1956**, 50 (24), 3869-3882.
13. Gritti, F.; Guiochon, G., The van Deemter equation: Assumptions, limits, and adjustment to modern high performance liquid chromatography. *Journal of Chromatography A* **2013**, 1302, 1-13.
14. Knox, J. H.; Scott, H. P., B and C terms in the Van Deemter equation for liquid chromatography. **1983**, 282, 297-313.
15. Singh, R., HPLC method development and validation- an overview. *Journal of Pharmaceutical Education and Research* **2013**, 4 (1), 26-33.
16. Majors, R., Developments in HPLC column packing design. *LCGC North America* **2006**, 24.
17. Fetzer, J. C.; Biggs, W. R., Retention behavior of large polycyclic aromatics in bonded-phase high-performance liquid chromatography. *J Chromatogr* **1987**, 386, 87-101.
18. Kirkland, J. J.; Dilks, C. H.; Destefano, J. J., Normal-Phase High-Performance Liquid-Chromatography with Highly Purified Porous Silica Microspheres. *Journal of Chromatography* **1993**, 635 (1), 19-30.
19. Kirkland, J. J.; Truszkowski, F. A.; Dilks, C. H., Jr.; Engel, G. S., Superficially porous silica microspheres for fast high-performance liquid chromatography of macromolecules. *J Chromatogr A* **2000**, 890 (1), 3-13.
20. Beck, A.; Wurch, T.; Bailly, C.; Corvaia, N., Strategies and challenges for the next generation of therapeutic antibodies. *Nature Reviews Immunology* **2010**, 10, 345+.
21. Pathak, Y.; Benita, S., *Antibody-mediated drug delivery systems concepts, technology, and applications*. Wiley: Hoboken, N.J., 2012.
22. Philippidis, A. Top 15 best-selling drugs of 2018. <https://www.genengnews.com/lists/top-15-best-selling-drugs-of-2018/>.
23. Hawkrige, A. M.; Muddiman, D. C., Mass Spectrometry–Based Biomarker Discovery: Toward a Global Proteome Index of Individuality. *Annu. Rev. Anal. Chem.* **2009**, 2 (1), 265-277.
24. Toby, T. K.; Fornelli, L.; Kelleher, N. L., Progress in Top-Down Proteomics and the Analysis of Proteoforms. *Annu. Rev. Anal. Chem.* **2016**, 9 (1), 499-519.
25. Snyder, L. R.; Stadalius, M. A.; Quarry, M. A., Gradient elution in reversed-phase HPLC-separation of macromolecules. *Analytical Chemistry* **1983**, 55 (14), 1412A-1430A.

26. Gritti, F., General theory of peak compression in liquid chromatography. **2016**, *1433*, 114-122.
27. Wu, N.; Liu, Y.; Lee, M. L., Sub-2  $\mu\text{m}$  porous and nonporous particles for fast separation in reversed-phase high performance liquid chromatography. *Journal of Chromatography A* **2006**, *1131* (1), 142-150.
28. de Villiers, A.; Lestremieu, F.; Szucs, R.; Gélébart, S.; David, F.; Sandra, P., Evaluation of ultra performance liquid chromatography. Part I. Possibilities and limitations. *Journal of chromatography. A* **2006**, *1127* (1-2), 60.
29. Destefano, J. J.; Boyes, B. E.; Schuster, S. A.; Miles, W. L.; Kirkland, J. J., Are sub-2 $\mu\text{m}$  particles best for separating small molecules? An alternative. *Journal of Chromatography A* **2014**, *1368*, 163-172.
30. Schure, M. R.; Maier, R. S.; Kroll, D. M.; Ted Davis, H., Simulation of ordered packed beds in chromatography. *Journal of Chromatography A* **2004**, *1031* (1-2), 79-86.
31. De Vos, J.; Broeckhoven, K.; Eeltink, S., Advances in Ultrahigh-Pressure Liquid Chromatography Technology and System Design. *Anal. Chem.* **2016**, *88* (1), 262-278.
32. Farkas, T.; Guichon, G., Contribution of the radial distribution of the flow velocity to band broadening in HPLC columns. *Analytical Chemistry* **1997**, *69* (22), 4592-4600.
33. Patel, K.; Jerkovich, A.; Link, J.; Jorgenson, J., In-depth characterization of slurry packed capillary columns with 1.0- $\mu\text{m}$  nonporous particles using reversed-phase isocratic ultrahigh-pressure liquid chromatography. *Analytical Chemistry* **2004**, *76* (19), 5777-5786.
34. Wei, B.; Malkin, D. S.; Wirth, M. J., Plate heights below 50 nm for protein electrochromatography using silica colloidal crystals. *Analytical chemistry* **2010**, *82* (24), 10216.
35. Rogers, B. J.; Birdsall, R. E.; Wu, Z.; Wirth, M. J., RPLC of intact proteins using sub-0.5  $\mu\text{m}$  particles and commercial instrumentation. *Analytical chemistry* **2013**, *85* (14), 6820.
36. Zhang, Z.; Wu, Z.; Wirth, M. J., Polyacrylamide brush layer for Hydrophilic Interaction Liquid Chromatography of intact glycoproteins. *J Chromatogr A* **2013**, *1301*, 156-61.
37. Knox, J. H.; McLaren, L., A New gas Chromatographic Method for Measuring Gaseous Diffusion Coefficients and Obstructive Factors. *Analytical Chemistry* **1964**, *36* (8), 1477-1482.
38. Miyabe, K.; Guiochon, G., Surface diffusion in reversed-phase liquid chromatography. *Journal of Chromatography A* **2010**, *1217* (11), 1713-1734.
39. Maxwell, J., A Treatise on Electricity and Magnetism. *Nature* **1873**, *7* (182), 478.

40. Rogers, B. J.; Wirth, M. J., Obstructed diffusion in Silica colloidal crystals.(Report). *Journal of Physical Chemistry A* **2013**, *117* (29), 6244-6249.
41. Yan, X.; Wang, Q., Numerical investigation into the effects of ordered particle packing and slip flow on the performance of chromatography. *Journal of Separation Science* **2013**, *36* (9-10), 1524-1529.
42. Wirth, M.; Fairbank, R.; Fatunmbi, H., Mixed self-assembled monolayers in chemical separations. *Science* **1997**, *275* (5296), 44-7.
43. Rogers, B. J.; Birdsall, R. E.; Wu, Z.; Wirth, M. J., RPLC of Intact Proteins Using Sub-0.5  $\mu\text{m}$  Particles and Commercial Instrumentation. *Analytical Chemistry* **2013**, *85* (14), 6820-6825.
44. Wei, B.; Rogers, B. J.; Wirth, M. J., Slip flow in colloidal crystals for ultraefficient chromatography.(Report). *Journal of the American Chemical Society* **2012**, *134* (26), 10780-10782.
45. Giddings, J. C., *Unified separation science*. Wiley: New York, 1991.
46. Bird, R. B.; Stewart, W. E.; Lightfoot, E. N.; Meredith, R. E., Transport Phenomena. *Journal of The Electrochemical Society* **1961**, *108* (3), 78C.
47. Rogers, B. J.; Wirth, M. J., Slip flow through colloidal crystals of varying particle diameter. *ACS nano* **2013**, *7* (1), 725.
48. Horváth, C.; Lin, H. J., Band spreading in liquid chromatography. General plate height equation and a method for the evaluation of the individual plate height contributions. *Journal of Chromatography A* **1978**, *149* (C), 43-70.
49. Makarov, A. A.; Schafer, W. A.; Helmy, R., Use of pressure in reversed-phase liquid chromatography to study protein conformational changes by differential deuterium exchange. *Analytical chemistry* **2015**, *87* (4), 2396.
50. de Villiers, A.; Lauer, H.; Szucs, R.; Goodall, S.; Sandra, P., Influence of frictional heating on temperature gradients in ultra-high-pressure liquid chromatography on 2.1 mm I.D. columns. *Journal of Chromatography A* **2006**, *1113* (1-2), 84-91.
51. Fallas, M. M.; Hadley, M. R.; McCalley, D. V., Practical assessment of frictional heating effects and thermostat design on the performance of conventional (3  $\mu\text{m}$  and 5  $\mu\text{m}$ ) columns in reversed-phase high-performance liquid chromatography. *Journal of Chromatography A* **2009**, *1216* (18), 3961-3969.
52. Gritti, F.; Guiochon, G., Comparison of heat friction effects in narrow-bore columns packed with core-shell and totally porous particles. *Chemical Engineering Science* **2010**, *65* (23), 6310-6319.

53. Fekete, S.; Fekete, J.; Guillarme, D., Estimation of the effects of longitudinal temperature gradients caused by frictional heating on the solute retention using fully porous and superficially porous sub-2 $\mu$ m materials. *Journal of Chromatography A* **2014**, *1359*, 124-130.
54. Wei, B.; Zhang, B.; Boyes, B.; Zhang, Y. T., Reversed-phase chromatography with large pore superficially porous particles for high throughput immunoglobulin G2 disulfide isoform separation. *Journal of Chromatography A* **2017**, *1526*, 104-111.
55. Bishop, L. D.; Landes, C. F., From a Protein's Perspective: Elution at the Single-Molecule Level. *Accounts of chemical research* **2018**, *51* (9), 2247-2254.
56. Liu, H.; Jeong, J.; Kao, Y.-H.; Zhang, Y. T., Characterization of free thiol variants of an IgG1 by reversed phase ultra high pressure liquid chromatography coupled with mass spectrometry. *Journal of pharmaceutical and biomedical analysis* **2015**, *109*, 142-149.
57. Eschelbach, J. W.; Jorgenson, J. W., Improved protein recovery in reversed-phase liquid chromatography by the use of ultrahigh pressures. *Analytical chemistry* **2006**, *78* (5), 1697-1706.
58. Fekete, S.; Guillarme, D., Influence of connection tubing in modern size exclusion chromatography and its impact on the characterization of mAbs. *Journal of pharmaceutical and biomedical analysis* **2018**, *149*, 22-32.
59. Wirth, M. J.; Smith, E. A.; Anthony, S. R., Measurement and simulation of tailing zones of a cationic dye in analytical-scale reversed phase chromatography. *Journal of Chromatography A* **2004**, *1034* (1-2), 69-75.
60. Newby, J.; Legg, M. A.; Rogers, B.; Wirth, M., Annealing of silica to reduce the concentration of isolated silanols and peak tailing in reverse phase liquid chromatography. *J. Chromatogr. A* **2011**, *1218* (31), 5131-5135.
61. Cuppett, C. M.; Doneski, L. J.; Wirth, M. J., Irreversible adsorption of lysozyme to polishing marks on silica. *Langmuir* **2000**, *16* (18), 7279-7284.
62. Ludes, M. D.; Anthony, S. R.; Wirth, M. J., Fluorescence imaging of the desorption of dye from fused silica versus silica gel.(Author Abstract). *Analytical Chemistry* **2003**, *75* (13), 3073.
63. Wirth, M. J.; Peter Fairbank, R. W., Preparation of Mixed C18/C1 Horizontally Polymerized Chromatographic Phases. *Journal of Liquid Chromatography & Related Technologies* **1996**, *19* (17-18), 2799-2810.
64. McCalley, D. V., Comparison of peak shapes obtained with volatile (mass spectrometry-compatible) buffers and conventional buffers in reversed-phase high-performance liquid chromatography of bases on particulate and monolithic columns. **2003**, *987* (1-2), 17-28.

65. Yamamoto, E.; Ishihama, Y.; Asakawa, N., Application of partially fluorinated carboxylic acids as ion-pairing reagents in LC/ESI-MS. **2014**, *127*, 219-224.
66. Podgornik, A., Pressure drop in liquid chromatography. *Journal of Separation Science* **2019**, *42* (1), 72-88.
67. Moldoveanu, S. C.; David, V., Basic Information about HPLC. Elsevier: 2013; pp 1-51.
68. Abbott, S. R., Practical Aspects of Normal-Phase Chromatography. **1980**, *18* (10), 540-550.
69. Aguilar, M.-I., Reversed-Phase High-Performance Liquid Chromatography. Humana Press: pp 9-22.
70. King, D. T.; Stewart, J. T., HPLC Determination of Dacarbazine, Doxorubicin, and Ondansetron Mixture in 5% Dextrose Injection on Underivatized Silica with an Aqueous-Organic Mobile Phase. *Journal of Liquid Chromatography* **1993**, *16* (11), 2309-2323.
71. Hao, Z.; Xiao, B.; Weng, N., Impact of column temperature and mobile phase components on selectivity of hydrophilic interaction chromatography (HILIC). **2008**, *31* (9), 1449-1464.
72. Moldoveanu, S. C.; David, V., Retention Mechanisms in Different HPLC Types. Elsevier: 2013; pp 145-190.
73. Zuvela, P.; Skoczylas, M.; Jay Liu, J.; Ba Czek, T.; Kaliszan, R.; Wong, M. W.; Buszewski, B., Column Characterization and Selection Systems in Reversed-Phase High-Performance Liquid Chromatography. *Chem Rev* **2019**, *119* (6), 3674-3729.
74. Alpert, A. J., Hydrophilic-interaction chromatography for the separation of peptides, nucleic acids and other polar compounds. *Journal of Chromatography A* **1990**, *499*, 177-196.
75. Buszewski, B.; Noga, S., Hydrophilic interaction liquid chromatography (HILIC)--a powerful separation technique. *Analytical and bioanalytical chemistry* **2012**, *402* (1), 231-47.
76. McCalley, D. V., Study of the selectivity, retention mechanisms and performance of alternative silica-based stationary phases for separation of ionised solutes in hydrophilic interaction chromatography. *Journal of Chromatography A* **2010**, *1217* (20), 3408-3417.
77. Ibrahim, M. E. A.; Liu, Y.; Lucy, C. A., A simple graphical representation of selectivity in hydrophilic interaction liquid chromatography. *Journal of Chromatography A* **2012**, *1260*, 126-131.
78. Kaliszan, R., QSRR: Quantitative Structure-(Chromatographic) Retention Relationships. *Chemical Reviews* **2007**, *107* (7), 3212-3246.

79. Isokawa, M.; Kanamori, T.; Funatsu, T.; Tsunoda, M., Recent advances in hydrophilic interaction chromatography for quantitative analysis of endogenous and pharmaceutical compounds in plasma samples. *Bioanalysis* **2014**, 6 (18), 2421-2439.
80. Wang, C.; Jiang, C.; Armstrong, D. W., Considerations on HILIC and polar organic solvent-based separations: Use of cyclodextrin and macrocyclic glycopeptide stationary phases. *Journal of Separation Science* **2008**, 31 (11), 1980-1990.
81. Chen, J.; Wang, W.; Lv, S.; Yin, P.; Zhao, X.; Lu, X.; Zhang, F.; Xu, G., Metabonomics study of liver cancer based on ultra performance liquid chromatography coupled to mass spectrometry with HILIC and RPLC separations. *Analytica Chimica Acta* **2009**, 650 (1), 3-9.
82. Karlsson, H.; Larsson, J. M.; Thomsson, K. A.; Hard, I.; Backstrom, M.; Hansson, G. C., High-throughput and high-sensitivity nano-LC/MS and MS/MS for O-glycan profiling. *Methods Mol Biol* **2009**, 534, 117-31.
83. Anderson, N. L.; Anderson, N. G., The Human Plasma Proteome. *Molecular & Cellular Proteomics* **2002**, 1 (11), 845-867.
84. Xie, F.; Smith, R. D.; Shen, Y., Advanced proteomic liquid chromatography. **2012**, 1261, 78-90.
85. Shen, Y.; Zhang, R.; Moore, R. J.; Kim, J.; Metz, T. O.; Hixson, K. K.; Zhao, R.; Livesay, E. A.; Udseth, H. R.; Smith, R. D., Automated 20 kpsi RPLC-MS and MS/MS with chromatographic peak capacities of 1000-1500 and capabilities in proteomics and metabolomics. *Analytical Chemistry*, 77(10):3090-3100 **2005**, 77 (10).
86. Chervet, J. P.; Ursem, M.; Salzmann, J. P., Instrumental Requirements for Nanoscale Liquid Chromatography. *Analytical Chemistry* **1996**, 68 (9), 1507-1512.
87. Welch, C. J.; Wu, N.; Biba, M.; Hartman, R.; Brkovic, T.; Gong, X.; Helmy, R.; Schafer, W.; Cuff, J.; Pirzada, Z.; Zhou, L., Greening analytical chromatography. *TrAC Trends in Analytical Chemistry* **2010**, 29 (7), 667-680.
88. Kislik, V. S., *Solvent extraction classical and novel approaches*. 1st ed. ed.; Elsevier: Amsterdam, 2012.
89. Mitulovic, G.; Smoluch, M.; Chervet, J.-P.; Steinmacher, I.; Kungl, A.; Mechtler, K., An improved method for tracking and reducing the void volume in nano HPLC?MS with micro trapping columns. *Analytical and Bioanalytical Chemistry* **2003**, 376 (7), 946-951.
90. Houbart, V.; Cobraiville, G.; Lecomte, F.; Debrus, B.; Hubert, P.; Fillet, M., Development of a nano-liquid chromatography on chip tandem mass spectrometry method for high-sensitivity hepcidin quantitation. **2011**, 1218 (50), 9046-9054.



91. Percy, A. J.; Chambers, A. G.; Yang, J.; Domanski, D.; Borchers, C. H., Comparison of standard- and nano-flow liquid chromatography platforms for MRM-based quantitation of putative plasma biomarker proteins. *Anal Bioanal Chem* **2012**, *404* (4), 1089-101.
92. Levsen, K.; Wagner-Redeker, W.; Schäfer, K. H.; Dobberstein, P., On-line liquid chromatography-mass spectrometry analysis of non-ionic surfactants. **1985**, *323* (1), 135-141.
93. Bianchi, F.; Riboni, N.; Termopoli, V.; Mendez, L.; Medina, I.; Ilag, L.; Cappiello, A.; Careri, M., MS-Based Analytical Techniques: Advances in Spray-Based Methods and EI-LC-MS Applications. *Journal of Analytical Methods in Chemistry* **2018**, *2018*, 1-24.
94. Dole, M.; Cox, H. L.; Gieniec, J., Electrospray Mass Spectroscopy. In *Polymer Molecular Weight Methods*, AMERICAN CHEMICAL SOCIETY: 1973; Vol. 125, pp 73-84.
95. Kebarle, P.; Verkerk, U. H., Electrospray: From ions in solution to ions in the gas phase, what we know now. *Mass Spectrometry Reviews* **2009**, *28* (6), 898-917.
96. Chen, X.; Bichoutskaia, E.; Stace, A. J., Coulomb Fission in Dielectric Dication Clusters: Experiment and Theory on Steps That May Underpin the Electrospray Mechanism. **2013**, *117* (19), 3877-3886.
97. Megoulas, N. C.; Koupparis, M. A., Enhancement of evaporative light scattering detection in high-performance liquid chromatographic determination of neomycin based on highly volatile mobile phase, high-molecular-mass ion-pairing reagents and controlled peak shape. **2004**, *1057* (1-2), 125-131.
98. Nguyen, H. P.; Schug, K. A., The advantages of ESI-MS detection in conjunction with HILIC mode separations: Fundamentals and applications. **2008**, *31* (9), 1465-1480.
99. Gunnar, T.; Mykkanen, S.; Ariniemi, K.; Lillsunde, P., Validated semiquantitative/quantitative screening of 51 drugs in whole blood as silylated derivatives by gas chromatography-selected ion monitoring mass spectrometry and gas chromatography electron capture detection. **2004**, *806* (2), 205-219.
100. Annesley, T. M., Ion Suppression in Mass Spectrometry. *Clinical Chemistry* **2003**, *49* (7), 1041-1044.
101. Settineri, C. A.; Burlingame, A. L., Strategies for the Characterization of Carbohydrates from Glycoproteins by Mass Spectrometry. In *Techniques in Protein Chemistry*, Crabb, J. W., Ed. Academic Press: 1994; Vol. 5, pp 97-104.

## CHAPTER 2. MECHANISTIC ASPECTS OF HILIC SEPARATION OF GLYCANS AND GLYCOPROTEINS

### 2.1 Introduction

Glycosylation is a post- or co-translational modification involves an oligomeric carbohydrate moiety, known as a glycan, linked to the peptide backbone of a protein through covalent bonding to an asparagine, serine, or threonine residue<sup>1</sup>. Most human proteins exist in a glycosylated form, with estimates placing their occupancy of the human proteome at 50-70%<sup>2</sup>. It is theorized that all living organisms employ one or more glycoproteins<sup>3</sup>, which play a critical role in protein stability<sup>4</sup>, solubility<sup>5</sup>, cell signaling<sup>6</sup>, immunomodulation<sup>7</sup>, tumorigenesis<sup>8</sup>, and protein folding<sup>9</sup>. Glycans can act as a sort of fingerprint, with a variety of different carbohydrate groups incorporated into the typically-branched structure. Each of these carbohydrate groups alters the structure, and thus the function, of the glycoprotein<sup>10</sup>. Considering the prevalence and importance of protein glycosylation, it is only logical that there would be great interest in chromatographic separation of glycoproteins to assist in their identification and characterization.

From a purely analytical point of view, the simplest way to characterize a glycovariant is through analysis of the free glycan itself. In practice this is no simple task, as the process of isolating and derivatizing the glycan is laborious and involves multiple steps which lower the final sample yield. The time required to digest the glycoprotein, extract the glycan, and attach a 2-aminobenzamide (2-AB) fluorescent tag is on the order of two days. This would be an unacceptable lag time, for example if one needs to judge the purity of a monoclonal antibody drug during production. Further, essential analyte information can be lost in the process. Sialic acid, a glycan constituent that is implicated in malignant tumor development<sup>11, 12</sup>, can be lost or modified during the process of labelling or performing a tryptic digest to cleave the protein for glycopeptide analysis<sup>13</sup>. These drawbacks highlight the advantages that could be provided by a rapid, top-down method of glycoprotein profiling.

HPLC techniques for intact glycoprotein analysis are gaining in popularity, made possible in part through the advent of ultra-wide pore silica. While lectin-affinity<sup>14</sup>, HIC<sup>15</sup>, and ion-exchange methods<sup>16</sup> have been employed in glycoprotein separations, HILIC is generally considered a method-of-choice, as each carbohydrate group in a glycan adds a significant amount of hydrophilic character to the glycoprotein<sup>17</sup>. Polymeric and small-molecule based HILIC bonded

phases have been developed specifically for glycoprotein separation, and have demonstrated their efficacy through baseline separation of multiple glycovariants of model protein ribonuclease B (RNase B)<sup>18, 19</sup>. Despite these advances, the chromatographic resolution that can be attained in separation of intact glycoproteins simply does not compare to that which one can achieve when separating free glycans.

In this study, a commercial column developed specifically for glycoprotein separations was utilized to separate the 2-AB labelled free glycans from RNase B as well as the various glycoforms of the intact protein. The efficiency and selectivity for the two classes of analyte on the same column was assessed quantitatively to understand the sources of diminished resolution for the intact glycoprotein.

## **2.2 Experimental**

### **2.2.1 Chemicals**

Ultrapure water was generated using a Milli-Q water purification system. Acetonitrile and IPA were purchased from Thermo Fisher. All other reagents were purchased from Sigma.

### **2.2.2 Methods**

#### ***Glycan Sample Preparation***

Prior to labeling, glycans were cleaved from bovine pancreatic ribonuclease B (RNase B) using a modified version of the protocol described by Mann, et al<sup>20</sup>. For glycan cleavage, a solution was prepared containing 20 units PNGase F in 40  $\mu$ L of a 50 mM PBS solution at pH 7.2. This was combined with 360  $\mu$ L of a solution containing 400  $\mu$ g RNase B in 50 mM PBS (pH 7.2). This solution was incubated in a water bath at 37 °C for a total of 18 hours.

Residual PNGase F and deglycosylated RNase B were removed from this solution by utilizing an Amicon Ultra-0.5 mL spin filter with a 10 kDa molecular-weight cut-off cellulose membrane, spun using an Eppendorf MiniSpin microcentrifuge at 14,000 x g for 20 minutes. The concentrated protein solution that did not pass through the filter was set aside for later analysis to confirm successful deglycosylation.

HILICON iSPE-HILIC solid phase extraction (SPE) cartridges were employed to purify the glycan-containing filtrate in a process adapted from Zhang, et. al<sup>21</sup>. Cartridges were pre-

conditioned using 0.5 mL H<sub>2</sub>O and 1 mL ACN, each of which was added to the cartridge and immediately removed from the sorbent using aspiration. Next, a mixture of 33 µL of the filtrate and 133 µL ACN was loaded onto the SPE cartridge. After aspirating the solvent, the cartridge was then rinsed two times with 250 µL ACN with an aspiration step after each rinse. Glycans were then eluted from the cartridge using 45 µL of a 5% ACN solution containing 100 mM ammonium acetate, with pressure applied to the head of the cartridge to assist in eluate recovery. The elution step was performed a total of three times, after which 540 µL ACN was added to the centrifuge tube containing the purified glycan mixture, which was then placed into a -80 °C freezer for approximately one hour. After the glycan solution was completely frozen, it was uncapped and placed into a vacuum chamber for overnight lyophilization, in a process adapted from Merry, et. al<sup>22</sup>.

Glycans were labeled with a fluorescent dye, 2-aminobenzamide (2-AB) using a protocol originally developed by Bigge, et. al<sup>23</sup>, modified to increase the sample size. A mixture of 150 µL acetic acid and 350 µL DMSO was created, with 100 µL of this mixture added to 5 mg of dried 2-AB. The solution was mixed using vortexing for approximately one minute, until the dye was completely dissolved. Finally, 6 mg of the reducing agent sodium cyanoborohydride was added to the dye mixture, which was then sonicated for five minutes until there were no visible particulates. 15 µL of this dye mixture was then added to the centrifuge tube containing the dried glycan sample, which was tightly sealed and placed into a water bath for 3 hours at 65 °C.

After removing the solution from the water bath, a Waters Glycoworks HILIC 1cc SPE cartridge was used to purify the newly-labeled glycans following the protocol from the manufacturer<sup>24</sup>. Cartridges were preconditioned with 100 µL H<sub>2</sub>O, and 100 µL of 85/15 ACN/H<sub>2</sub>O, with aspiration performed immediately after loading each solvent. The ACN content of the sample was brought to 80%, and the sample was then loaded onto the cartridge followed by immediate aspiration. The cartridge was rinsed twice with 85/15 ACN/H<sub>2</sub>O and dried using vacuum aspiration. Finally, sample was eluted using 100 µL of a 100 mM ammonium acetate solution in 5% ACN. The eluate was recovered by applying pressure to the head of the cartridge with a syringe, and placed into a -20 °C freezer for approximately 30 minutes. The frozen glycan sample was then placed to a vacuum chamber for overnight lyophilization, and reconstituted in 30 µL of a solution containing 70% ACN.

## ***Chromatographic Methods***

The chromatograph utilized in this study was a Waters Acquity I-Class UHPLC instrument. An Acquity UHPLC Glycoprotein Amide column with dimensions of 10 cm x 2.1 mm containing 1.7  $\mu\text{m}$  particles with 300 Å pores was purchased from Waters and utilized for all chromatographic runs. Data were analyzed using OriginPro.

Prior to chromatographic analysis, glycoprotein samples were prepared in a 70% ACN diluent, containing 0.1% TFA to aid in solubility<sup>25</sup>. All runs were performed with the thermostatted column compartment held at 30 °C, and 0.1% TFA was used as the mobile phase additive. For gradient elution, the gradient steepness was the same for glycoprotein and glycan analytes. The gradient profile for the glycoproteins was 70 – 55% ACN over 45 minutes, and for the free glycans was 75 – 60% ACN over 45 minutes.

Isocratic runs used in generating the van Deemter plots used a mobile phase composition designed to give approximately the same retention factor for both analytes, with  $k_{\text{glycan}} = 4.4$  and  $k_{\text{glycoprotein}} = 4.1$  attained using 68% and 64.5% ACN for glycan and glycoprotein mobile phases, respectively. A partial loop injection method was used for all analyses in order to conserve sample, with 1  $\mu\text{L}$  injected from a 10  $\mu\text{L}$  sample loop.

## ***Molecular Modeling***

Molecular dynamics simulations were run using the GLYCAM06 force field<sup>26</sup> and GLYCAM-Web software<sup>27</sup> from the University of Georgia's Complex Carbohydrate Research Center. The resulting models were visualized using Python Molecular Viewer<sup>28</sup>.

## **2.3 Results and Discussion**

The higher HILIC resolution for free glycans compared to intact glycoproteins is illustrated in Figure 1. Using the same column and employing gradient elution with the same slope, the first two major peaks in the glycan sample are separated with nearly three-fold higher resolution than for the glycoprotein sample. It should be noted that the formula used for determining resolution in this case employed the peak FWHM (Equation 1) to lessen the impact from minority species eluting between the major peaks<sup>29</sup>.

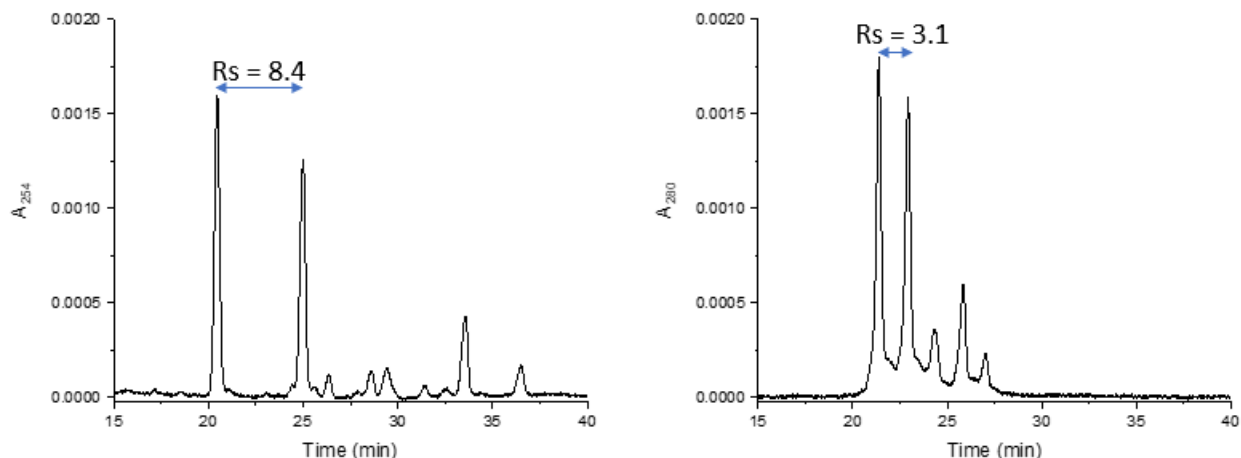


Figure 2.1. Chromatograms for the gradient elution of free glycans (left) and intact glycoproteins (right).

$$R = 1.18 \times \left( \frac{t_{R2} - t_{R1}}{FWHM_1 + FWHM_2} \right)$$

Equation 2.1

Figure 2.2 shows van Deemter plots obtained using isocratic of the glycans and the glycoproteins, with the efficiency calculated for the Mannose 5 peak. Those data were fit to the van Deemter equation, where the B term was found to be negligible in both cases. The C term is an order of magnitude lower for the free Mannose 5 glycan than for its glycoprotein counterpart, at  $1.4 \pm 0.1$  s and  $13.8 \pm 0.6$  s, respectively. This is attributed to slower intra-particle diffusion, as expected with a protein analyte<sup>30</sup>. The typical working range suggested by the column manufacturer<sup>31</sup> is highlighted in blue, showing the efficiency for the glycan is two to three times that with the intact protein under these conditions.

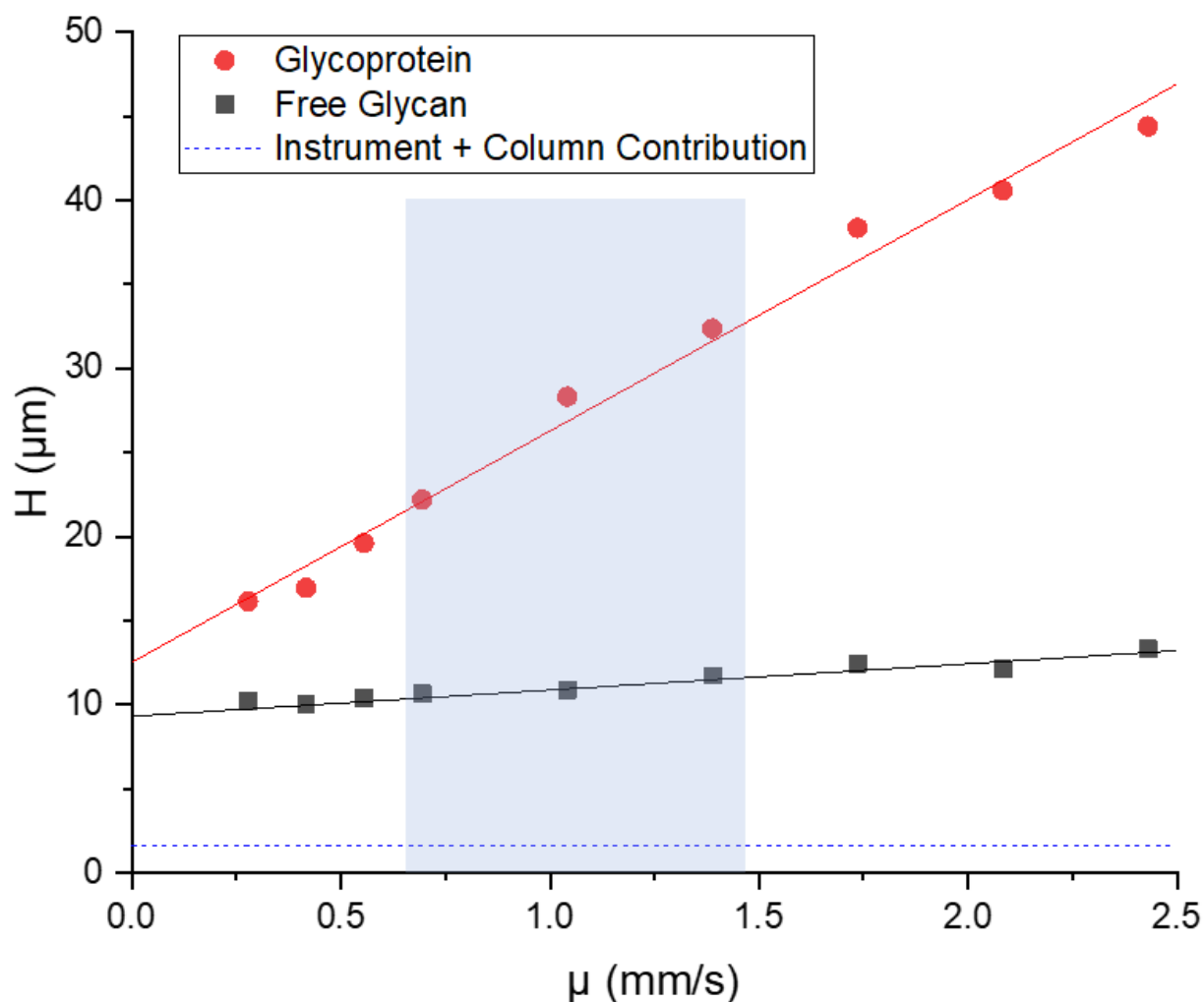


Figure 2.2. van Deemter plots for isocratic separations of the free Man5 glycan and the intact RNase B (+Man5) glycoprotein using detection at  $\lambda = 254$  nm and 280 nm, respectively. The shaded area indicates the typical working range, at 100 – 200  $\mu$ L/min

Although the difference in plate heights for the two samples is reduced with lower flowrates, the intercept is still significantly different for the glycan as compared to the protein ( $9.3 \pm 0.5$  and  $12.5 \pm 0.8$ , respectively). This appears to be caused by inhomogeneity of the protein itself, where overlapping peaks with slight retention shifts would artificially inflate the A-term in the van Deemter equation<sup>32</sup>. Various post-translational modifications can alter the hydrophilicity of the protein itself<sup>33</sup>, and a deconvoluted mass spectrum of the main peak over  $\pm 2\sigma$  reveals the presence of multiple co-eluting species (Figure 2.3). Viewing the extracted-ion chromatogram (EIC) for the most abundant species, the peak is 20% narrower than that of the UV chromatogram (Figure 2.4). The difference in the respective half-maximum peak widths for the EIC and UV

chromatograms, at 0.19 min, is enough to account for the difference in van Deemter A-terms: the intercept becomes  $8.8 \pm 0.6 \mu\text{m}$  when the difference is subtracted. The two van Deemter plots then have the same A-term, approximately  $9 \mu\text{m}$ , when the protein heterogeneity is accounted for. An independent measurement of the A term was made by injection of ribonuclease A under unretained conditions, and this was found to be only  $2 \mu\text{m}$ , which is much closer to what is expected for this Waters Acquity I-class UPLC with a  $0.5 \mu\text{m}$  detector volume. This is significantly smaller than the nominal  $9 \mu\text{m}$  intercept for both the Man5 glycoprotein and the Man5 glycan. The likely explanation is that the Man5 glycan moiety itself is heterogeneous, and evidence from tandem mass spectrometry supports this interpretation<sup>34</sup>.

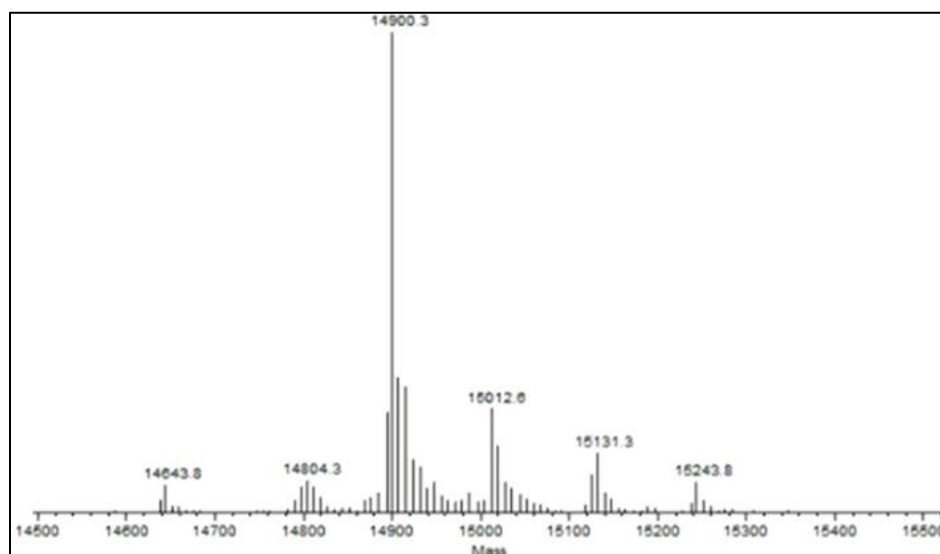


Figure 2.3. Deconvoluted mass spectrum for the purified RNase B (+Man5) glycoprotein



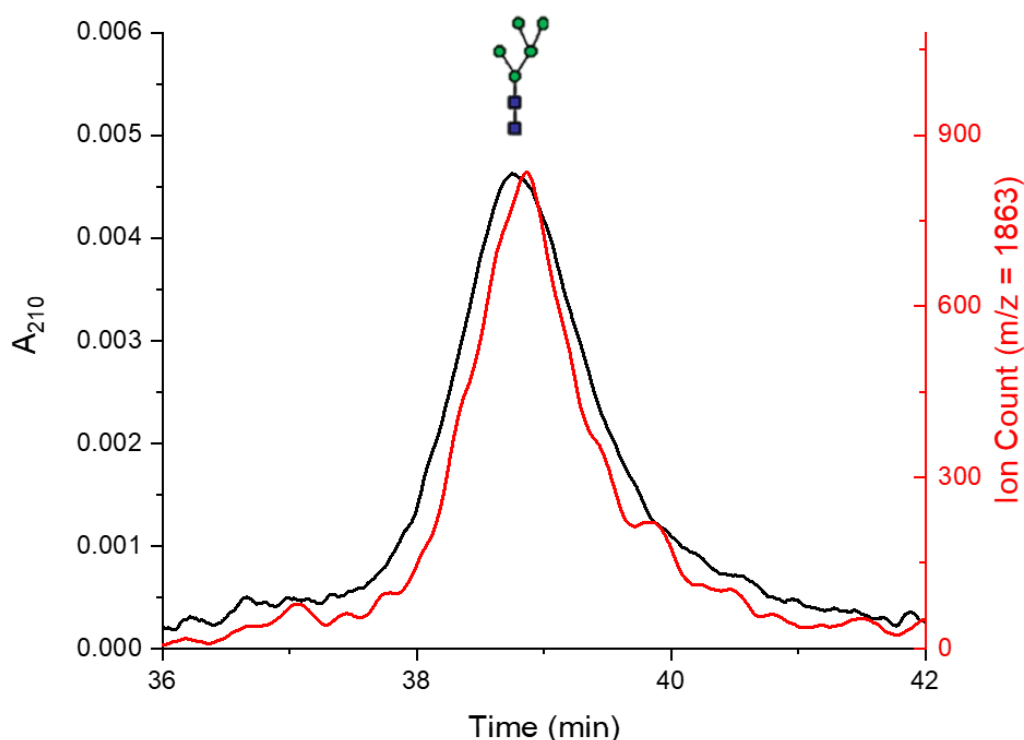


Figure 2.4. Chromatograms for a separation of the purified RNase B (+Man5) glycoprotein using UV absorbance (black) and mass spectrometry-based (red) detection methods

While there is a clear difference in column efficiency in separating the glycan and the intact protein, this is not the complete picture. The nearly-tripled resolution for the glycan is not explained by the doubled column efficiency, since resolution scales with the square root of efficiency. Therefore, it must be that the selectivity for the glycan species is correspondingly greater than that for the glycoproteins. To study selectivity, log-log scale plots of analyte retention factor versus volume fraction water were prepared for each of the glycans or glycoforms. These plots confirm the higher selectivity for the glycans: along the x-axis, which is relevant to gradient elution, there is a two-fold greater spacing between the traces for the free glycans than those for the intact glycoproteins (Figure 2.5). This means that the HILIC selectivity in gradient elution is inherently higher for separation of the free glycans: the increasing difference in  $k$  between the different species for a given mobile phase composition directly translates to increasing distance between the peaks in a chromatogram. A careful look at the linearity of the data points in Figure 5 reveals minor curvature, and such behavior has previously been attributed to silanol or solvent-solute interactions<sup>35, 36</sup>.

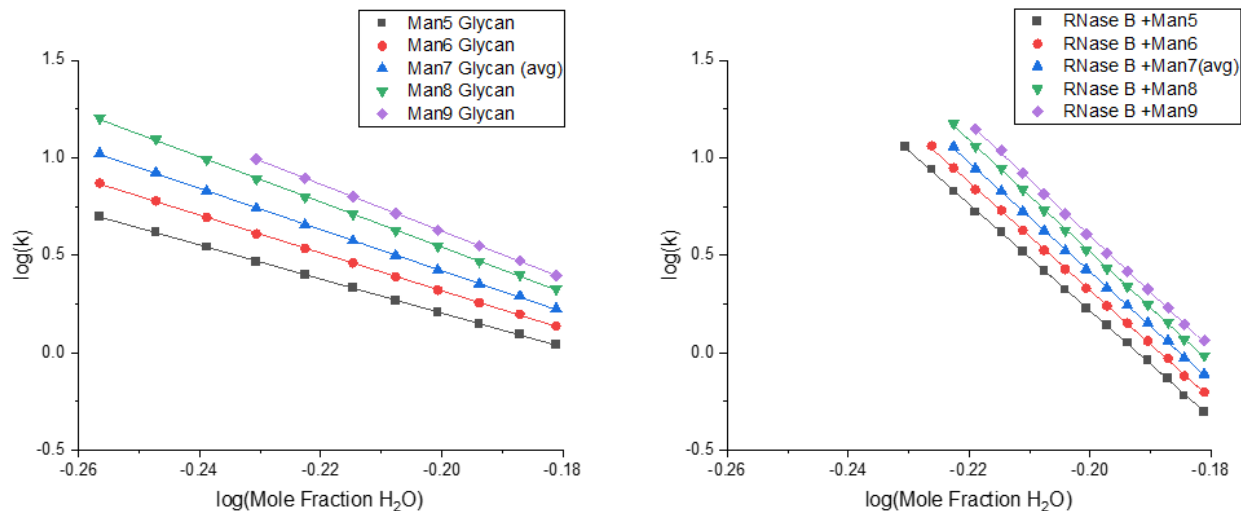


Figure 2.5. Log-log plots of retention factor as a function of mole fraction H<sub>2</sub>O for the free glycans of RNase B (left) and the intact glycovariants (right)

In 1974, Snyder presented an equation (Equation 2.2) describing a general relationship between retention factor,  $k$ , and the volume fraction of strong solvent,  $\phi$ <sup>35, 37</sup>. The slope of this equation,  $S'$ , is proportional to the number of solvent molecules that are displaced from a chromatographic surface by a solute upon adsorption. This model is useful in describing gradient elution separations because  $\phi$  is the quantity that is controlled experimentally. Soczewiński provided a model based on the law of mass action describing the number of displaced solvent molecules,  $m$ , displaced from the surface<sup>38</sup>. The resulting log-log equation (Equation 2.3) uses the mole fraction of strong solvent,  $X_s$ , rather than  $\phi$ , but it is more insightful to have an absolute number of solvent molecules rather than the proportionality<sup>39</sup>. The intercept is  $\log(k_0)$ , where  $k_0$  is the retention factor when the mole fraction of strong solvent (water in this case) is unity. Although Soczewiński based his model on normal-phase chromatography, its general application to HILIC has been confirmed<sup>36, 40</sup>.

$$\log(k) = \text{constant} + S'(\phi)$$

Equation 2.2.

$$\log(k) = \log(k_{\text{water}}) - m * \log(X_s)$$

Equation 2.3.

A linear fit was performed on the log-log plot of Figure 2.5 and the resulting slopes and intercepts are given in Table 2.1 and Table 2.2, respectively. The values of  $m$  are larger for the glycoproteins than for the glycans since the protein moiety also displaces water from the surface. It is the differences between  $m$  values that dictates selectivity. The data show that the differences in slope, rather than the intercepts,  $\log(k_0)$ , are the main source of spacings in the plots. The physical interpretation is that the HILIC separation relies upon each additional mannose group displacing an increasing amount of water from the surface upon adsorption. One can see from the Tables that the differences in values of  $m$  between the free glycans is significantly greater in magnitude than those of the intact glycoprotein. In other words, each additional mannose group on the glycoprotein displaces less water than does each mannose group on the glycan. This means that the protein must in some way shield the added sugar group from interaction with the stationary phase, causing the observed decrease in selectivity for the glycoforms of the intact protein.

It is noted that there are statistically significant differences in the intercepts among the glycans and that the trend in retention is opposite that for HILIC. This indicates that there would be a small amount of selectivity in reverse-phase mode, although the values of  $k$  would be impractically low,  $k < 0.1$ . The slight retention factors are likely due to the benzyl group of the label, with the progressively larger number of mannose groups decreasing retention, thereby explaining the reverse-phase retention order. It is interesting to note that the glycoproteins have much smaller intercepts and they are not statistically different. This is consistent with the previous interpretation: the intercepts are the same because the glycans are all attached to the same protein, and the intercepts are smaller because the protein is hydrophilic. The interpretation is consistent with previous literature that has described an analyte-specific balance of HILIC and RPLC-type separation mechanisms on HILIC chromatographic media<sup>36</sup>. The small values and small differences among intercepts in Table 2.2 underscore the main point of this study, which is that the slopes, i.e., the number of water molecules displaced upon analyte adsorption, give rise to HILIC selectivity.

Table 2.1. Values for  $m$ , the slope in Equation 2.3, for the RNase B glycovariants and free glycans

	<b>Man5</b>	<b>Man6</b>	<b>Man7 (avg)</b>	<b>Man8</b>	<b>Man9</b>
Intact Protein	27.4 $\pm 0.1$	27.8 $\pm 0.1$	28.0 $\pm 0.1$	28.7 $\pm 0.2$	28.9 $\pm 0.2$
Glycans	8.74 $\pm 0.04$	9.70 $\pm 0.04$	10.57 $\pm 0.04$	11.59 $\pm 0.04$	12.03 $\pm 0.04$

Table 2.2. Values for  $k_0$ , the intercept in Equation 2.3, for the RNase B glycovariants and free glycans

	<b>Man5</b>	<b>Man6</b>	<b>Man7 (avg)</b>	<b>Man8</b>	<b>Man9</b>
Intact Protein	-5.26 $\pm 0.02$	-5.23 $\pm 0.03$	-5.19 $\pm 0.01$	-5.22 $\pm 0.03$	-5.19 $\pm 0.04$
Glycans	-1.54 $\pm 0.01$	-1.62 $\pm 0.01$	-1.69 $\pm 0.01$	-1.78 $\pm 0.01$	-1.78 $\pm 0.01$

The crystallographic structure of RNase A, an aglycosylated variant of RNase B, is published on the RCSB Protein Data Bank<sup>41</sup>. This structure was glycosylated *in silico* and energy-minimized using the Glycam force field<sup>26</sup> to observe the orientation of the glycan in its free form or in the context of the larger protein (Figure 6). It appears that one of the branches of the protein-linked Man 6 glycan is not in a planar orientation with the side of the protein and base of the glycan, instead taking on a pyramidal geometry. The change towards a more three-dimensional glycan structure effectively decreases the cross-section of the glycan. This in turn reduces the area available for interaction with the stationary phase, thus offering a reasonable explanation for the decreasing number of water molecules displaced upon adsorption. These structures represent the physical conformation of molecules in H<sub>2</sub>O, rather than upon adsorption, therefore, one cannot extract quantitative information about the number of water molecules displaced. With more thorough molecular dynamics simulations the change in conformation upon adsorption may be

predicted, which may further assist in designing improved stationary phases for glycoprotein separations.

## 2.4 Conclusion

Combining the effects of protein heterogeneity and diminished selectivity for the intact glycoprotein paints a more complete picture of the difficulty one encounters when moving from a small molecule to protein analytical modality. An additional aspect that plays a role in diminishing the efficacy of protein separations is the physical structure of the stationary phase. The same wide-pore column was used in this work for both classes of analyte, as a control. Using silica with smaller pores can increase the surface area, with the potential for a corresponding increase in efficiency, but these pores will generally exclude larger molecules such as proteins. As glycans are approximately an order of magnitude less massive than proteins, they can be expected to present a significantly diminished cross-section which would allow use of a more efficient, smaller-pore column.

It is important to keep in mind that with HILIC stationary phases, the water layer presents a more three-dimensional bonded phase than one would expect to encounter in a traditional RPLC column. Increasing the thickness of this water layer may provide an avenue for more of the protein-linked glycan to interact with the stationary phase, which has been investigated and will be discussed more thoroughly in the next chapter.

With an improved bonded phase and use of MS-based detection, it is conceivable that the resolution for separation of intact glycoproteins could approach that observed with the free glycans. This will only be possible at lower flowrates, however, as the fundamental physical processes which dictate mass transfer rates remain unchanged. Using smaller, non-porous particles should assist in this area due to the lower C-term that they present, which will also be discussed later in this dissertation.

## 2.5 References

1. Lis, H.; Sharon, N., Protein glycosylation: structural and functional aspects. *European Journal of Biochemistry* **1993**, 218 (1), 1-27.

2. Apweiler, R., On the frequency of protein glycosylation, as deduced from analysis of the SWISS-PROT database. *Biochimica et Biophysica Acta (BBA) - General Subjects* **1999**, 1473 (1), 4-8.
3. Shylaja, M.; Seshadri, H., Glycoproteins: An overview. *Biochemical Education* **1989**, 17 (4), 170-178.
4. Mimura, Y.; Church, S.; Ghirlando, R.; Ashton, P.; Dong, S.; Goodall, M.; Lund, J.; Jefferis, R., The influence of glycosylation on the thermal stability and effector function expression of human IgG1-Fc: properties of a series of truncated glycoforms. *Molecular immunology* **2000**, 37 (12-13), 697-706.
5. Tams, J. W.; Vind, J.; Welinder, K. G., Adapting protein solubility by glycosylation. *Biochimica et Biophysica Acta (BBA) - Protein Structure and Molecular Enzymology* **1999**, 1432 (2), 214-221.
6. Zhao, Y.-Y.; Takahashi, M.; Gu, J.-G.; Miyoshi, E.; Matsumoto, A.; Kitazume, S.; Taniguchi, N., Functional roles of N-glycans in cell signaling and cell adhesion in cancer. **2008**, 99 (7), 1304-1310.
7. Atochina, O.; Da'Dara, A. A.; Walker, M.; Harn, D. A., The immunomodulatory glycan LNFPIII initiates alternative activation of murine macrophages in vivo. *Immunology* **2008**, 125 (1), 111-121.
8. Hughes, R. C., MEMBRANE GLYCOPROTEINS AND GROWTH CONTROL. Elsevier: 1976; pp 269-284.
9. Molinari, M., N-glycan structure dictates extension of protein folding or onset of disposal. **2007**, 3 (6), 313-320.
10. Morell, A. G.; Gregoriadis, G.; Scheinberg, I. H.; Hickman, J.; Ashwell, G., The role of sialic acid in determining the survival of glycoproteins in the circulation. *Journal of Biological Chemistry* **1971**, 246 (5), 1461-1467.
11. van Beek, W. P.; Smets, L. A.; Emmelot, P., Increased Sialic Acid Density in Surface Glycoprotein of Transformed and Malignant Cells—a General Phenomenon? *Cancer Research* **1973**, 33 (11), 2913-2922.
12. Stefenelli, N.; Klotz, H.; Engel, A.; Bauer, P., Serum sialic acid in malignant tumors, bacterial infections, and chronic liver diseases. **1985**, 109 (1), 55-59.
13. Yang, S.; Zhang, L.; Thomas, S.; Hu, Y.; Li, S.; Cipollo, J.; Zhang, H., Modification of Sialic Acids on Solid Phase: Accurate Characterization of Protein Sialylation. *Analytical Chemistry* **2017**, 89 (12), 6330-6335.
14. Lotan, R.; Nicolson, G. L., Purification of cell membrane glycoproteins by lectin affinity chromatography. *Biochimica et Biophysica Acta (BBA) - Reviews on Biomembranes* **1979**, 559 (4), 329-376.

15. Rustandi, R. R., Hydrophobic Interaction Chromatography to Analyze Glycoproteins. Humana Press: 2013; pp 211-219.
16. Raouf, A.; Parker, N.; Iddon, D.; Ryder, S.; Langdon-Brown, B.; Milton, J. D.; Walker, R.; Rhodes, J. M., Ion exchange chromatography of purified colonic mucus glycoproteins in inflammatory bowel disease: absence of a selective subclass defect. *Gut* **1991**, 32 (10), 1139-1145.
17. Periat, A.; Krull, I. S.; Guilleme, D., Applications of hydrophilic interaction chromatography to amino acids, peptides, and proteins. **2015**, 38 (3), 357-367.
18. Zhang, Z.; Wu, Z.; Wirth, M. J., Polyacrylamide brush layer for Hydrophilic Interaction Liquid Chromatography of intact glycoproteins. *J Chromatogr A* **2013**, 1301, 156-61.
19. Matthew A. Lauber, S. A. M., Bonnie A. Alden, Pamela C. Iraneta, and Stephan M. Koza. Developing High Resolution HILIC Separations of Intact Glycosylated Proteins Using a Wide-Pore Amide-Bonded Stationary Phase 2015.
20. Mann, A. C.; Self, C. H.; Turner, G. A., A general method for the complete deglycosylation of a wide variety of serum glycoproteins using peptide-N-glycosidase-F. **1994**, 1 (4), 253-261.
21. Zhang, Q.; Li, H.; Feng, X.; Liu, B.-F.; Liu, X., Purification of Derivatized Oligosaccharides by Solid Phase Extraction for Glycomic Analysis. **2014**, 9 (4), e94232.
22. Merry, A. H.; Neville, D. C. A.; Royle, L.; Matthews, B.; Harvey, D. J.; Dwek, R. A.; Rudd, P. M., Recovery of Intact 2-Aminobenzamide-Labeled O-Glycans Released from Glycoproteins by Hydrazinolysis. **2002**, 304 (1), 91-99.
23. Bigge, J. C.; Patel, T. P.; Bruce, J. A.; Goulding, P. N.; Charles, S. M.; Parekh, R. B., Nonselective and Efficient Fluorescent Labeling of Glycans Using 2-Amino Benzamide and Anthranilic Acid. *Analytical Biochemistry* **1995**, 230 (2), 229-238.
24. Lauber, M. A.; Koza, S. M.; Fountain, K. J., GlycoWorks HILIC SPE Robust Glycan Sample Preparation. Waters: 2014; pp 1-3.
25. Houen, G., The solubility of proteins in organic solvents. *Acta Chem Scand* **1996**, 50 (1), 68-70.
26. Kirschner, K. N.; Yongye, A. B.; Tschampel, S. M.; González-Outeiriño, J.; Daniels, C. R.; Foley, B. L.; Woods, R. J., GLYCAM06: A generalizable biomolecular force field. Carbohydrates. *Journal of Computational Chemistry* **2008**, 29 (4), 622-655.
27. WoodsGroup GLYCAM Web. Complex Carbohydrate Research Center, University of Georgia, Athens, GA. <http://glycam.org> (accessed March 30, 2020).
28. Sanner, M. F., Python: a programming language for software integration and development. *J Mol Graph Model* **1999**, 17 (1), 57-61.

29. Kawabe, T.; Tomitsuka, T.; Kajiro, T.; Kishi, N.; Toyo'Oka, T., Ternary isocratic mobile phase optimization utilizing resolution Design Space based on retention time and peak width modeling. **2013**, *1273*, 95-104.
30. Gritti, F.; Guiochon, G., Mass transfer equation for proteins in very high-pressure liquid chromatography. *Analytical chemistry* **2009**, *81* (7), 2723-2736.
31. Koza, S. M.; Lauber, M. A.; Fountain, K. J.; McCall, S.; Bharadjwaj, R.; Fournier, J.; Chambers, E. E.; Morris, M. F.; Brousmiche, D. W.; Iraneta, P. C.; McCarthy, S. M.; Birdsall, R. E.; Yu, Y. Q., Glycans - Waters Application Notes. Waters Corporation: 2016.
32. Bupp, C. R.; Wirth, M. J., Making Sharper Peaks for Reverse-Phase Liquid Chromatography of Proteins. *Annual Review of Analytical Chemistry* **2020**, *13* (1).
33. Knorre, D. G.; Kudryashova, N. V.; Godovikova, T. S., Chemical and functional aspects of posttranslational modification of proteins. *Acta Naturae* **2009**, *1* (3), 29-51.
34. Prien, J. M.; Ashline, D. J.; Lapadula, A. J.; Zhang, H.; Reinhold, V. N., The high mannose glycans from bovine ribonuclease B isomer characterization by ion trap MS. *Journal of the American Society for Mass Spectrometry* **2009**, *20* (4), 539-56.
35. Valkó, K.; Snyder, L. R.; Glajch, J. L., Retention in reversed-phase liquid chromatography as a function of mobile-phase composition. **1993**, *656* (1-2), 501-520.
36. Jin, G.; Guo, Z.; Zhang, F.; Xue, X.; Jin, Y.; Liang, X., Study on the retention equation in hydrophilic interaction liquid chromatography. **2008**, *76* (3), 522-527.
37. Snyder, L. R., Role of the Solvent in Liquid-Solid Chromatography—A Review. *Analytical Chemistry* **1974**, *46* (11), 1384-1393.
38. Soczewinski, E.; Waksmundzki, A.; Soczewinski, E.; Suprynowicz, Z.; Ewell, R. H.; Harrison, J. M.; Berg, L.; Pimentel, G. C.; McClellan, A. L.; Hydrogen Bond, T.; Francisco, S., Solvent Composition Effects in Thin-Layer Chromatography Systems of the Type Silica Gel-Electron Donor Solvent. *J. Oscik, Bull. Acad. Pol. Sci., Ser. Sci. Chim* **1968**, *5* (1), 7-7.
39. Soczewiński, E., Mechanistic molecular model of liquid–solid chromatography. **2002**, *965* (1-2), 109-116.
40. Wang, P. G.; He, W., *Hydrophilic interaction liquid chromatography (HILIC) and advanced applications*. Taylor & Francis: Boca Raton, 2011.
41. Chatani, E.; Hayashi, R.; Moriyama, H.; Ueki, T., Conformational strictness required for maximum activity and stability of bovine pancreatic ribonuclease A as revealed by crystallographic study of three Phe120 mutants at 1.4 Å resolution. **2009**, *11* (1), 72-81.



## **CHAPTER 3. DEVELOPING A NANO-HILIC PLATFORM FOR SEPARATION OF LABELED GLYCOPROTEINS WITH FLUORESCENCE DETECTION**

### **3.1 Introduction**

The work discussed in the previous chapter made the case for an improved bonded phase that might allow the entire glycan to interact with the water layer on the particle surface, even when the glycans remains attached to the protein. Polymer brush layer bonded phases have been investigated by our research group for several years<sup>1-3</sup>, and seemed a clear choice for this purpose. Two candidates were selected for this study: polyacrylamide (PAAm) and polyhydroxymethacrylamide (PHMAAm). Both polymers are based upon hydrophilic monomers, and are known to swell upon hydration, incorporating a substantial amount of water within and surrounding the polymer<sup>1, 4, 5</sup>.

Utilizing Snyder plots we are able to quantitatively assess both analyte selectivity, by looking at the spacing between the trendlines, and the degree of interaction between the analyte and the surface-immobilized water layer, by looking at the trendline slopes. This provides a broader view when optimizing bonded phase design. Instead of comparing the analyte selectivity provided by columns under specific conditions and assuming those conditions are truly representative of column performance, a mechanistic approach can be taken to predict performance across a broad range of conditions.

Moving this to the nano-scale has great potential in improving analytical sensitivity<sup>6</sup>, however it is critical to minimize extra-column broadening when developing such a platform. Fluorescence microscopy is an ideal method of detection as it enables the researcher to observe chromatographic performance in real time with excellent sensitivity<sup>7</sup> without the potential for post-column broadening which can significantly hamper chromatographic performance<sup>8</sup>. Nano-scale LC is particularly sensitive to this issue<sup>9, 10</sup>, making this consideration an important part of platform development.

Using fluorescence microscopy-based detection is not without its drawbacks, however. Most proteins do not exhibit a significant degree of fluorescence, and as such must be labeled prior to analysis<sup>11</sup>. The addition of a dye label can introduce structural changes in the protein analyte<sup>12</sup>, which may in turn influence retention time<sup>13</sup>. The possibility of a multiply-labeled protein<sup>14</sup>

increases the likelihood of peak splitting, which can result in the misidentification of peaks. Further, this process can be time consuming and resource intensive<sup>11</sup>, making it impractical for use as a standard method. For this reason, the work presented in this chapter can best be considered a “stepping stone” on the path to a more robust method.

## **3.2 Experimental**

### **3.2.1 Materials**

Ultrapure water was generated using a Millipore Milli-Q water filtration system. Formic acid, acetonitrile, isopropanol, toluene, ethanol, aluminum oxide and the Alexa Fluor 488 Protein Labeling Kit were purchased from Thermo Fisher. Sodium ascorbate was obtained from TCI. Silica gel was purchased from Sorbtech. Organosilanes were purchased from Gelest. Me<sub>6</sub>Tren was obtained from Alfa Aesar. All other reagents were purchased from Sigma.

Toluene was dried prior to use by flowing it through a 5 cm ID glass column filled with approximately 5 cm aluminum oxide, followed by approximately 30 cm silica gel, and a glass wool frit. A Whatman paper filter was used to prevent silica gel from entering the bottle used to collect the dry toluene.

The fluorescence microscopy apparatus consisted of a Nikon Eclipse TE2000-LI inverted microscope with a Princeton Instruments ProEM 512SSD CCD detector. A fluorescence filter set (XF202) was purchased from Omega Optics, consisting of bandpass excitation and emission filters, and a dichroic mirror. Fluorescence data were captured using Princeton Instruments WinView software. Data were analyzed using Microsoft Excel and OriginLabs OriginPro software.

Optical microscope images were acquired using a Nikon SMZ1500 microscope coupled to a Nikon DS-Fi1 detector. These images were captured using NIS-Elements software.

TEM micrographs were acquired a FEI Technai F20 instrument and analyzed using Gwyddion imaging software. The chromatograph used for UHPLC separations was a Waters Acquity I-Class UHPLC instrument. The nanoLC instrument employed was a Thermo Fisher UltiMate 3000.

Heat treatment steps were performed using an OTF-1200X tube furnace from MTI corporation. Particles were sonicated using a Branson 3800 Ultrasonic Cleaner. All lab-made columns were packed using a Chromtech CP-class isocratic pump.

Stainless-steel column hardware including column bodies, nuts, and 0.5  $\mu\text{m}$ -mesh frits were purchased from IDEX. Polymicro fused silica capillary tubing with a 360  $\mu\text{m}$  outer and 75  $\mu\text{m}$  inner diameter was purchased from Molex. Capillary fittings and capillary packing frits were purchased from VICI. The Fisherbrand hygrometer was purchased from Fisher Scientific.

### **3.2.2 Methods**

#### ***Sample Preparation***

Prior to analysis, the protein sample was labelled with a small molecule fluorophore. Alexa Fluor 488 was used for this purpose, chosen based on its resistance to photobleaching and high quantum yield<sup>14</sup>.

The labeling protocol was adapted from the manufacturer's recommendations<sup>15</sup>, with the exception that the amount of protein used was 20x the amount recommended (20 mg/mL RNase B instead of 1 mg/mL.) This change was introduced to minimize fluorescence quenching and to reduce sample heterogeneity caused by different degrees of labeling, which will be discussed in more detail later in this chapter. A diagram of the labeling process is given in Figure 3.1.

After labeling, the sample was diluted to 40  $\mu\text{g/mL}$  using 80% ACN, 10% DMSO, 0.1% FA, and 0.025% TFA unless otherwise noted. This was accomplished by creating the final diluent mixture first, then adding the labeled protein mixture in one step (in order to minimize the risk of precipitation that may occur when adding 100% ACN to the labeled protein mixture before further dilution.)

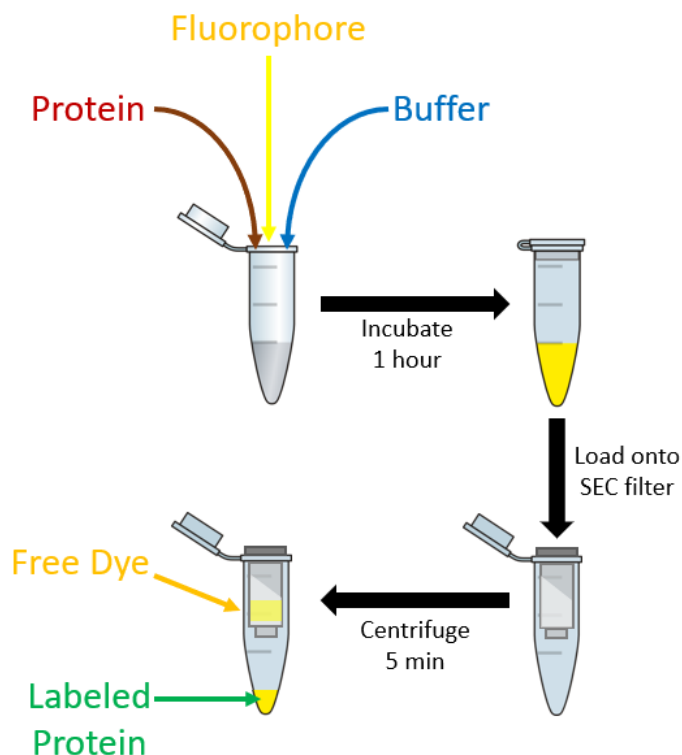


Figure 3.1. Workflow for Labeling Protein with Small-molecule Fluorophore

### ***Particle Preparation***

Particles were heat-treated prior to chemical modification. The first heat-treatment procedure, calcination, was utilized in order to remove any organic impurities and promote formation of siloxane bonds<sup>16</sup>. This was achieved by heating the particles to 600 °C for six hours, followed by sonication in ethanol and three sequential rinses with ultrapure water. This process was repeated a total of three times. The particles were next annealed at 1050 °C for three hours to smooth the surface, followed by sonication in ethanol and triple rinsing with ultrapure water.

After heat-treatment, the particles underwent a rehydroxylation step. This was performed by refluxing in 1 M nitric acid for 24 hours while stirring, followed by six rinses in ultrapure water. Particles were then stored in ultrapure water until they were ready for silylation.

Particles that were to be packed into a stainless-steel column for UHPLC analysis were silylated, where a monolayer composed of (chloromethyl)phenylethyl-dimethylsilane (mBC) and trimethylsilane (mC1) moieties was synthesized on the particle surface. For this reaction, 2 grams of particles were sonicated in 96 mL dry toluene in a round-bottom flask until they were fully suspended. The headspace was purged with nitrogen, and the flask was connected to a condenser

and placed into a sand bath on a heated stir-plate. The temperature of the stir plate was increased to 350 °C and stirring continued for 15 minutes, before adding 2 mL of mBC and 100 µL butylamine. The particles were refluxed for 3 hours before 2 mL mC1 was added, followed by another 3 hours of refluxing.

After the reaction mixture cooled to room temperature, the particles were centrifuged and decanted. They were next rinsed three times with toluene, and again with ethanol. Particles were subsequently dried using a vacuum chamber and stored dry until needed.

### *Ex-situ Polymer Modification*

Some of the particles that were to be packed into a stainless-steel UHPC column were subjected to ex-situ polymer modification. These particles were coated with polyhydroxymethacrylamide (PHMAAm) using an AGET-ATRP synthesis<sup>17</sup> which relied upon the mBC initiator for surface-induced polymerization, in the reaction scheme provided in Figure 3.2. In this reaction, X represents the chloride group for the mBC initiator,  $L_n$  is the  $Me_6Tren$  ligand, M represents the monomer, and  $P_n\bullet$  represents the polymer radical.

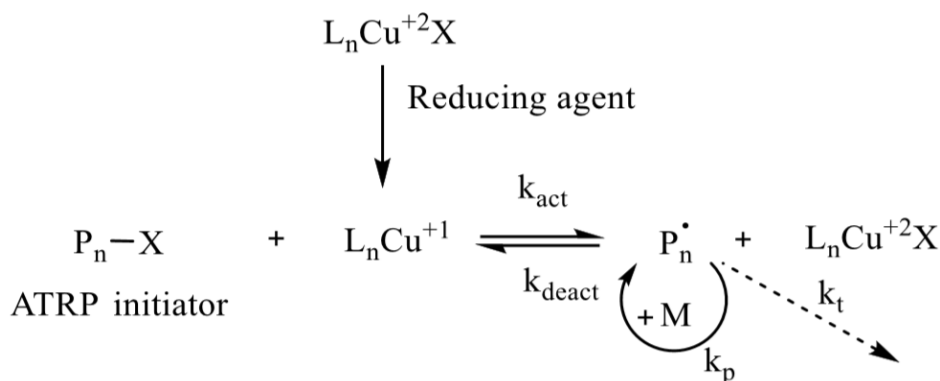


Figure 3.2. AGET-ATRP Reaction Scheme

The process for PHMAAm coating is as follows: first, bottles of  $H_2O$  and EtOH were sparged using nitrogen for approximately one hour. Next, 0.45 grams of the mBC:mC1 coated particles were suspended in a round-bottom flask containing 15 mL EtOH, using sonication for 5 minutes. 13.3 mL  $H_2O$  was added to this flask and the headspace was purged with nitrogen. 13.3

mL of liquid N-hydroxymethacrylamide monomer (48% in H<sub>2</sub>O) was then added to the flask, which was allowed to sonicate for another 5 minutes. A magnetic stir bar was added to the flask, which was then immersed in a 38 °C water bath with a stir plate underneath providing constant stirring for the duration of the reaction.

Two additional reaction mixtures were prepared. The first mixture contained 40 mg copper (II) chloride and 80 µL Me<sub>6</sub>Tren in 2.5 mL H<sub>2</sub>O. The next mixture contained 20 mg sodium ascorbate in 2.5 mL H<sub>2</sub>O. These reaction mixtures were briefly vortexed, then sonicated for approximately 10 minutes, until the copper was completely dissolved. Next, the copper (II) chloride and sodium ascorbate reaction mixtures were combined in a glass vial and mixed using inversion. They were then sonicated for one additional minute.

The particle-containing flask was again sparged with nitrogen for two minutes. The vial containing the other reaction mixtures was added, and a septum with a nitrogen-filled balloon was placed onto the flask. The reaction was then allowed to proceed for 90 minutes.

After the polymerization reaction was complete, the particles were transferred to conical flasks, centrifuged and decanted. Particles were then rinsed three times with H<sub>2</sub>O, once with ethylene glycol, twice with H<sub>2</sub>O, once with EtOH, and one final time with acetone, with two minutes sonication in between each rinse with the exception of the ethylene glycol rinse wherein the slurry was sonicated for 20 minutes. Centrifugation after each rinse was performed for 2 minutes at 7000 RPM with the exception of the ethylene glycol rinse, which was performed for 10 minutes at 4500 RPM. After the rinses, the particles were dried in a vacuum chamber and set aside until packing. TEM micrographs of particles before and after ex-situ polymer modification are provided in Figure 3.3.

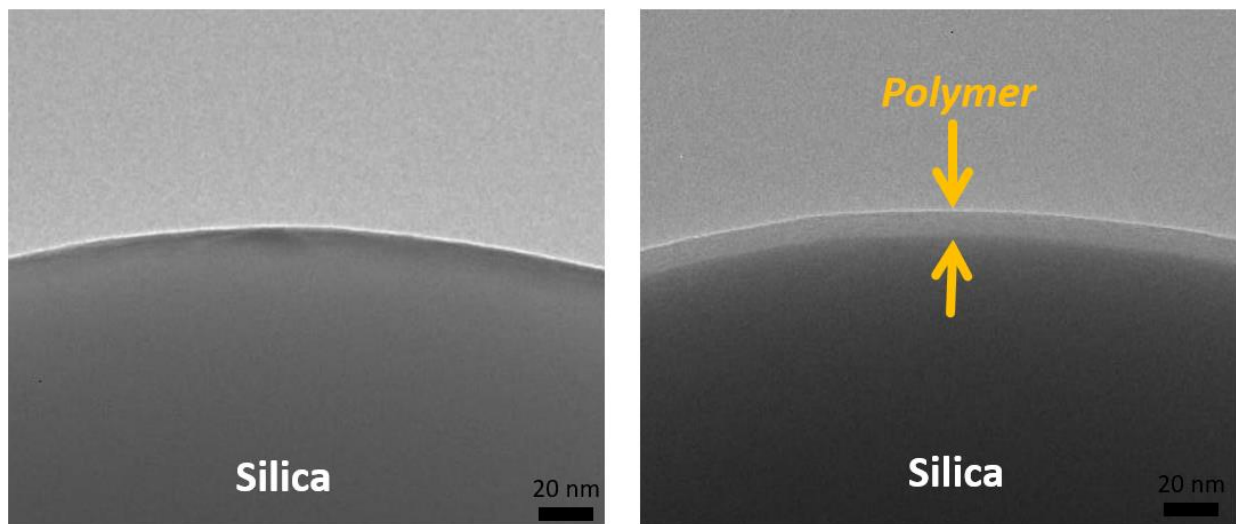


Figure 3.3. TEM Micrograph of particles before and after adding a polymer brush layer using surface-initiated polymerization

### ***Column Packing***

Particles were packed into 5 cm x 2.1 mm stainless-steel columns under sonication, as illustrated in Figure 3.4. A slurry was created using 0.26 g of particles in 2 mL solvent. PHMAAm-coated particles were suspended under sonication in a mixture of 50/50 H<sub>2</sub>O/EtOH prior to packing, and mBC:mC1 particles were suspended under sonication in 100% EtOH. For the columns containing ex-situ modified, PHMAAm-coated particles, the packing solvent was 60/40 EtOH/H<sub>2</sub>O. The mBC:mC1 particles required 100% EtOH as a packing solvent.

A 20 cm x 4.6 mm reservoir column was attached to an empty, fritted column body using a custom-made packing union. A photograph of the packing setup is provided in Figure 3.4 for clarity, and the CAD design for the packing union is provided in Figure 3.5. Columns were packed at 17.5 kPSI for 30 minutes under sonication, for an additional 5 minutes without sonication, then allowed to depressurize completely. This process was repeated two additional times. With the PHMAAm-coated particles, the third packing step was performed using 80/20 ACN/H<sub>2</sub>O as the packing solvent. After packing, the reservoir column was removed, a fritted nut was screwed onto the other end of the column, and a torque wrench was used to tighten the nut to 9.25 lb/ft.

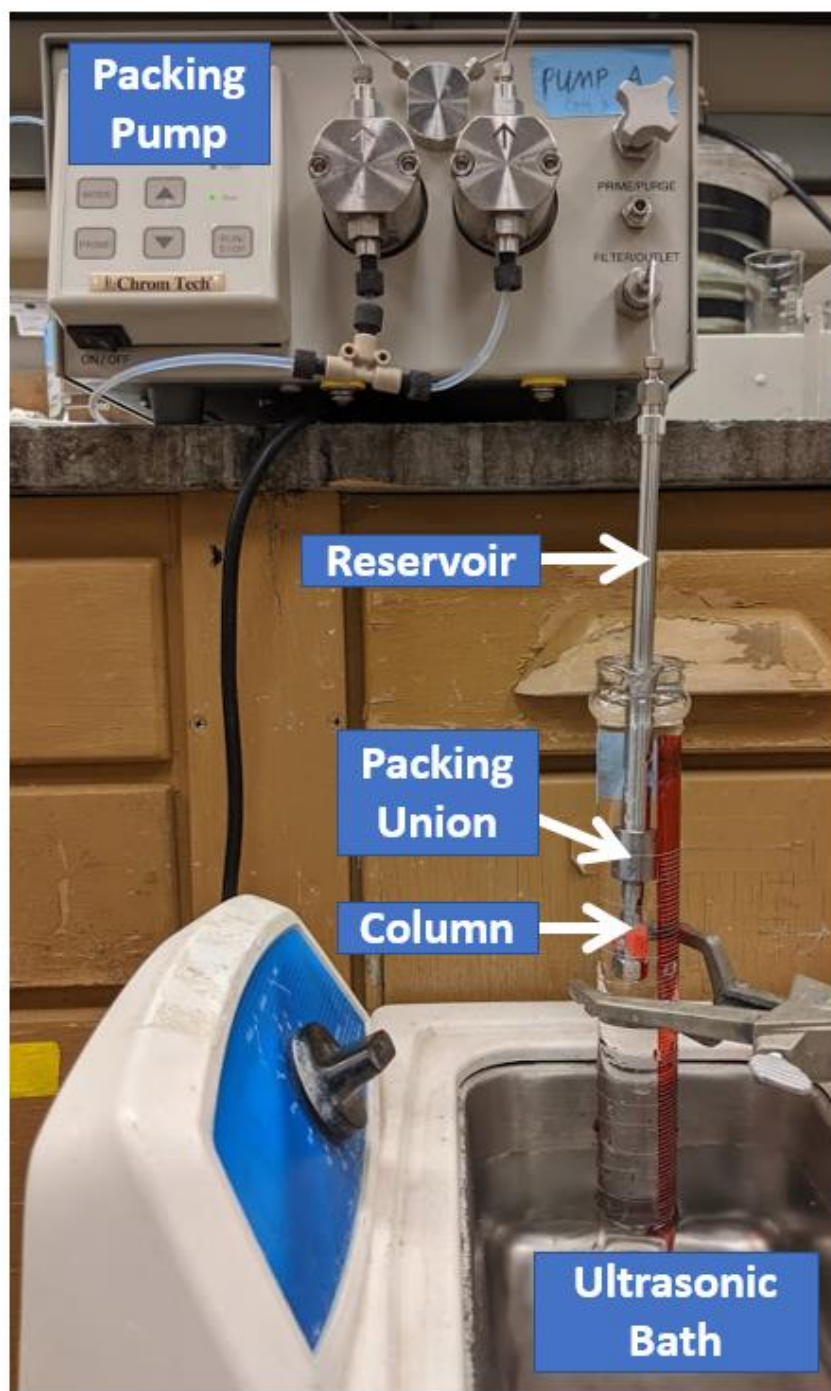


Figure 3.4. Stainless-steel Column Packing Setup



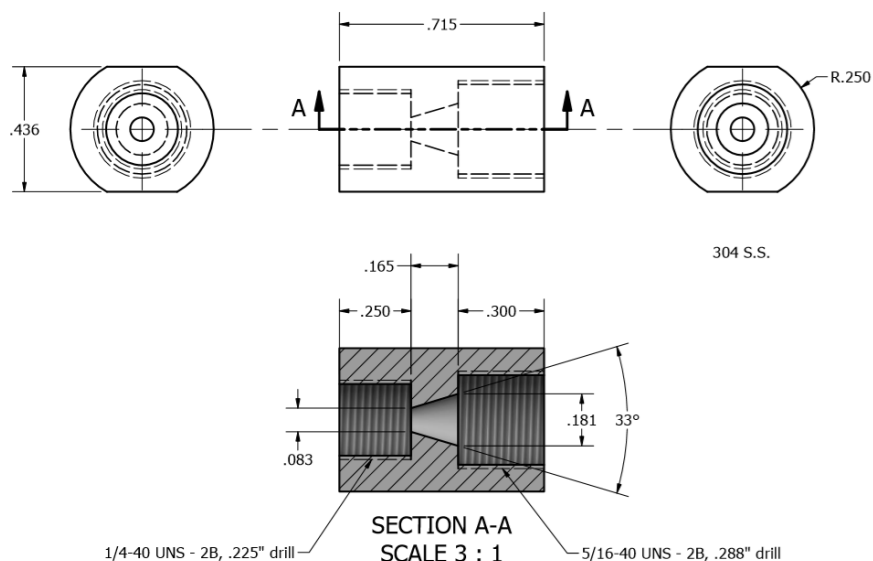


Figure 3.5. CAD drawing of custom-made column packing union

### ***In-column Polymer Modification for Stainless-Steel Columns***

After packing the mBC:mC1-modified silica particles into stainless steel columns, three reaction mixtures were prepared for an AGET-ATRP reaction. This synthesis method was employed as described in the earlier section describing *ex-situ* polymer growth, albeit with conditions modified optimized for stable growth of a PAAm brush layer instead of PHMAAm.

Similar to earlier, the solvents were first sparged with nitrogen in order to remove dissolved oxygen. The first reaction mixture consisted of 0.88 g acrylamide in 4 mL of 3:1 H<sub>2</sub>O:IPA. This was prepared in a polypropylene centrifuge tube. Next, a mixture was created containing 40 mg CuCl<sub>2</sub>, 80  $\mu$ L Me<sub>6</sub>Tren and 2.5 mL of 3:1 H<sub>2</sub>O:IPA in a glass vial. Finally, a solution of 20 mg sodium ascorbate in 2.5 mL of 3:1 H<sub>2</sub>O:IPA was prepared, also in a glass vial.

Each reaction mixture was mixed by inversion and sonicated for approximately 10 minutes, until the copper in the second reaction mixture was completely dissolved. After this, 516  $\mu$ L was taken from the second vial and placed into a new vial along with 500  $\mu$ L of the sodium ascorbate solution. This mixture was sonicated for approximately two minutes, then added to the acrylamide solution in the polypropylene centrifuge tube. The final mixture was then sonicated for approximately two minutes before being added to a 25 cm x 4.6 mm reservoir column, which was connected to the mBC:mC1 particle-packed column using stainless-steel tubing.

The reaction mixture was pumped through the packed column at 100  $\mu\text{L}/\text{min}$  for 10 minutes using 3:1  $\text{H}_2\text{O}:\text{IPA}$  as the pumping solvent. Flow was then stopped and the column was capped at the outlet. After 60 minutes, the column was disconnected from the reservoir, connected directly to the pump, and rinsed for 60 minutes at 100  $\mu\text{L}/\text{min}$  using 3:1  $\text{H}_2\text{O}:\text{IPA}$ . A TEM micrograph of PAAm-coated particles after an in-column modification is provided in Figure 3.6.

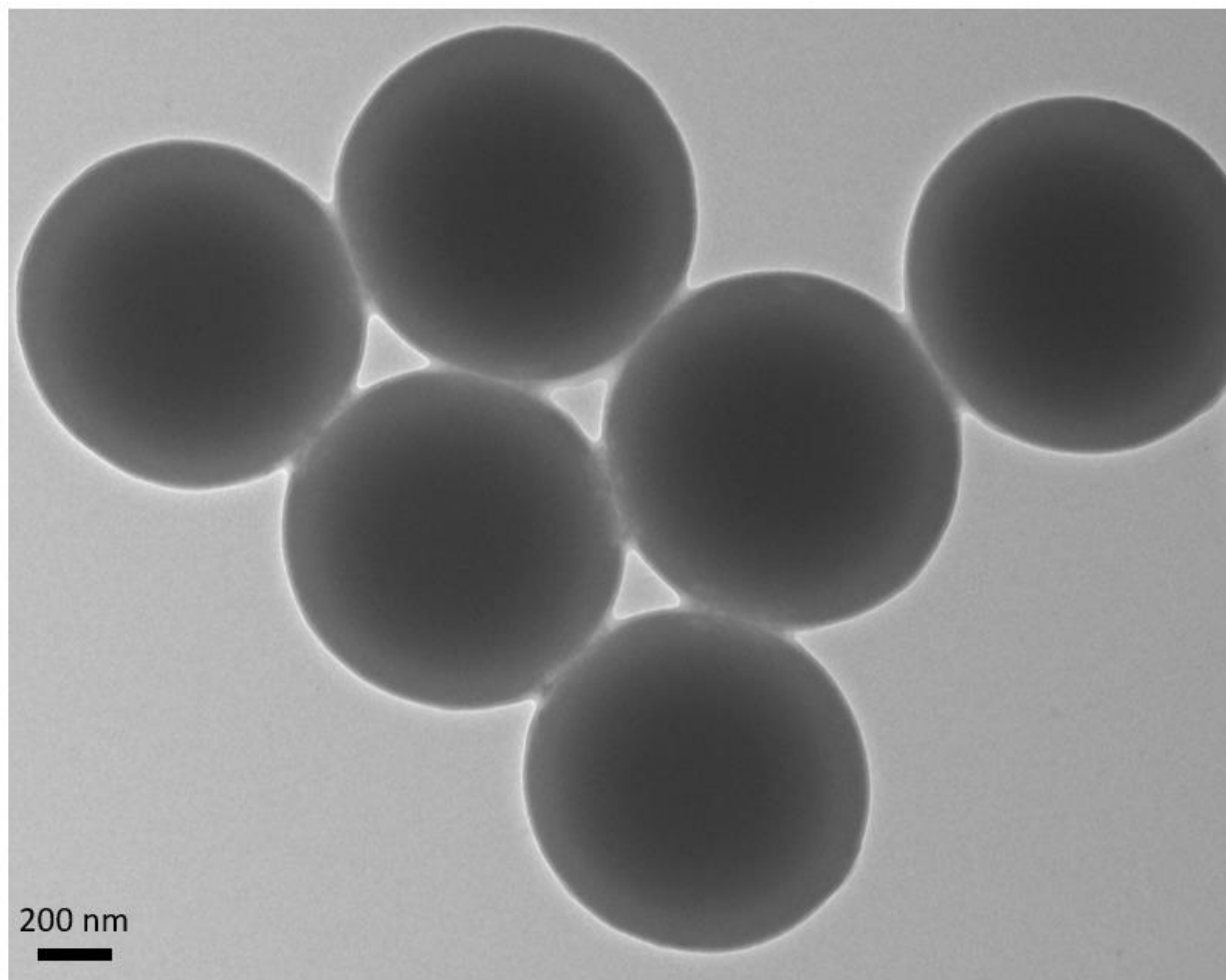


Figure 3.6. TEM image of particles with a PAAm brush layer from an in-column polymerization reaction (after depacking)

### ***Capillary Column Packing***

Prior to capillary packing, the tubing was conditioned using a syringe pump filled with 0.1 M NaOH for one hour at 100  $\mu\text{L}/\text{min}$ . It was then rinsed using  $\text{H}_2\text{O}$  for 15 minutes at the same flowrate.

A slurry was created using rehydroxylated silica particles at 30% w/w in 50/50 EtOH/ $\text{H}_2\text{O}$ . This was sonicated for approximately 15 minutes, prior to being pulled into a 20 cm segment of capillary tubing using a syringe. A packing frit was connected to one end of the capillary, the other connected to a pump which was set to a constant pressure of 7000 PSI, flowing 60/40 EtOH/ $\text{H}_2\text{O}$  for 30 minutes with the capillary under constant sonication, as illustrated in Figure 3.7. After packing, the capillary was placed into a desiccation chamber for approximately three days, until fully dry.

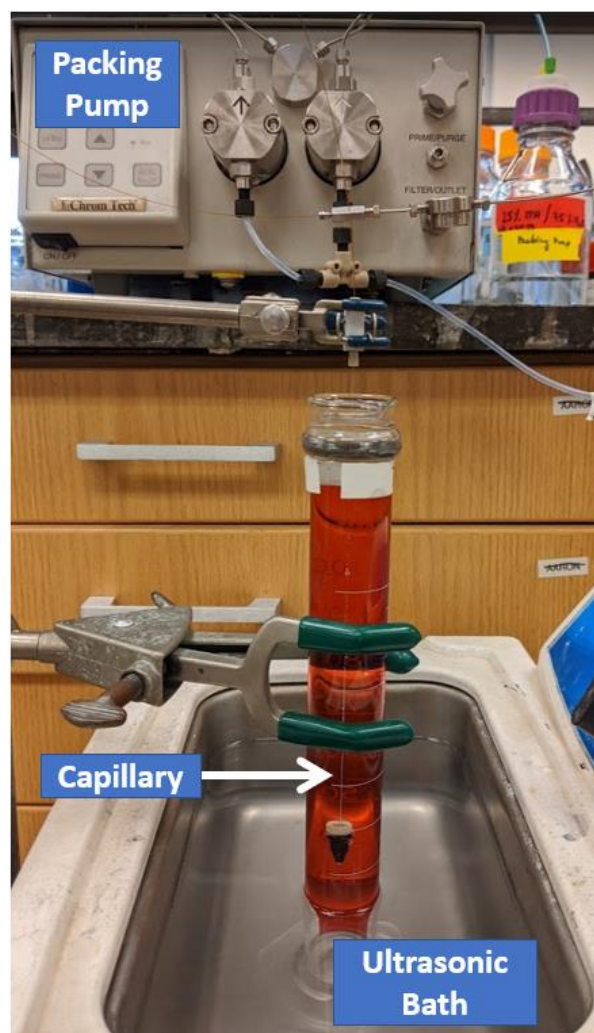


Figure 3.7. Photograph of capillary column packing hardware

### ***In-capillary Silane Modification***

After capillaries were packed and allowed to dry completely, they were subjected to an in-column silane reaction to functionalize the surface. This process involved an initial humidification step, where a thin layer of water was generated on the particle surfaces. This was achieved by placing the capillaries inside a lab-made humidification chamber which was kept at  $50 \pm 5\%$  RH for approximately three hours, illustrated in Figure 3.8.

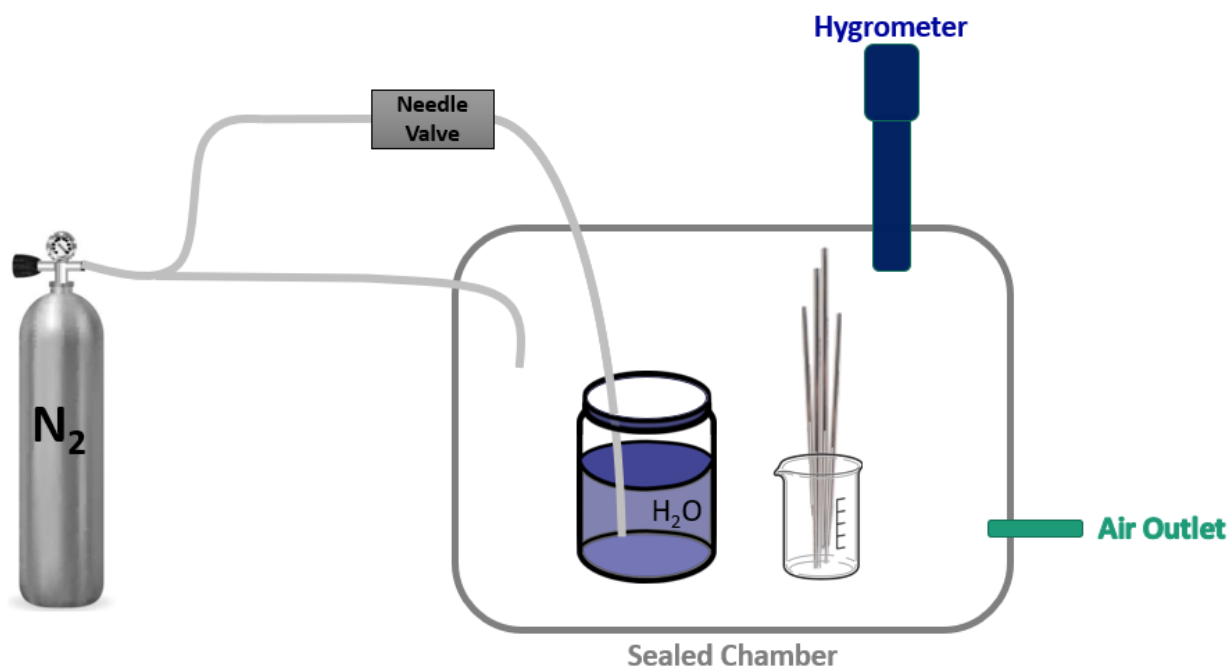


Figure 3.8. Diagram of humidification chamber used for particle surface conditioning prior to in-capillary silane modification

During the humidification process, a silane reaction mixture was created by adding 2 mL p-chloromethylphenyltrichlorosilane (tBC) and 0.5 mL methyltrichlorosilane (tC1) to 22.5 mL dry toluene. A 30 cm glass test tube was filled with 20 mL of this solution after prewetting three times, then the capillaries were placed into the tube with the packed bed at the bottom. The headspace was purged with nitrogen and a septum was placed on top of the test tube. A nitrogen-filled balloon was then connected to the test tube by linking the balloon to a needle which was inserted through the septum. A diagram of this setup is provided in Figure 3.9. The silane solution was wicked into the packed capillaries and the reaction was allowed to proceed overnight.

The following morning, the capillaries were removed one at a time from the test tube and individually rinsed with toluene for 15 minutes at 1000 PSI using the capillary packing pump shown earlier, with the packed bed facing the pump. After rinsing, each capillary was immediately placed into a 120 °C oven for 3 hours to condense the siloxane bonds. The capillaries were then set aside for subsequent polymer brush layer addition.

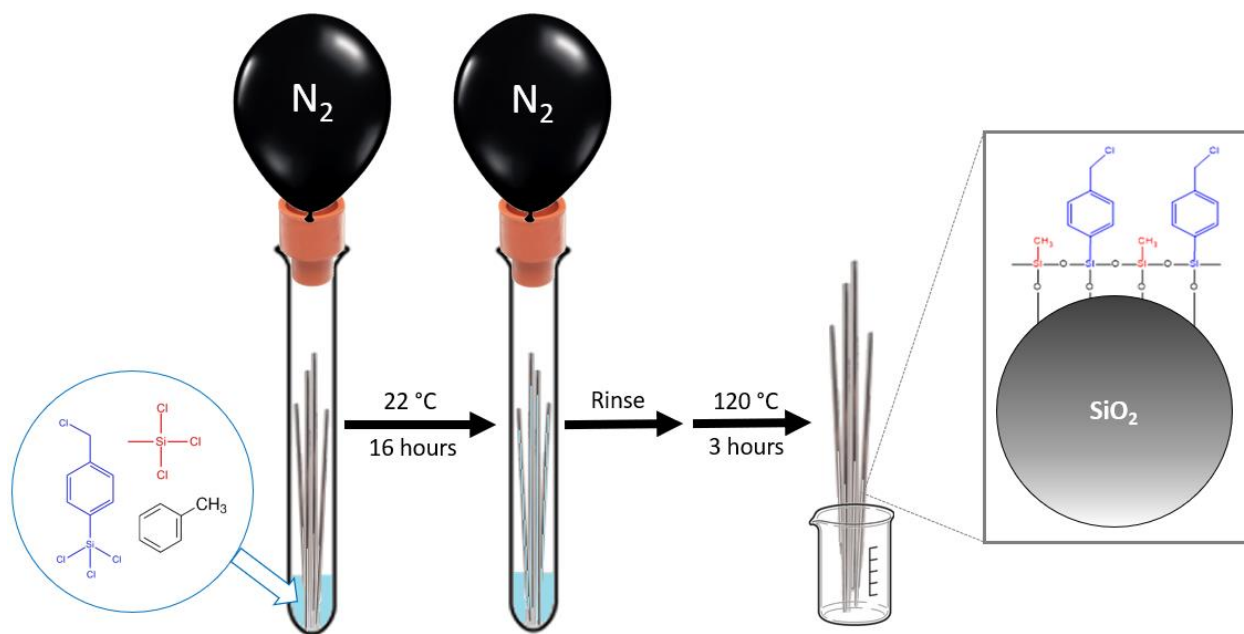


Figure 3.9. Diagram of in-capillary silane reaction

### ***In-capillary Polymer Modification***

After performing the in-capillary tBCl:C1 modification, a capillary was further modified to add a polymer brush layer to the surface using the tBCl as an initiator in the AGET-ATRP reaction described earlier in this chapter. Reaction mixtures were prepared as discussed earlier in this chapter. A 25 cm x 100  $\mu\text{m}$  capillary was used as a reservoir, and the reaction mixture was pulled into the reservoir using a syringe. The reservoir was connected to the pump and the capillary was connected to the reservoir with the packed bed facing the reservoir as illustrated in Figure 3.10. The reaction mixture was pumped into the packed capillary at 1000 PSI until packed bed was fully wetted, then for an additional 5 minutes. The flow was turned off, and the reaction was allowed to proceed for 60 minutes. For the PHMAAm-modified capillaries, the capillary and linked reservoir were placed into a  $38\text{ }^{\circ}\text{C}$  oven for the duration of this modification.

After the reaction was run for 60 minutes, the capillary was connected directly to the pump, with the packed bed facing the pump. The capillary was then rinsed for approximately 30 minutes at 2000 PSI using 50/50 EtOH/ $H_2O$ .

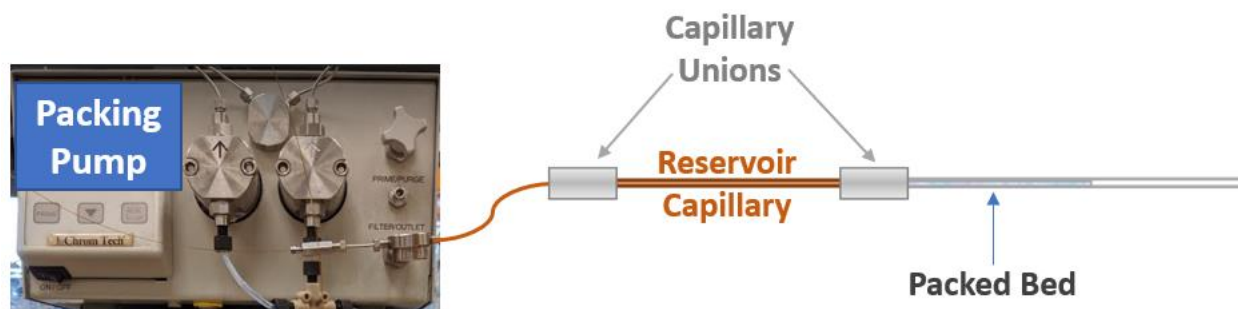


Figure 3.10. Diagram of apparatus used for in-capillary polymer modification

### ***Fluorescence Microscopy***

An inverted fluorescence microscope was used to image the labeled protein along the capillary column. The capillary column was connected to the nanoLC chromatograph using a reducing union, and was placed atop the microscope stage (Figure 3.11.) WinView software was used to control the CCD detector, using a gain of 40 and sampling rate of 2 Hz for all analyses. While there is the option to increase sensitivity by selecting a microscope objective with a greater magnification factor (assuming a larger numerical aperture), in this case a smaller magnification factor of 2x was selected in order to maximize the physical detection window. This enabled a broader view of analyte band separation in real-time, which was particularly useful when assessing the behavior at the head of the capillary column. After an analysis, images were captured using WinView and the raw data were exported as ASCII text for quantitative analysis using OriginPro.

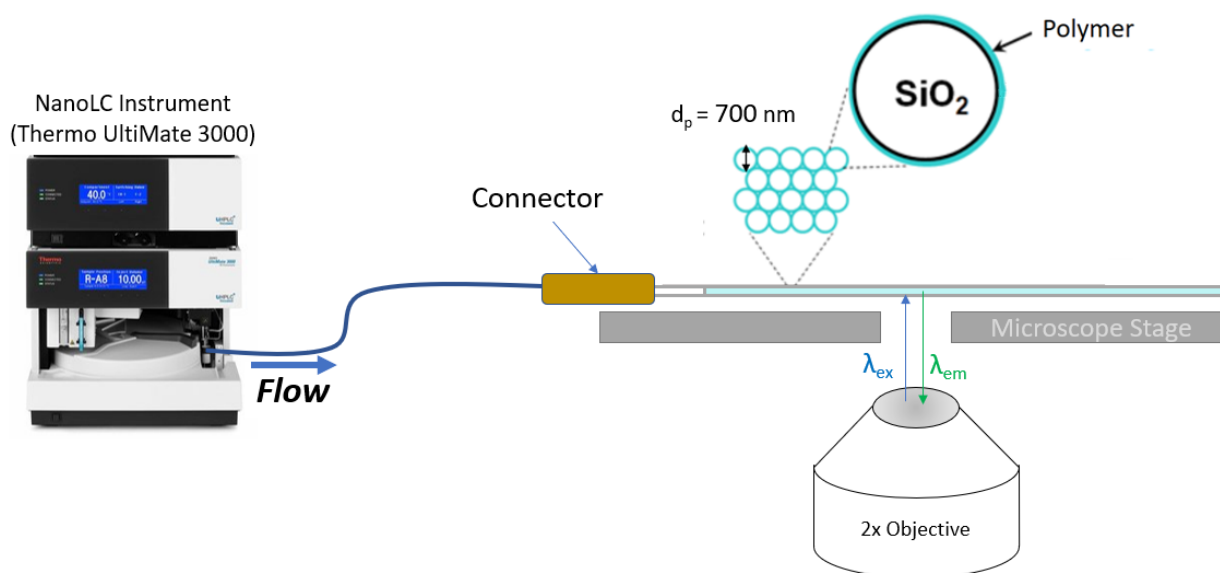


Figure 3.11. Diagram of instrumentation used in fluorescence microscopy-based analyses

### 3.3 Results and Discussion

#### 3.3.1 Bonded Phase Selection

The selection of bonded phase chemistry was an essential first step in this investigation. A mechanistic approach was chosen for this purpose, based upon the investigation into analyte selectivity discussed in Chapter 2. In order to assess bonded phase performance, standard-scale UHPLC columns were created using PAAm and PHMAAm brush layers on nonporous silica. PAAm columns were modified in-column, as discussed in the materials selection of this chapter. PHMAAm particles were modified ex-situ prior to packing.

Column performance was assessed by generating Snyder plots from multiple isocratic separations of RNase B at different mobile phase compositions (Figure 3.12). The slopes of the linear trendlines are presented in

Table 3.1. Based upon the increased spacing between the trendlines in the Snyder Plot (which indicated increased selectivity), PAAm was selected as the optimum bonded phase for future research.



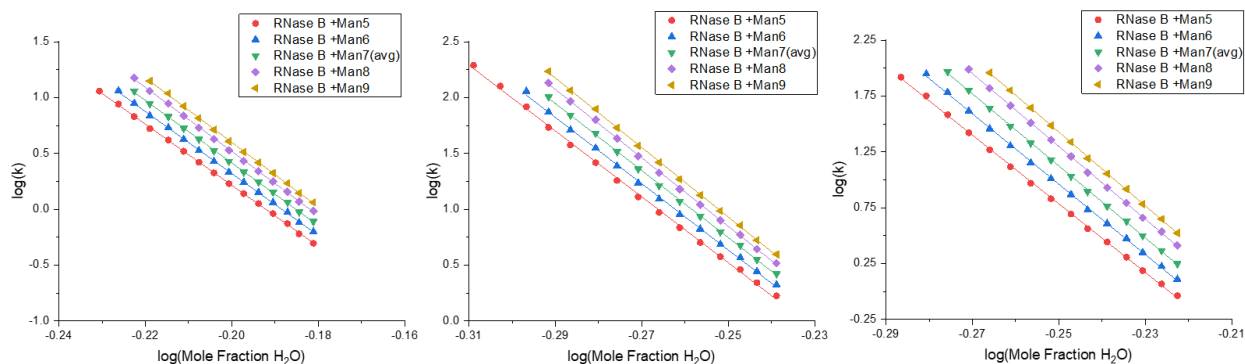


Figure 3.12. Snyder Plots for separation of RNase B glycoforms using a commercial amide column (left) compared with lab-made PHMAAm (center), and PAAM (right) columns. All are plotted over the same range to facilitate comparison.

Table 3.1. Slope data for the linear-fit trendlines illustrated in Figure 3.12.

	Man5	Man6	Man7 (avg)	Man8	Man9
Commercial Amide	27.4 ±0.1	27.8 ±0.1	28.0 ±0.1	28.7 ±0.2	28.9 ±0.2
PHMAAm	29.5 ±0.3	29.7 ±0.3	30.0 ±0.2	30.6 ±0.2	31.1 ±0.2
PAAM	30.8 ±0.2	31.5 ±0.2	32.2 ±0.1	32.6 ±0.2	33.0 ±0.2

### 3.3.2 On-column Focusing for NanoLC-Fluorescence Microscopy

An effective sample loading technique is necessary for effective nanoLC separations because of the large volume of sample injected for nanoLC analyses, relative to the mobile phase flowrate. Without focusing the sample band at the head of the column, the sharpest peak that is theoretically possible for a typical 50 nL injection with a flowrate of 100 nL/min would be 0.5 minutes. In practice, peak widths would be even greater due to band broadening during separation, meaning that an on-column focusing step is necessary for an acceptable separation. By using on-column focusing methods (colloquially referred to as “stacking”), a typical 50 nL injection plug can be focused to a ~20  $\mu\text{m}$  band at the head of the column. This yields a final volume of ~30 pL, giving a concentration factor of nearly 2,000x.

Performing this stacking step requires a weaker mobile phase solvent composition at the beginning of the gradient, providing full retention of the analyte. Optimizing this process was facilitated through direct, fluorescence microscopy-based detection of the chromatographic zone at the head of the column. This was made possible by leaving an empty segment of capillary in place when trimming the nanoHILIC capillary (illustrated in Figure 3.13).

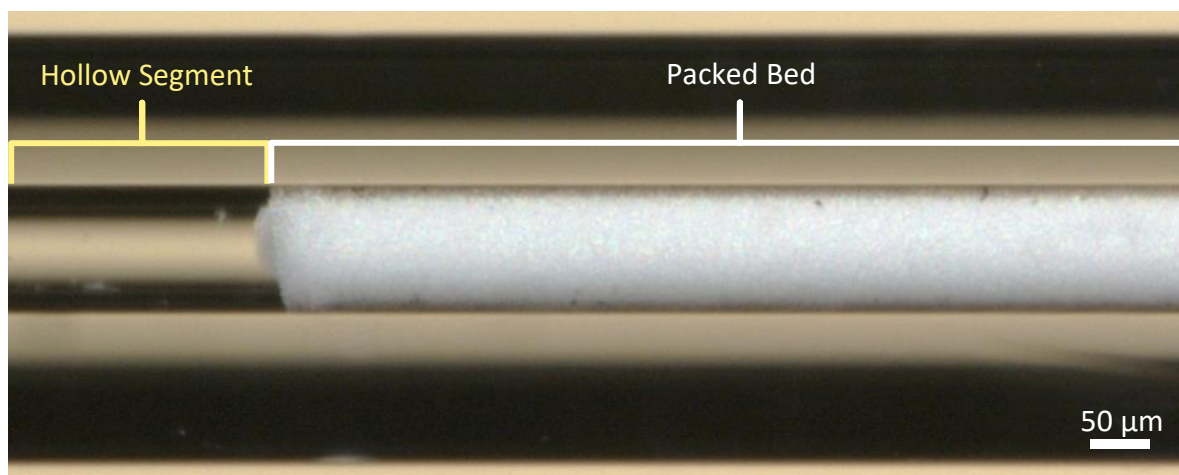


Figure 3.13. Image of the head of a packed capillary column with a segment of hollow capillary upstream, captured using an optical microscope at 11x.

Visualization of the stacking process required the use of an overabundance of protein in the labeling procedure—instead of using a 1 mg/mL protein solution for the labeling reaction as recommended by the manufacturer, the concentration was increased to 20 mg/mL. This alteration significantly reduced the effects of fluorescence quenching, allowing the zone to be imaged during the stacking process (Figure 3.14).

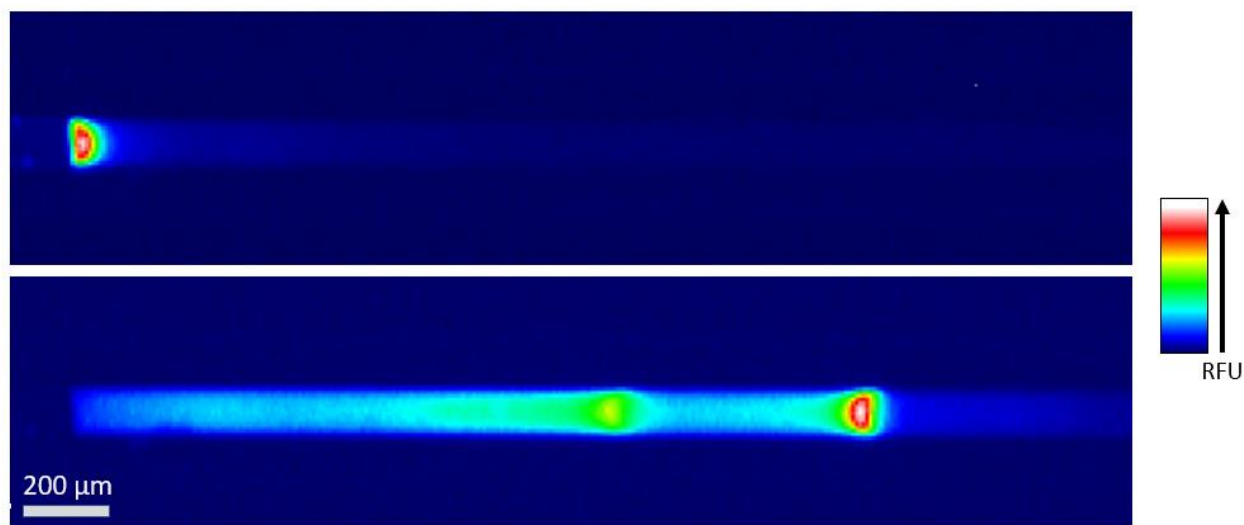


Figure 3.14. False-color fluorescence images of labeled protein analytes under stacking conditions (top) and 10 minutes into the gradient elution (bottom).

One of the necessary aspects of LC method optimization is choosing an appropriate sample diluent. A major drawback with protein HILIC is that the solubility of proteins in high concentrations of organic solvent is minimal. HILIC separation performance can be extremely sensitive to mismatches in sample solvent strength<sup>18</sup>, so this is an area of great concern.

While the stacking performance with RNase B is acceptable (but not optimal) when using a sample diluent of 75% ACN, this may not be acceptable for less-hydrophilic proteins such as mAbs, and can be improved using a weaker solvent composition for the diluent (Figure 3.15). Although protein solubility decreases sharply after increasing ACN concentrations beyond 75% ACN (even when using acidic solvent modifiers to improve solubility<sup>19</sup>) it was determined that the addition of 10% DMSO ameliorated this issue by improving the protein solubility. DMSO is also a weaker solvent than water in HILIC separations<sup>18</sup>, which may further improve stacking performance.

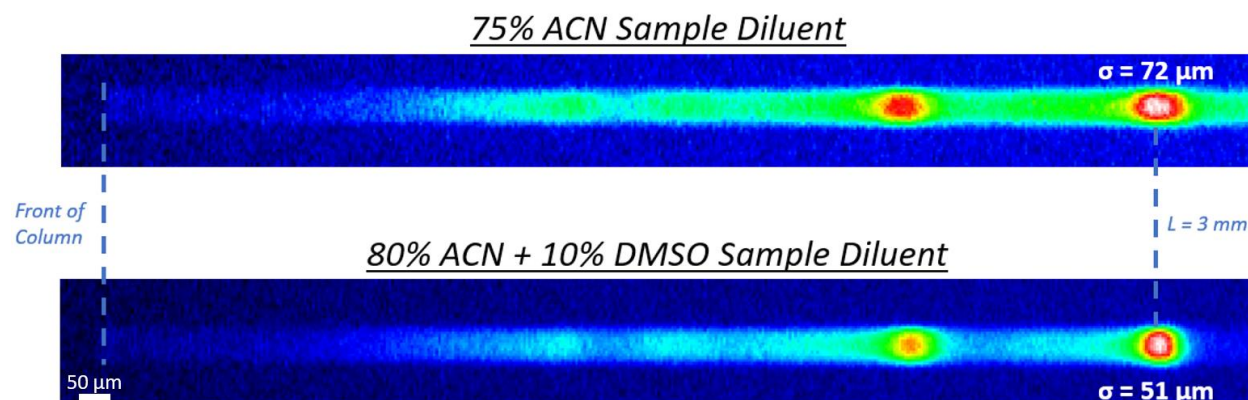


Figure 3.15. False-color fluorescence image demonstrating the narrower zone width resulting from improved sample diluent composition

### 3.3.3 Nano-HILIC Separation of Labeled Glycoproteins

Deliberately under-labeling the protein also proved advantageous for the remainder of the nanoLC-fluorescence microscopy experiments undertaken in this study. The A488 dye label, like many small molecule fluorophores<sup>20</sup>, consists of conjugated aromatic rings (Figure 3.16) so its addition can alter the protein's hydrophilic character and thus change its retention time in HILIC separations. Each additional label further impacts retention time (Figure 3.17), effectively splitting the peaks and producing more complex chromatograms (Figure 3.18). This can be problematic when attempting to optimize separation conditions, especially in cases where there is no clear baseline resolution between analyte species.

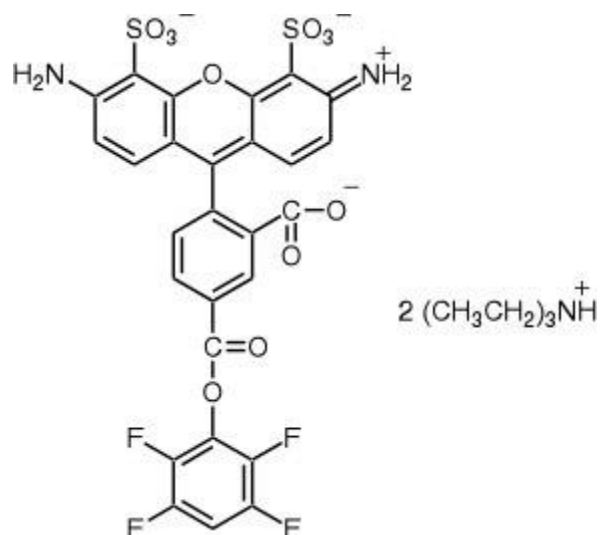


Figure 3.16. Structure of Alexa Fluor 488 fluorescent dye<sup>15</sup>

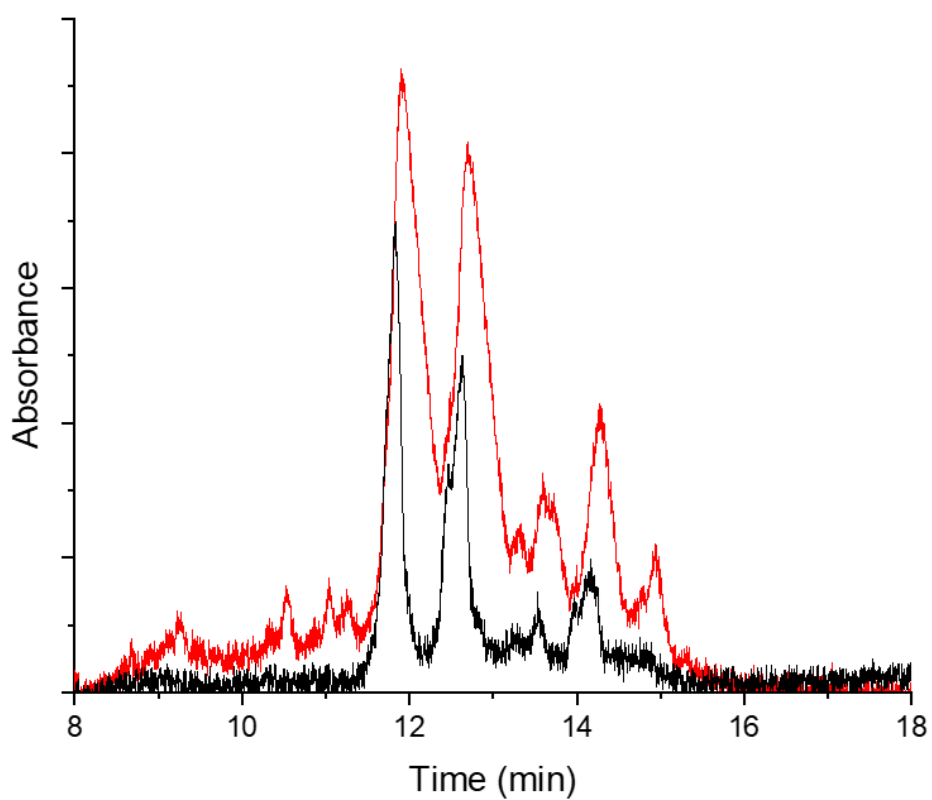


Figure 3.17. UV-visible chromatograms from a single analysis of an RNase B sample, post-labeling, with detection at different wavelengths. Labeled and unlabeled proteins absorb at 280 nm (red), but only the labeled proteins absorb at 495 nm (black)

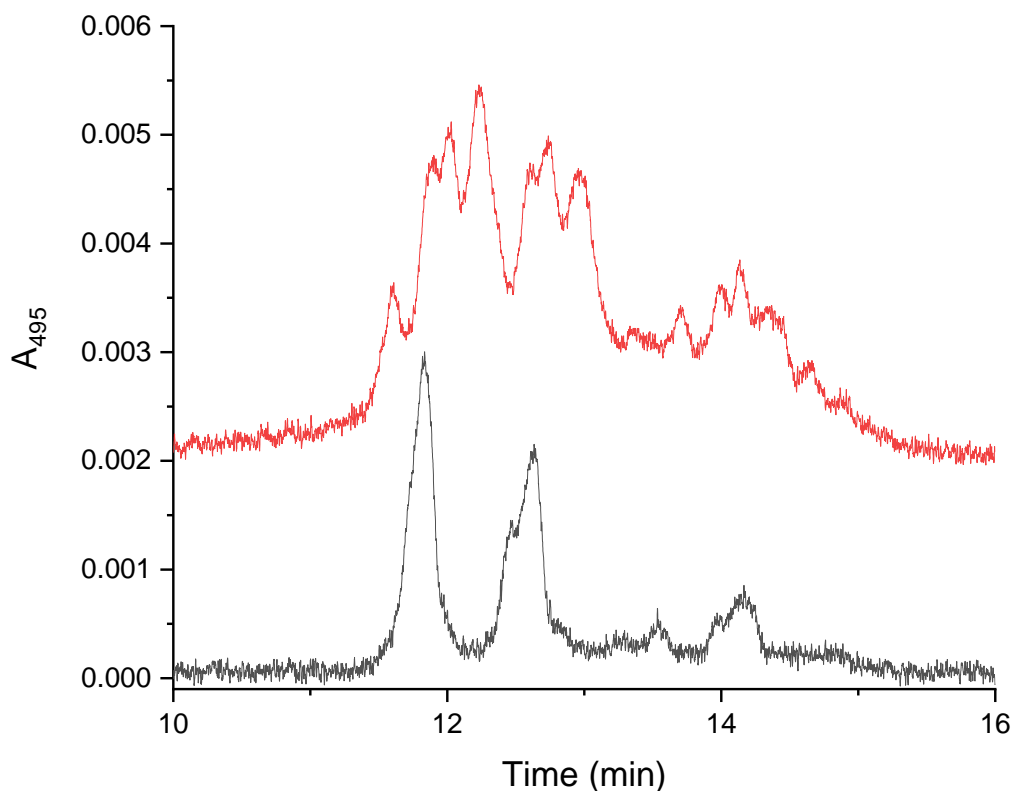


Figure 3.18. UV chromatograms illustrate the difference in complexity between labeled RNase B modified using the standard protocol (red) and under-labeling conditions (black)

After labeling RNase B using the modified protocol and reconstituting it in the optimized diluent, the labeled glycoprotein was utilized in optimizing the chromatographic conditions of the nanoLC separations in conjunction with fluorescence microscopy. This enabled the optimization of chromatographic methods without any additional variables introduced by post-column detection. The impact of post-column broadening for standard-scale UHPLC has been discussed in previous literature<sup>8</sup> and is an even greater concern with nanoLC<sup>21</sup>. This phenomenon was investigated in the development of the nanoHILIC-MS platform and will be discussed in the following chapter.

Multiple gradient profiles were investigated while monitoring fluorescence intensity at a position of 3 cm from the head of the PAAm capillary column. A flowrate of 70 nL/min was selected based on backpressure limitations, and an optimum balance of peak width and selectivity was achieved using a gradient of 75% - 60% ACN over 30 minutes (Figure 3.19, Figure 3.20). Separations utilized 0.1% FA and 0.025% TFA mobile phase modifiers, which were selected to

minimize ion suppression effects introduced by the ion-pairing agent TFA<sup>22</sup>, while still protonating residual silanols on the particle surface to reduce peak tailing.

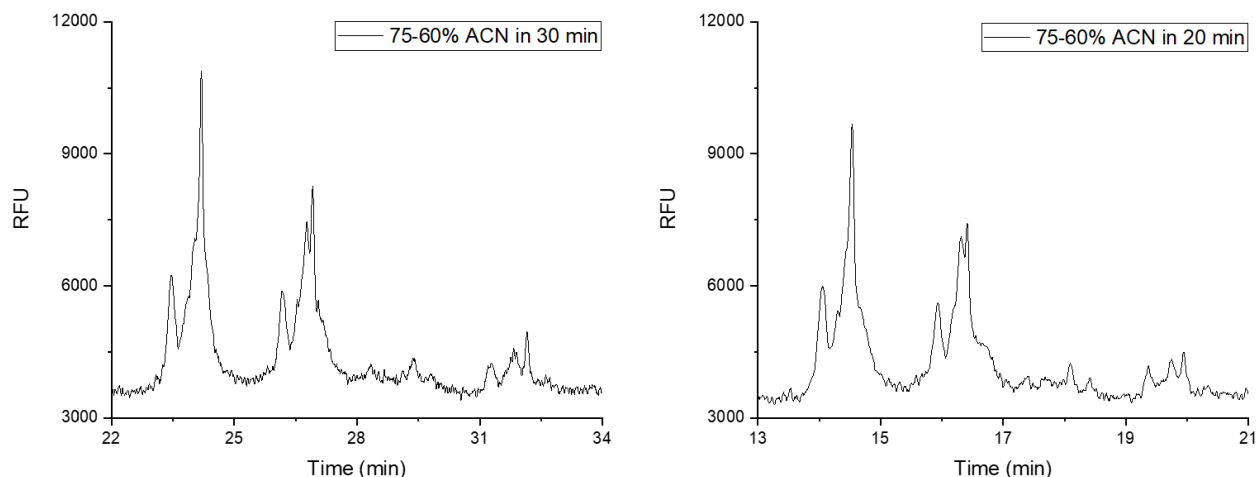


Figure 3.19. Comparison of different gradient slopes for separation of labeled RNase B using a 3 cm PAAm-modified capillary— $\Delta B = 15\%$  over 30 minutes (left) and over 20 minutes (right)

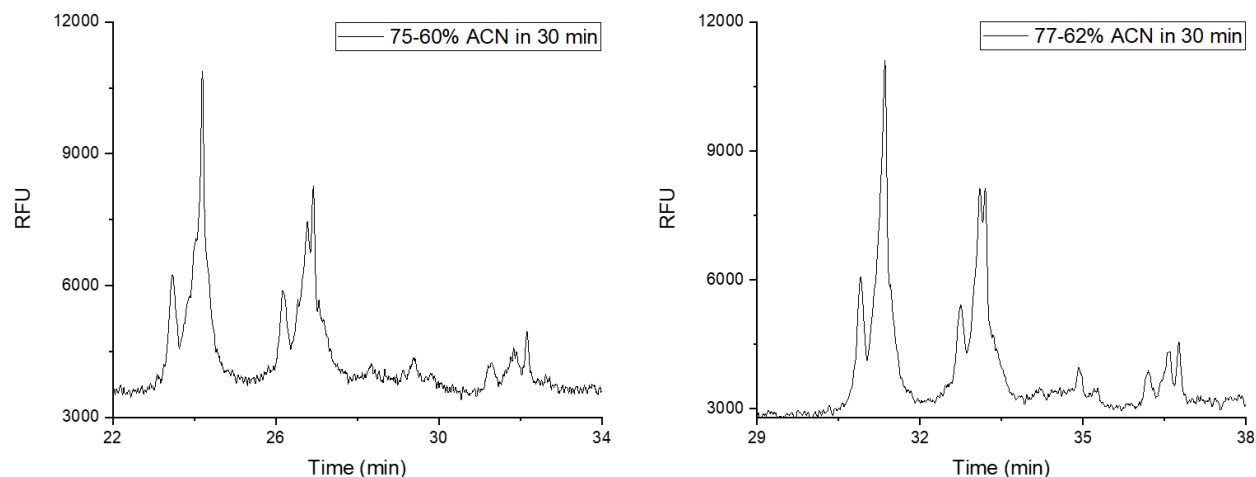


Figure 3.20. Comparison of different gradient start points for separation of labeled RNase B using a 3 cm PAAm-modified capillary, starting at 75%B (left) vs. 77%B (right)

After optimizing gradient conditions, the impact of column length was investigated. Using fluorescence microscopy with a translucent capillary enables analysis at multiple positions for the same column. This minimizes artifacts which may be introduced by differences in column packing, particle modification, or backpressure that might arise when comparing two separate columns. In comparing the separation at different points along the column it becomes clear that increasing the

length of the column continues to provide improved resolution and the elucidation of additional peaks. This holds true along the entirety of a 3 cm column, as illustrated by the chromatograms in Figure 3.21. Although one can also look at the size of chromatographic zones in the physical domain, a fair comparison of the zone width at different positions along the column cannot be made for this analyte, as each major peak begins to separate into multiple peaks along the length of the column (Figure 3.22). This introduces apparent band broadening that is actually caused by separation of previously co-eluting peaks as the effective column length increases.

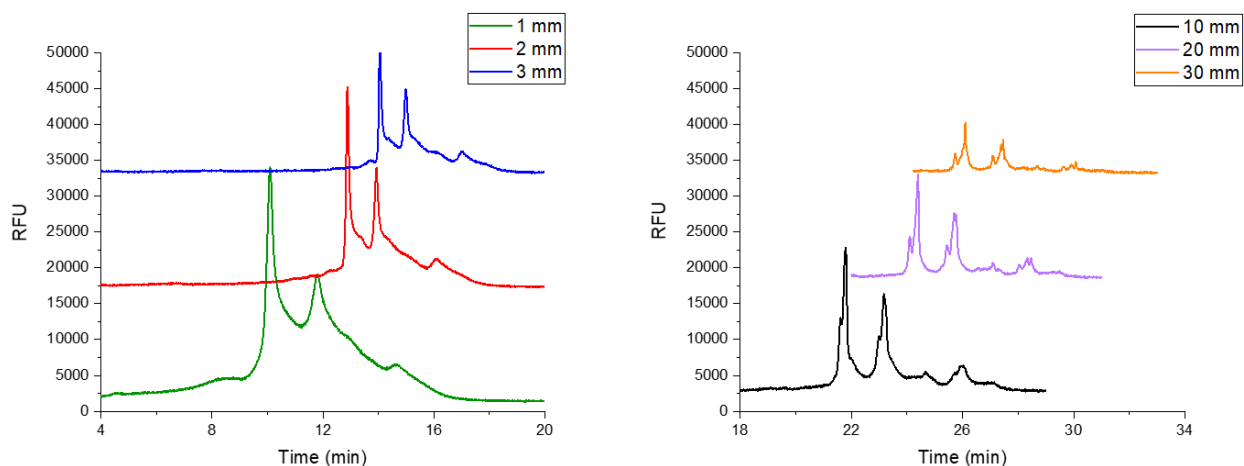


Figure 3.21. Chromatograms obtained at different positions along the same capillary column

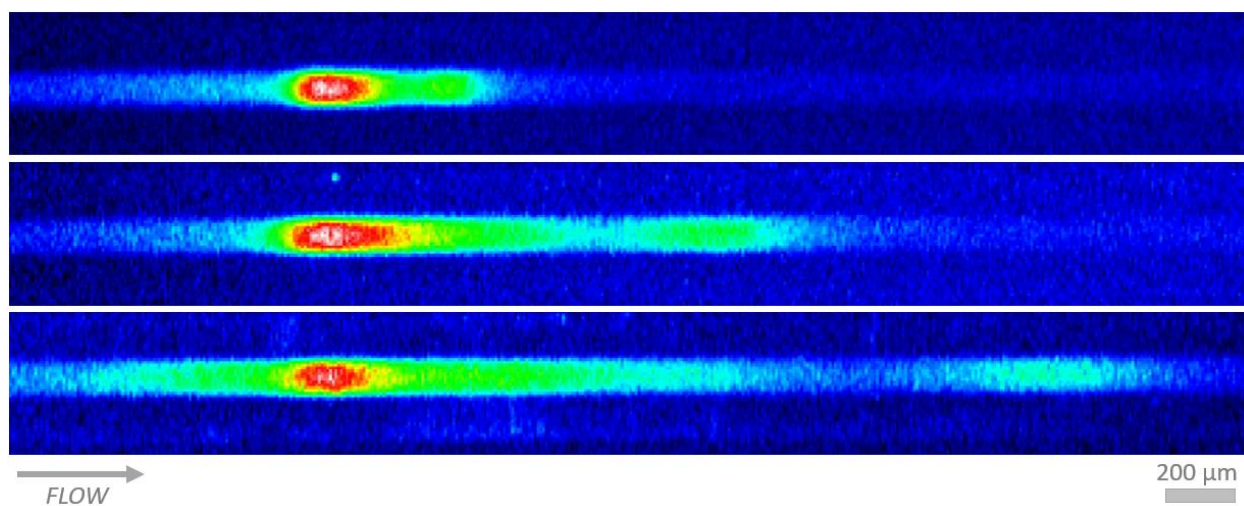


Figure 3.22. False-color fluorescence images of the chromatographic zone from RNase B (+Man5) at different positions along the same capillary column (top to bottom: 1 cm, 2 cm, 3 cm.) The minor peak on the right is believed to be the same glycoprotein with an additional label



### 3.4 Conclusion

Capillary columns containing nonporous silica with a PAAm polymer brush layer were proven to be effective in their separation of the fluorescent dye-labeled glycoforms of RNase B. After creating columns using in-column silane and polymer modification techniques, it was determined that the resolution for gradient separations continued to improve along the entire length of the 3 cm column. With this in mind, it appears that the balance which must be considered is between the improved resolution for progressively longer columns vs. the backpressure that the longer columns present. It is likely that increasing the length of the packed bed to an extreme may introduce diminished performance due to particle packing inefficiencies, but that concern was not addressed in this investigation.

Although separation of the fluorescent dye-labeled proteins was clearly successful, this acts more as a proof-of-concept than a useable, finished method. Protein labeling is expensive, laborious, and can introduce increasing levels of sample complexity due to variable degrees of labeling. This increased complexity can introduce additional peaks which may be misinterpreted as indicating that there are more species present in the original, unlabeled sample than are actually present. Coupling the nanoHILIC platform to a mass spectrometer could provide the ability to detect unlabeled glycoproteins and give mass information for assistance in identifying sample constituents. This was further investigated and will be discussed in the following chapter.

### 3.5 References

1. Zhang, Z.; Wu, Z.; Wirth, M. J., Polyacrylamide brush layer for Hydrophilic Interaction Liquid Chromatography of intact glycoproteins. *J Chromatogr A* **2013**, *1301*, 156-61.
2. Huckabee, A. G.; Yerneni, C.; Jacobson, R. E.; Alzate, E. J.; Chen, T.-H.; Wirth, M. J., In-column bonded phase polymerization for improved packing uniformity. *Journal of Separation Science* **2017**, *40* (10), 2170-2177.
3. Xiao, D.; Wirth, M. J., Kinetics of Surface-Initiated Atom Transfer Radical Polymerization of Acrylamide on Silica. *Macromolecules* **2002**, *35* (8), 2919-2925.
4. Peters, A.; Candau, S. J., Kinetics of swelling of polyacrylamide gels. *Macromolecules* **1986**, *19* (7), 1952-1955.
5. Mandal, J.; Simic, R.; Spencer, N. D., Impact of dispersity and hydrogen bonding on the lubricity of poly (acrylamide) brushes. *Advanced Materials Interfaces* **2019**, *6* (14), 1900321.

6. Karlsson, H.; Larsson, J. M.; Thomsson, K. A.; Hard, I.; Backstrom, M.; Hansson, G. C., High-throughput and high-sensitivity nano-LC/MS and MS/MS for O-glycan profiling. *Methods Mol Biol* **2009**, *534*, 117-31.
7. Ljunglöf, A.; Hjorth, R., Confocal microscopy as a tool for studying protein adsorption to chromatographic matrices. **1996**, *743* (1), 75-83.
8. Vanderlinden, K.; Broeckhoven, K.; Vanderheyden, Y.; Desmet, G., Effect of pre- and post-column band broadening on the performance of high-speed chromatography columns under isocratic and gradient conditions. **2016**, *1442*, 73-82.
9. Prüß, A.; Kempter, C.; Gysler, J.; Jira, T., Extracolumn band broadening in capillary liquid chromatography. *Journal of Chromatography A* **2003**, *1016* (2), 129-141.
10. Beisler, A. T.; Schaefer, K. E.; Weber, S. G., Simple method for the quantitative examination of extra column band broadening in microchromatographic systems. *Journal of Chromatography A* **2003**, *986* (2), 247-251.
11. Toseland, C. P., Fluorescent labeling and modification of proteins. *Journal of chemical biology* **2013**, *6* (3), 85-95.
12. Ghisaidoobe, A.; Chung, S., Intrinsic Tryptophan Fluorescence in the Detection and Analysis of Proteins: A Focus on Förster Resonance Energy Transfer Techniques. *International Journal of Molecular Sciences* **2014**, *15* (12), 22518-22538.
13. Oefner, P. J.; Huber, C. G.; Umlauf, F.; Berti, G. N.; Stimpfl, E.; Bonn, G. K., High-Resolution Liquid Chromatography of Fluorescent Dye-Labeled Nucleic Acids. **1994**, *223* (1), 39-46.
14. Panchuk-Voloshina, N.; Haugland, R. P.; Bishop-Stewart, J.; Bhalgat, M. K.; Millard, P. J.; Mao, F.; Leung, W.-Y.; Haugland, R. P., Alexa Dyes, a Series of New Fluorescent Dyes that Yield Exceptionally Bright, Photostable Conjugates. *Journal of Histochemistry & Cytochemistry* **1999**, *47* (9), 1179-1188.
15. Invitrogen, Alexa Fluor™ 488 Protein Labeling Kit. ThermoFisher: p <https://www.thermofisher.com/order/catalog/product/A10235>.
16. Van Le, T.; Ross, E. E.; Velarde, T. R. C.; Legg, M. A.; Wirth, M. J., Sintered Silica Colloidal Crystals with Fully Hydroxylated Surfaces. *Langmuir* **2007**, *23* (16), 8554-8559.
17. Min, K.; Gao, H.; Matyjaszewski, K., Preparation of Homopolymers and Block Copolymers in Miniemulsion by ATRP Using Activators Generated by Electron Transfer (AGET). **2005**, *127* (11), 3825-3830.
18. Ruta, J.; Rudaz, S.; McCalley, D. V.; Veuthey, J.-L.; Guilleme, D., A systematic investigation of the effect of sample diluent on peak shape in hydrophilic interaction liquid chromatography. *Journal of Chromatography A* **2010**, *1217* (52), 8230-8240.

19. Lauber, M. A.; Yu, Y.-Q.; Brousmiche, D. W.; Hua, Z.; Koza, S. M.; Magnelli, P.; Guthrie, E.; Taron, C. H.; Fountain, K. J., Rapid Preparation of Released N-Glycans for HILIC Analysis Using a Labeling Reagent that Facilitates Sensitive Fluorescence and ESI-MS Detection. *Anal Chem* **2015**, 87 (10), 5401-9.
20. Fu, Y.; Finney, N. S., Small-molecule fluorescent probes and their design. *RSC Advances* **2018**, 8 (51), 29051-29061.
21. Jung, M. C. Major Sources of Post-column Peak Broadening in nanoLC. <https://www.waters.com/webassets/cms/library/docs/720006526en.pdf> (accessed March 20, 2020).
22. Annesley, T. M., Ion Suppression in Mass Spectrometry. *Clinical Chemistry* **2003**, 49 (7), 1041-1044.

## CHAPTER 4. NANO-HILIC-MS FOR SEPARATION OF PROTEINS AND GLYCOPROTEINS ON THE SUB-FEMTOMOLE LEVEL

### 4.1 Introduction

The nanoLC platform introduced in the previous chapter serves as a solid foundation for a robust analytical method, but is not an exceptionally practical tool in and of itself due to the requirement of an intrinsically fluorescent or fluorescently-labeled analyte. Incorporating a more universal detection method would remove this caveat. Using mass spectrometry to overcome this limitation would not only bring the method into the realm of practicality, but it would add an orthogonal stream of data: analyte mass information.

With a mass spectrometer as the “back-end” of this platform, the resulting data could be leveraged to properly identify the glycoprotein species as they elute from the column. This would be particularly useful in cases where there is no a priori knowledge of the identities of the protein glycoforms and/or their anticipated retention order. Extracted ion chromatograms (EICs) could also provide a means to analytically resolve co-eluting species which may otherwise be impossible to separate using simple UV or fluorescence detection.

One of the main advantages of using a nano-scale LC-MS platform compared to traditional LC-MS is the drastic increase in sensitivity<sup>1</sup>. Lower volumetric flowrates for nanoLC can correspond to increased analyte concentration in the center of a chromatographic zone<sup>2</sup>. Signal is enhanced due to a greater ionization efficiency; nanospray droplets are an order of magnitude smaller than those emitted from a traditional ESI source<sup>3</sup>, allowing more rapid desolvation in the Taylor cone and jet stream<sup>4,5</sup>. Further, with fewer analyte molecules to ionize, charge-competition is minimized<sup>6</sup>. The decrease in mobile phase volume also yields a corresponding decrease in background noise caused by additives and trace solvent impurities<sup>3</sup>.

Migrating the nanoLC platform to incorporate mass spectrometry-based detection proved to be more involved than simply linking the capillary to a commercially available needle emitter. A hollow segment of post-column tubing has been shown to drastically distort peak shapes and diminish chromatographic resolution, as discussed in previous literature from multiple sources<sup>7-10</sup>. This is largely due to the parabolic flow profile introduced in an empty tube, referred to as “Poiseuille flow”<sup>11</sup>. This type of broadening can be calculated in a straightforward manner for a segment of cylindrical tubing based upon the Navier-Stokes equation written in cylindrical

coordinates (Equation 4.1)<sup>12</sup>. In this case,  $z$  represents the position along the length axis of the pipe,  $r$  represents the distance from the center of the flow,  $a$  is the radius of the pipe,  $P(z)$  indicates the backpressure at position  $z$ , and  $\eta$  represents the viscosity of the liquid.

$$\eta \left( \frac{\partial^2 u}{\partial r^2} + \frac{1}{r} \frac{\partial u}{\partial r} \right) = \frac{\partial P(z)}{\partial z}$$

Equation 4.1.

In his 1956 paper, R. Aris utilized the previous equations to derive the anticipated dispersion of a chromatographic analyte flowing through an open capillary<sup>13</sup>, as presented in Equation 4.2. For this equation,  $\sigma^2$  represents the volumetric variance introduced by the open tube,  $r$  is the tube radius,  $D$  is the diffusion coefficient, and  $F_v$  represents the volumetric flowrate<sup>14</sup>. Solving Aris's equation, therefore, requires knowledge of the diffusion coefficient of the analyte-of-interest. As the diffusion coefficient for molecules dissolved in H<sub>2</sub>O can be calculated as  $D \approx (M)^{-0.33}$ , it becomes clear that the band broadening caused by Poiseuille flow is significantly diminished for proteins relative to that for small molecules<sup>15</sup>. It should be noted that  $D$  scales inversely with the viscosity of the mobile phase as shown in the Stokes-Einstein relation (Equation 4.3)<sup>16, 17</sup>. As such, this band broadening will increase in an ACN-rich HILIC mobile phase due to its significantly diminished viscosity relative to that of pure water<sup>18</sup>. For Equation 4.3,  $k$  represents the Boltzmann constant,  $T$  is the temperature (in Kelvin),  $r$  represents the hydrodynamic radius of the molecule, and  $\eta$  is the viscosity of the liquid.

$$\sigma^2 = \frac{1}{24} \frac{\pi r^4 L}{D} F_v$$

Equation 4.2.

$$D = \frac{kT}{6\pi\eta r}$$

Equation 4.3.

In reality, zone broadening introduced by a hollow needle emitter is considerably more complex than the above representation. The underlying Navier-Stokes equation assumes an

incompressible liquid<sup>12, 19</sup>, which is not the case for an ACN/H<sub>2</sub>O mixture<sup>20</sup>, and does not apply in the case of the tapered segment near the point of the emitter<sup>21</sup>. These limitations can be resolved through computational methods, where the profile of the original peak can be convolved with the output of a computational fluid dynamics (CFD) simulation<sup>22</sup>. Performing this task requires the initial creation of a three-dimensional model using computer-aided design (CAD) software, which is a trivial task when modeling the flow path through the needle emitter. The results from this simulation can be compared with empirical data to determine the goodness-of-fit for the model, and significant deviations from the model can act as a flag indicating the presence of one or more external variables. This insight can be used to design and apply a better interface for the separation of glycoproteins.

## **4.2 Experimental**

### **4.2.1 Materials**

For electrospray, PicoTip needle emitters with a 75  $\mu\text{m}$  inner diameter and hole size of 8  $\mu\text{m}$  were purchased from New Objective. These emitters were silica-based, with an outer diameter of 360  $\mu\text{m}$  and length of 20 cm. The PTFE sleeve used to link a hollow needle emitter to a packed capillary was obtained from Vici.

A Thermo LTQ Velos linear ion trap mass spectrometer was used as a detector, in conjunction with Thermo Excalibur software for data analysis and Zhang & Marshall's MagTran software<sup>23</sup> for peak deconvolution. Ion chromatograms were plotted using OriginPro from OriginLab.

The humanized monoclonal antibody standard (SRM 8671) was obtained from NIST. Immunoglobulin-degrading enzyme from *Streptococcus pyogenes* (IdeS) was purchased from Genovis. All additional equipment and reagent sources are as described in Chapters 2 and 3.

### **4.2.2 Methods**

#### ***Fluorescence Microscopy of Linked Needle Emitter***

For imaging the separation of labeled glycoprotein after its passage through the hollow needle emitter, the capillary column was linked to the emitter using a PTFE sleeve. A portable fan was used to help evaporate solvent as it flowed out of the emitter in order to prevent a droplet from

accumulating and obscuring the view of the analyte bands. A diagram is provided in Figure 4.1 for clarity, with a photograph of the capillary and linked emitter shown in Figure 4.2.

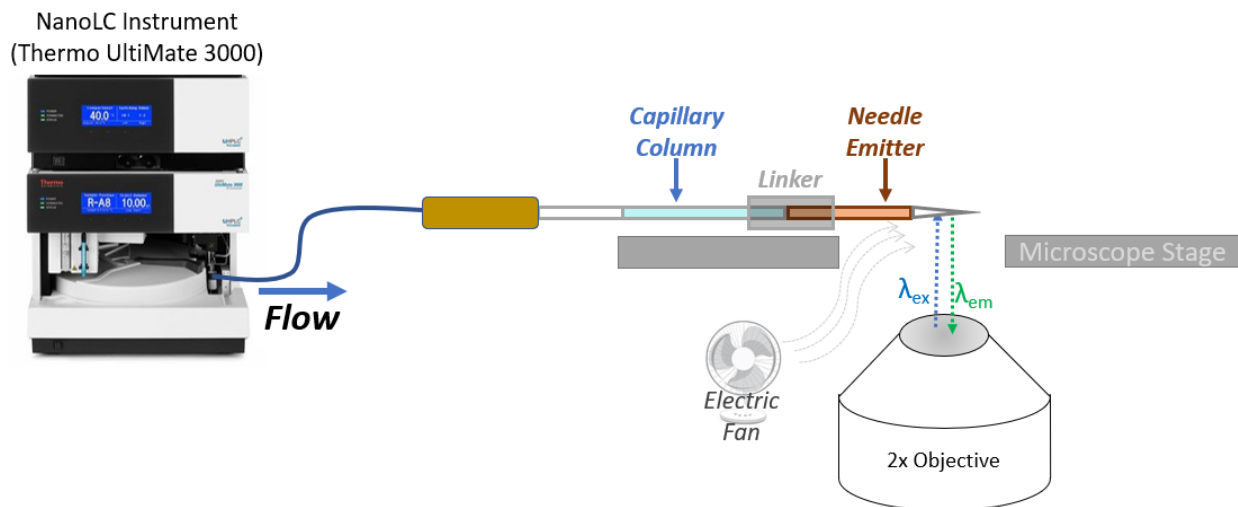


Figure 4.1. Diagram of setup used in imaging the tip of a hollow needle emitter, post-capillary



Figure 4.2. Photograph of capillary column (left) linked to a hollow needle emitter (right) using a PTFE sleeve

### ***Needle Emitter Preparation & Packing***

To prevent breakage caused by stress corrosion<sup>24</sup>, the empty needle emitters were given a hydrophobic coating prior to packing. This was achieved using a gas-phase tC1 reaction. The emitters were placed into a graduated cylinder, with the pointed end facing up, and the downward-facing end kept approximately 5 cm above the bottom of the graduated cylinder. This was accomplished by simply holding the emitters against the side of the graduated cylinder when inserting them; static electricity kept them in place during the course of the gas-phase reaction.

The graduated cylinder containing the emitters was then capped with a septum and connected to the lab-made humidification chamber described in the previous chapter. After

stabilizing the humidification chamber at 50% RH, the chamber and graduated cylinder were connected using Tygon® tubing as illustrated in Figure 4.3.

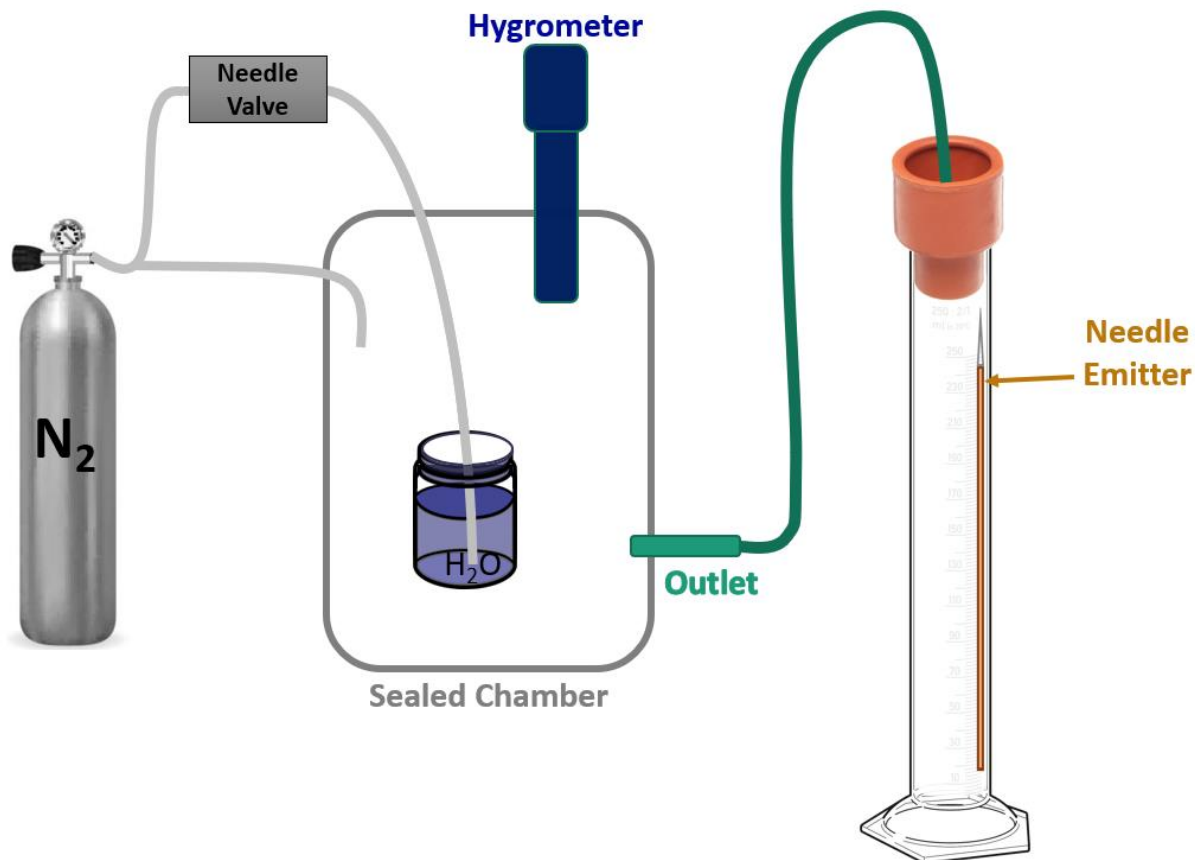


Figure 4.3. Diagram of the equipment used in surface humidification for the gas-phase silylation of needle emitter tips

Once these two containers were linked, another needle was connected to a 30 mL syringe and subsequently inserted into the septum atop the graduated cylinder. The air from the humidification chamber was pulled into the graduated cylinder by filling the 30 mL syringe a total of ten times, disconnecting the needle from the syringe each time to expel the air collected within the syringe.

After waiting 30 minutes to allow the necessary water layer to accumulate on the surface of the emitters, a mixture of 4.5 mL dry toluene and 0.5 mL tC1 were injected through the septum into the graduated cylinder. Care was taken to keep the needle emitters above the surface of the



reaction mixture. A nitrogen filled balloon was connected to the graduated cylinder, and this reaction was allowed to run overnight.

The following morning, the needle emitters were rinsed with toluene by connecting the unsharpened side of the emitter to a 6 mL syringe with a PTFE sleeve and slowly drawing 5 mL toluene through the emitter. Finally, the hollow emitters were placed into a 120 °C oven for three hours in order to condense the siloxane bonds.

Superficially porous particles with a diameter of 2.7  $\mu\text{m}$  were modified ex-situ to give a PHMAAm coating as described in the previous chapter. A slurry containing these particles at 5% w/v in 50/50 EtOH/H<sub>2</sub>O was drawn into a 5 cm x 100  $\mu\text{m}$  reservoir capillary which was connected to a capillary packing pump on one side and a tC1-coated needle emitter on the other side, as shown in Figure 4.4. Columns were packed at 7000 PSI for 30 minutes with sonication, then 5 additional minutes without sonication. Despite the opening of the tip being approximately 3x the size of the superficially-porous particles, the particles were held in place due to the keystone effect<sup>25</sup>. As a result, this process created a frit of approximately 1 mm in length at the end of the needle emitter (Figure 4.5).

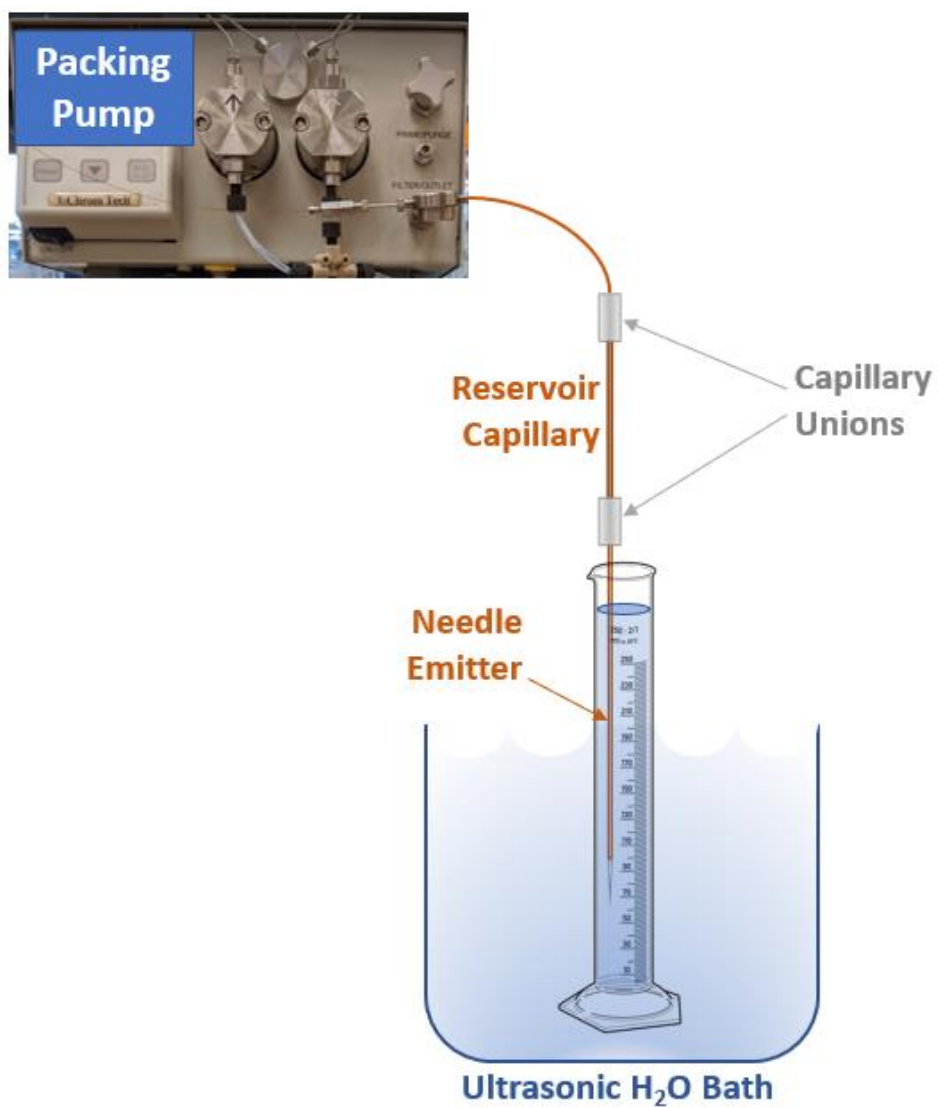


Figure 4.4. Schematic of the apparatus utilized in packing needle emitters

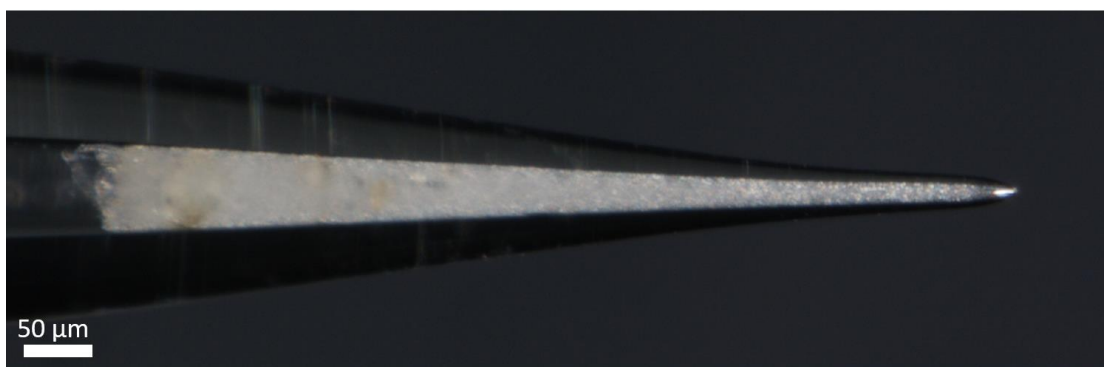


Figure 4.5. An image of a fritted needle emitter, containing a 1 mm segment of PHMAAm-coated superficially porous particles. Captured using an optical microscope at 11x zoom

Nonporous mBC:mC1-coated particles with a 700 nm diameter were created as described in Chapter 3. They were then packed into the needle emitter against the superficially porous particle frit. This was achieved by filling a 30 cm x 100  $\mu$ m reservoir capillary with a slurry containing the mBC:mC1 particles at 30% w/v in 50/50 EtOH/H<sub>2</sub>O, which was then connected to the pump and newly-fritted needle emitter as shown in Figure 4.4. Packing was performed at 7000 PSI for 30 minutes under sonication, followed by an additional 10 minutes without sonication. After packing, needle emitters were trimmed to remove the hollow capillary tubing and dried under ambient conditions for three days.

### ***Bonded Phase Synthesis***

After packing a needle emitter with mBC:mC1-modified particles, PAAm AGET-ATRP reaction solutions were created as described in Chapter 3. After combining the three solutions, the resulting mixture was loaded into a 30 cm x 100  $\mu$ m reservoir capillary using a syringe. The reservoir was then connected to the blunt side of the needle emitter using PEEK ferrules and stainless-steel capillary union, with the other end connected to the packing pump as illustrated in Figure 3.10.

The reaction mixture was pumped into the packed needle emitter at 1000 PSI until a droplet formed at the end of the emitter, then for an additional 5 minutes. At this time, flow was halted and the reaction was allowed to proceed for 60 minutes. The packed emitter was then disconnected from the reservoir and connected to the pump directly for a 30-minute rinse with 75/25 H<sub>2</sub>O/IPA.

### ***Mass Spectrometer Configuration***

A Thermo LTQ Velos linear ion trap mass spectrometer was used in positive ionization mode for all analyses. Nitrogen was used as a sweep gas for standard UHPLC-MS, set at a pressure of 40 PSI. No sweep or sheath gas was utilized for nanoLC-MS analyses.

Ion optics and detector parameters were optimized for UHPLC-MS using LTQ Tune software. Signal for the automated optimization procedure was provided by ionization of 1 mg/mL RNase A in 70% ACN (+ 0.1% FA, 0.025% TFA), which was pumped directly into the electrospray source using the instrument-integrated syringe pump at 50  $\mu$ L/min. Ionization was performed using a potential of +2.5 kV for RNase A & B and +2.0 kV for the *IdeS*-digested mAb.

For nanoLC-MS detector optimization, the same RNase A solution was loaded into a 25 cm x 100  $\mu$ m reservoir capillary, which was then linked to a hollow needle emitter on one end and the Thermo Ultimate 3000 chromatograph on the other. The flow was set at 100 nL/min, and automated optimization of the ion optics and gain settings for the nanoLC-MS analyses performed using LTQ Tune.

### ***IdeS Protease Digestion of the NIST mAb Standard***

The procedure used to cleave the humanized IgG1 $\kappa$  antibody standard (NIST mAb SRM 8671) using the Immunoglobulin-degrading enzyme from *Streptococcus pyogenes* (*IdeS*) was based upon the protocol given by the manufacturer<sup>26</sup>. In brief: the lyophilized protease was first reconstituted in 75  $\mu$ L of pH 7.0 phosphate buffered saline to a final concentration of 66.7 units/ $\mu$ L. Next, 7.5  $\mu$ L of this was added to 125  $\mu$ L of a 4 mg/mL mAb solution (in the manufacturer-supplied histidine buffer, 5 mM, pH 6.0). The resulting solution was then incubated in a 37  $^{\circ}$ C water bath for 30 minutes. Finally, the digest was split into 10  $\mu$ L aliquots and stored at -20  $^{\circ}$ C until needed.

## **4.3 Results and Discussion**

### **4.3.1 Broadening Introduced by Hollow Needle Emitter**

The first step in migrating the newly-developed nanoHILIC-fluorescence method to the more universal MS detection method required adaptation of the outlet of the column to a format conducive to electrospray ionization (ESI). Commercial nanoLC-ESI-MS systems are commonly

sold that utilize commercial capillary columns with integrated, nominally zero dead volume (ZDV) connectors that can be screwed into a nebulization apparatus for nanoelectrospray. These instruments generally employ a hollow stainless-steel or glass needle emitter with a length of 5 cm and an average inner diameter of 20  $\mu\text{m}$ <sup>27</sup>. The combination of mixing within the connector and the parabolic flow profile from the hollow emitter can introduce substantial post-column broadening<sup>28</sup>.

The effect of linking a commercially-available hollow needle emitter to a nanoHILIC capillary with a PTFE sleeve was thus investigated. An image of this linkage is provided in Figure 4.2 for clarity. Figure 4.6 provides a direct comparison that was performed by imaging the separation at the end of the HILIC capillary (left) and at the end of the 3-cm hollow emitter (right), using fluorescence microscopy. The resulting chromatograms provide a clear illustration of the broadening one encounters when introducing such a significant post-column void space. Even after trimming both the analytical and emitter capillaries with a diamond cutter and visually confirming the absence of a mixing volume between the two capillaries, the peaks are significantly broader and the resulting signal-to-noise is decreased enormously. The first two major peaks are no longer baseline-resolved and the fine structure of the first peak is lost completely (Figure 4.7), making the case for developing a platform that does not require the use of a hollow needle-emitter.

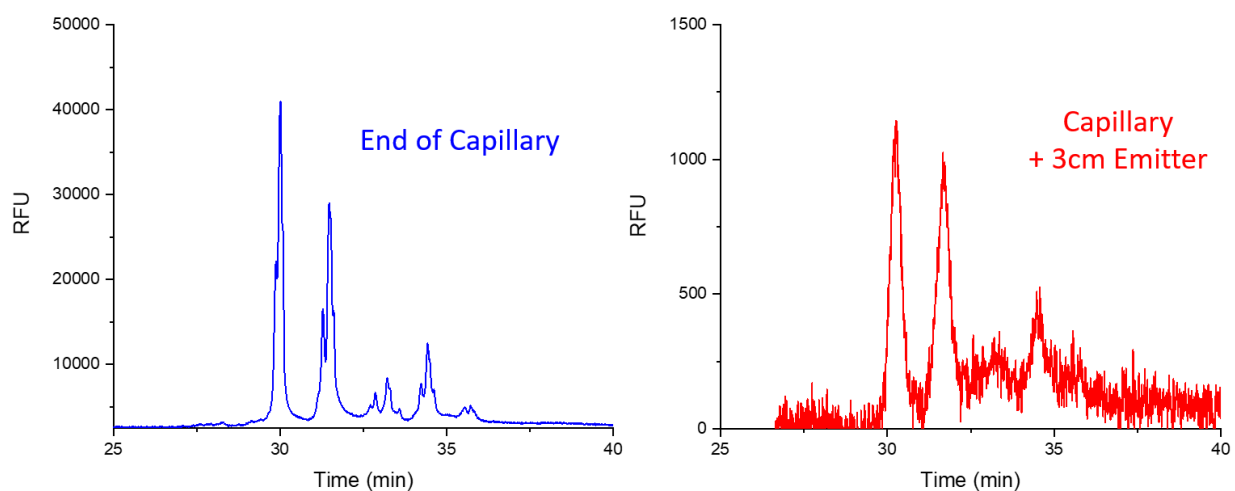


Figure 4.6. Chromatograms from separation of A488-labeled RNase B at the end of a capillary column before (left) and after (right) travelling through a linked needle emitter. Gradient elution was utilized, with 75-60% ACN + 0.1% FA, 0.025% TFA over 30 minutes.

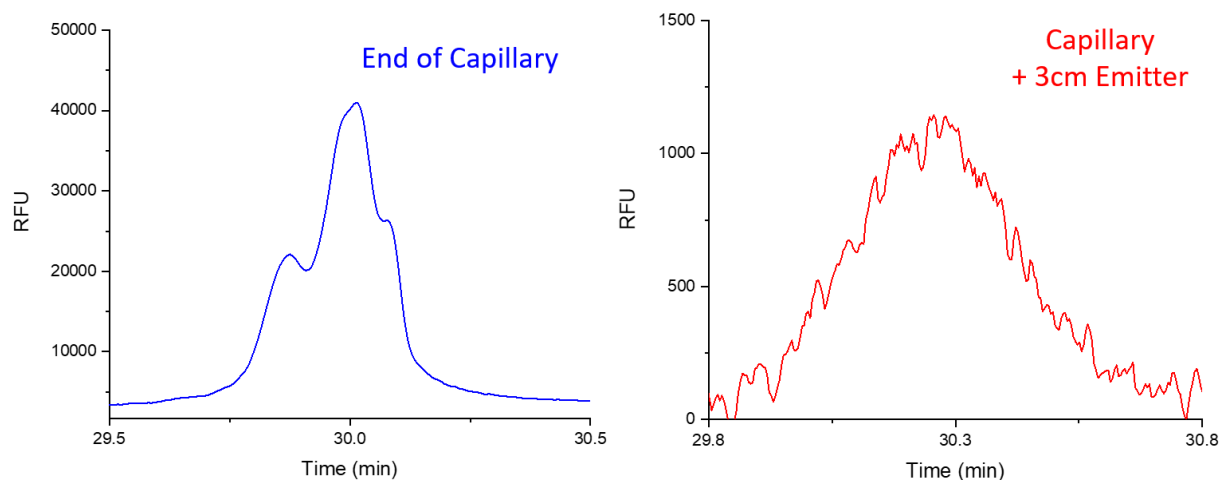


Figure 4.7. A magnified view of the first peak for each of the two chromatograms presented in Figure 4.6

### 4.3.2 Capillary Column with Integrated Emitter

After investigating the post-column broadening introduced by a linked needle emitter, it became clear that the performance of nanoHILIC-MS separations would be severely limited by using such a simple interface between the column and the mass spectrometer. An alternative was sought by the packing of the needle emitter itself, which is designed to eliminate the parabolic flow profile. A key consideration, however, is that the packing of a capillary column plays a significant role in its performance. To reduce packed bed inhomogeneity, standard UHPLC and nanoLC columns are packed under sonication. The effects of packed bed inhomogeneity are generally more pronounced in capillary packing<sup>29</sup>—Figure 4.8 illustrates an extreme example of the void volumes that can be introduced in packing without sonication. Additional void spaces between the particles are common when packing capillaries without sonication<sup>30</sup>, increasing porosity and peak widths, though these are too small to visualize in this scenario.

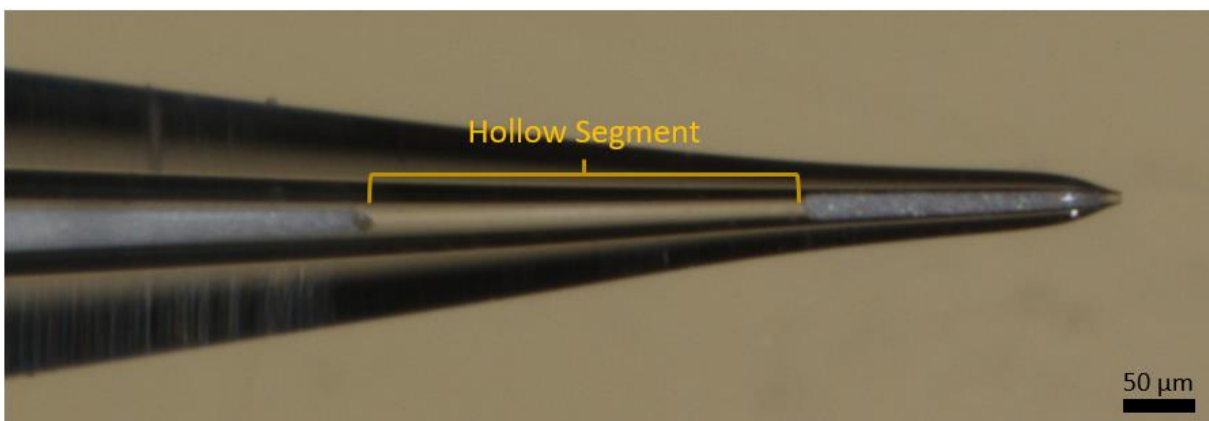


Figure 4.8. Commercial needle emitter packed without sonication

While PTFE- or polyimide-coated capillaries are sturdy enough to withstand the sonication required for packing an efficient capillary column, the sharp, uncoated silica tip of a needle emitter can readily fracture due to the pressure waves produced by the sonicator (Figure 4.9). Wetted silicate glass is particularly susceptible to breakage due to stress corrosion, where the growth rate of a sub-microscopic crack in the silica is accelerated by three or more orders of magnitude in the presence of water<sup>31, 32</sup>. By applying an organosilane monolayer, the surface can be made hydrophobic, alleviating this concern and thus strengthening the glass.

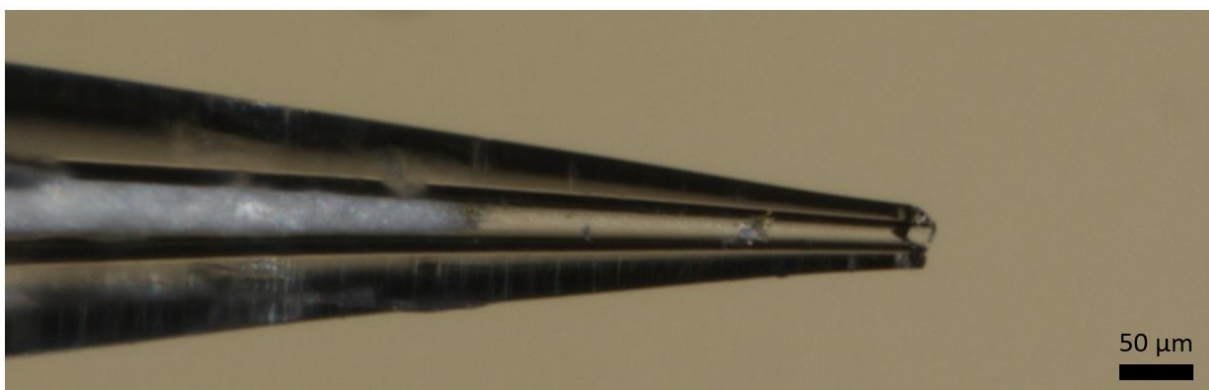


Figure 4.9. Unmodified commercial needle emitter, with the tip fractured during sonication

A simple gas-phase silane reaction was performed to give the needle emitters the desired hydrophobic coating, following a procedure described by Kasapgil<sup>33</sup> (adapted for coating needle emitters through use of the apparatus illustrated in Figure 4.3). After coating the surface of the

emitters with a polysiloxane monolayer, they became rugged enough to withstand the sonication required to produce a well-ordered packed bed without breaking (Figure 4.10).

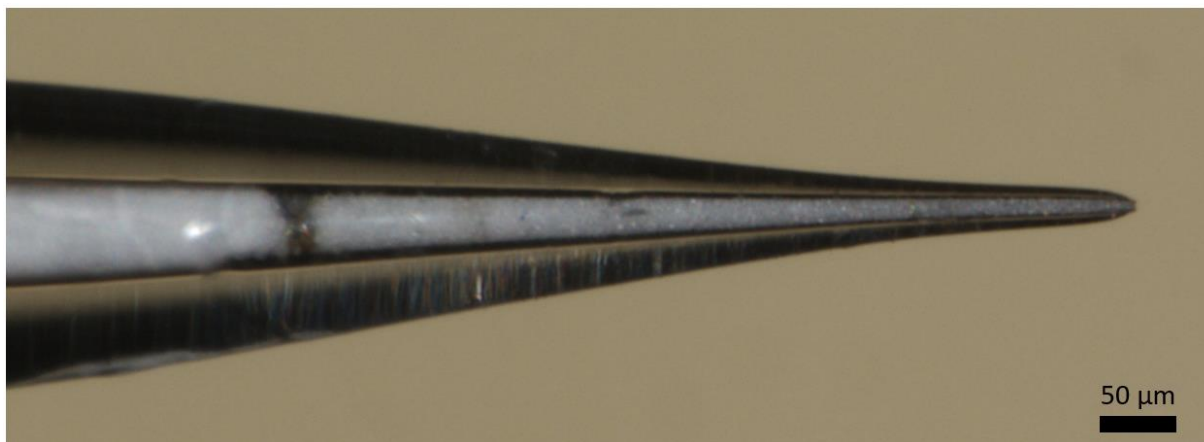


Figure 4.10. Silanized needle emitter with a 1 mm frit composed of PHMAAm-coated SPP, and a packed bed of PAAm-coated nonporous particles. The visible gap is a result of constriction of the packed bed upon drying, resolved by rehydration of the packed bed or avoiding dehydration altogether. The tip is intact.

### 4.3.3 nanoHILIC-MS Glycoprotein Separations

Utilizing a packed needle emitter as the nanoLC column enabled greatly improved resolution of the intact glycoforms of RNase B and its aglycosylated counterpart RNase A (Figure 4.11) with on-column masses of 1.2 and 0.2 ng, respectively. The sensitivity of the optimized nanoHILIC method provides the means to detect and identify multiple minority species present in concentrations less than 1% that of the total protein sample, i.e. at sub-femtomole levels. While RNase B was chosen as a model glycoprotein largely due to its relative simplicity—there are only five major glycoforms present—the resolution provided by this nanoHILIC-MS platform enables detection of no fewer than twelve unique species in the sample.



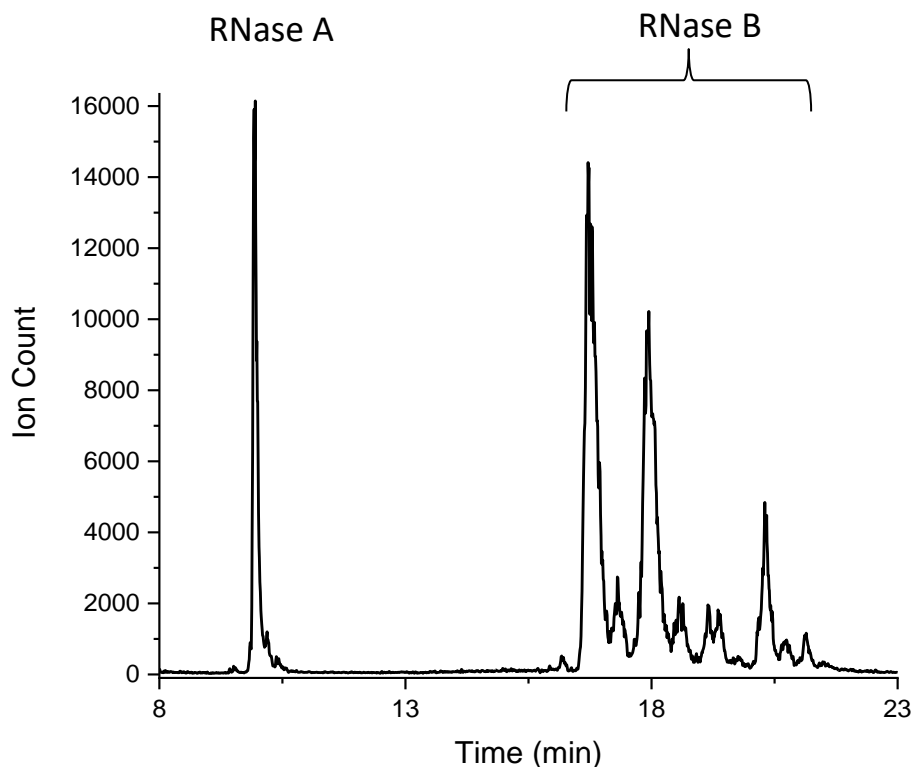


Figure 4.11. Base peak chromatogram for nanoHILIC-MS separation of intact, unlabeled RNase A and RNase B glycoforms using a lab-made capillary column. A gradient of 75-65% ACN + 0.1% FA, 0.025% TFA is run over 30 minutes.

After realizing success with the separation of the model glycoprotein, the next step was to assess the suitability of the nanoHILIC-MS platform for use in characterizing the glycosylation profile of a monoclonal antibody (mAb) standard. The NIST mAb standard was chosen for this purpose, which has been thoroughly characterized through inter-laboratory “round robin” investigations<sup>34</sup>.

The NIST mAb can be rapidly digested enzymatically to release the 25 kDa Fc fragment, which contains the glycans<sup>35</sup>. Separation of the many glycoforms of the Fc fragment of the NIST mAb required an increased concentration of ACN in the mobile phase, as it is not as hydrophilic as the model glycoprotein RNase B. This made the need for the improved sample diluent (discussed in Chapter 3) all the more important; the Fc fragments would not stack at the head of the column using the typical 75% ACN sample solvent composition and without proper on-column focusing, nanoLC separation of such a complex analyte would simply be impossible.

The rapid *IdeS* digest used in the preparation of the NIST mAb sample served two purposes. First, it decreased the mass of the analyte by nearly an order of magnitude—the reported mass for an intact IgG1 protein is approximately 150 kDa<sup>36</sup>, whereas the mass of an Fc fragment with the attached glycan is on the order of 25 kDa<sup>37</sup>. Secondly, digestion made the glycan more accessible; in the intact protein the glycan is sandwiched between the two linked Fc regions of the homodimer but after digestion the glycan is freely accessible. Structures for an intact IgG1 and the G1F-glycosylated Fc fragment were obtained from literature<sup>38, 39</sup> and are presented in Figure 4.12 and Figure 4.13 to illustrate the steric hindrance introduced by the intact protein. The two Fc fragments for the intact, homodimeric IgG1 effectively act as a cage, protecting the glycan from strong interactions with the stationary phase.

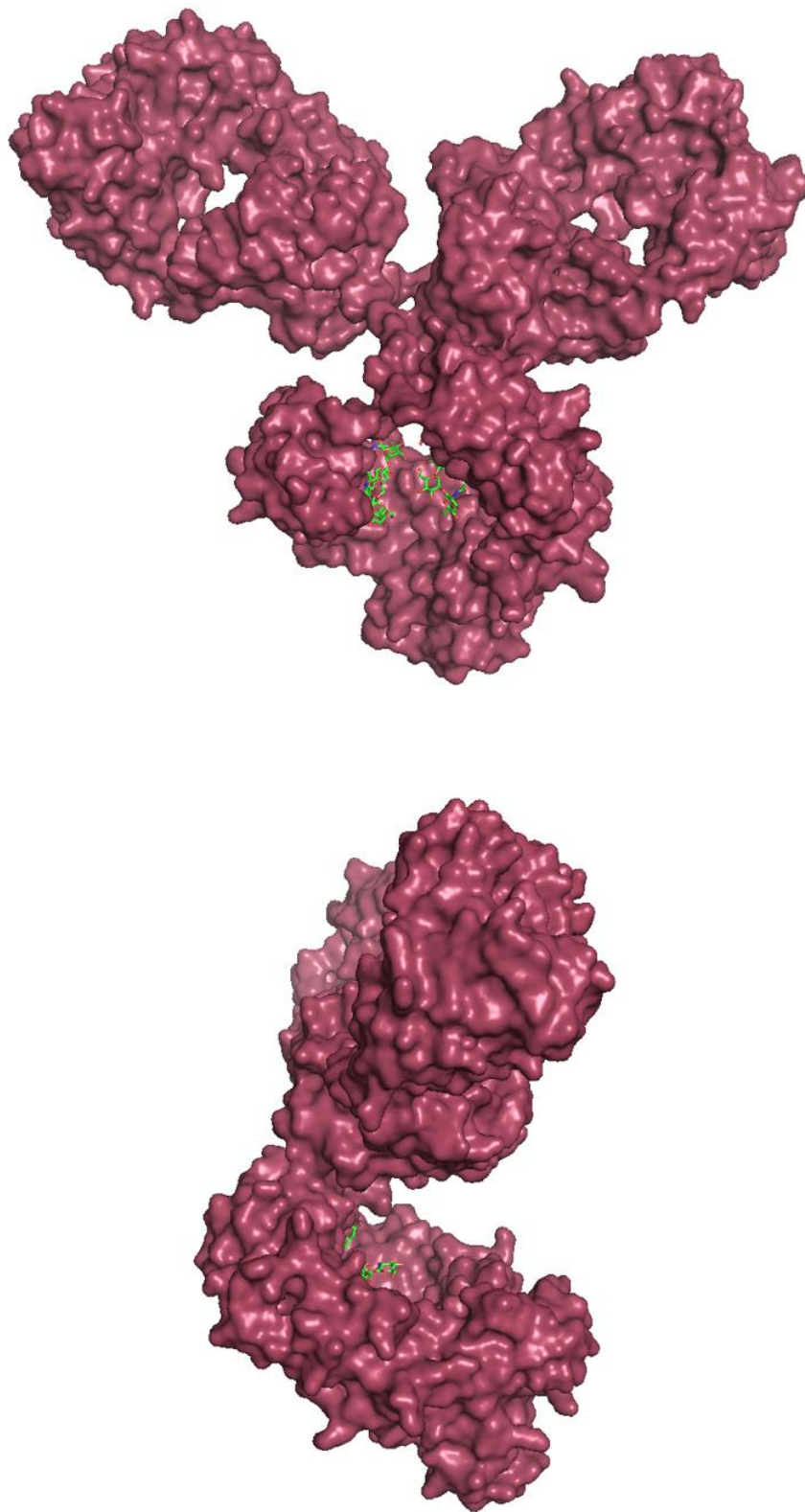


Figure 4.12. Models of an intact IgG1 glycoprotein based on X-ray crystallography data<sup>39</sup>, generated with a “head on” perspective (top) and rotated 90° about the y-axis (bottom)

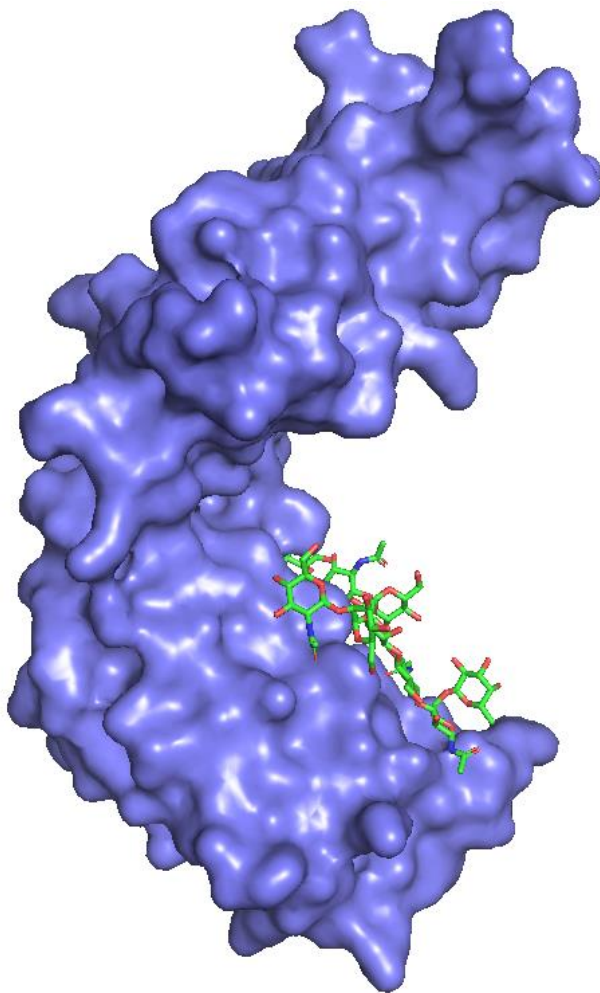


Figure 4.13. Model of the G1F glycan-bearing Fc fragment from an *IdeS* digestion of the NIST mAb<sup>38</sup>, based on X-ray crystallography data. Scale is 2x that of Figure 4.12

After a 30-minute digestion step was performed using *IdeS* to break up the Fab and Fc chains of the mAb, nanoHILIC separation of the various glycoforms of the protein's Fc fragment was performed with the results presented in Figure 4.14. The chromatogram on the left, which is for the capillary, reveals many more glycoforms. This compares very favorably with the separation achieved using traditional HILIC UHPLC-MS methods and a commercial column, as shown in the same figure. Strikingly, the nano-scale separation employed less than 0.05% the sample mass required for the standard UHPLC method (2.5 ng vs. 6  $\mu$ g) but still provided a significantly improved signal to background.

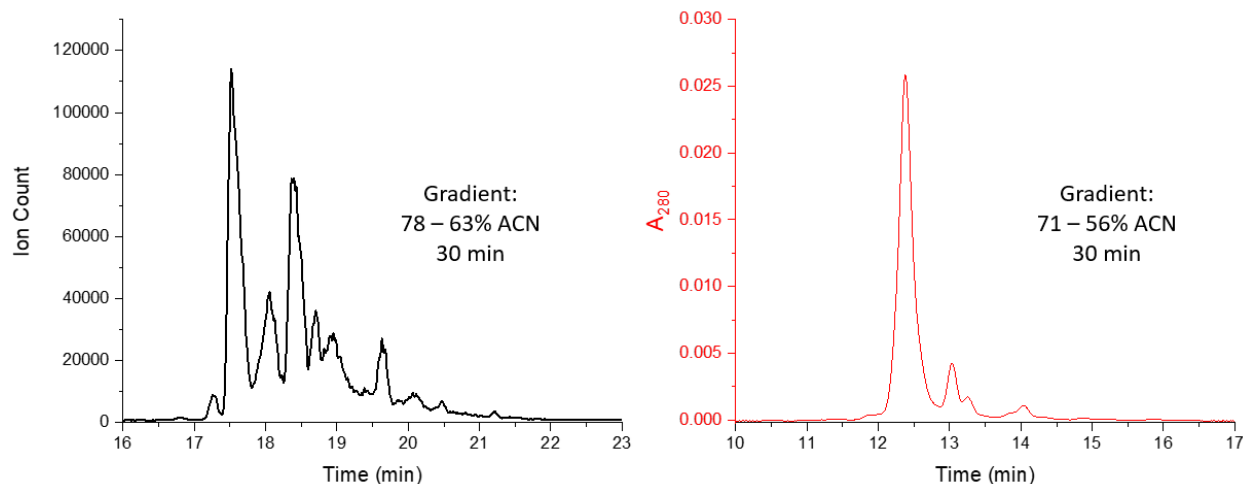


Figure 4.14. A comparison of base peak chromatograms for the NIST mAb Fc fragment, obtained using the nanoHILIC-MS platform (left) and using a commercial HILIC UHPLC column (right)

#### 4.3.4 Analyte Identification

As discussed above, a key advantage of MS-based detection is the ability to identify analytes eluting off the column based on their respective masses. Powerful software tools exist to assist in the deconvolution of the charge ladders produced by the multiply-charged protein ions, predicting the mass of the molecular ion without the need for manual calculations<sup>40</sup>. Using LC at the front end of the mass spectrometer instead of simply introducing the complex mixture to the inlet of mass spectrometer provided more simple mass spectra (Figure 4.15), amenable to the automated deconvolution methods utilized in the identification of multiple constituents of the NIST mAb sample (Figure 4.16). Further, separating the sample mixture with LC prior to mass spectrometry can help prevent false identifications caused by sample contamination or excipients within the sample matrix<sup>41</sup>.

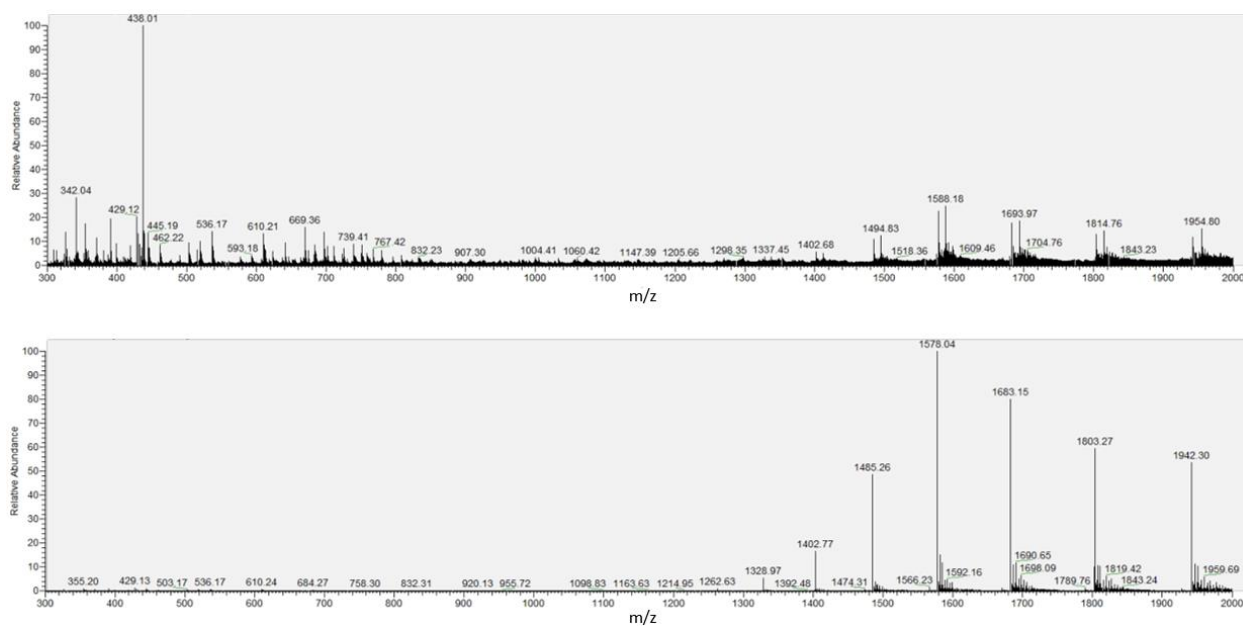


Figure 4.15. Mass spectra obtained over the entire 30-minute gradient for the NIST mAb (top) vs that obtained when limiting the time window to that of the peak for the G1F glycoform (bottom)

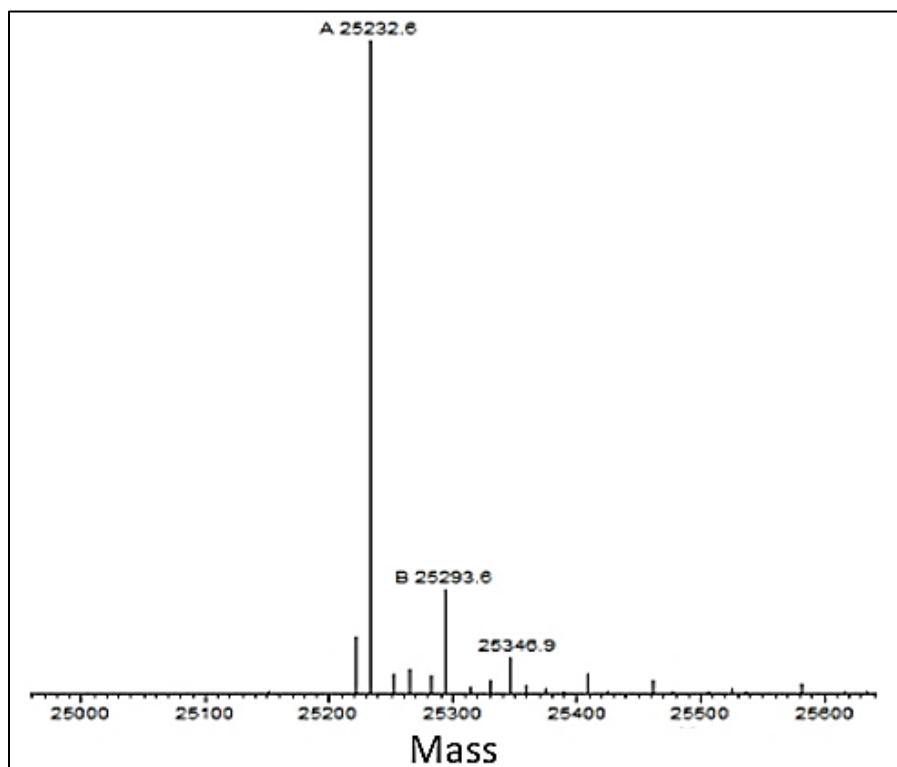


Figure 4.16. Deconvoluted mass spectrum for the G1F peak, generated using MagTran software to process the raw mass spectrum from Figure 4.15

The superior signal-to-background provided by nanoHILIC combined with the mass information gathered using mass spectrometry-based detection enabled the positive identification of 28 glycoforms of the NIST mAb standard (Figure 4.17, Table 4.1), including the pharmaceutically-relevant Man5 glycoform present at sub-femtomole levels<sup>34, 42</sup> (Figure 4.18). Multiple additional species were detected, but the species corresponding to their intact masses have yet to be identified. While a staggering amount of data was generated by a round-robin interlaboratory study of the glycoforms in the NIST mAb standard, including the identification of over 100 species, the glycan or glycoprotein mass information is not contained within this trove of information<sup>34</sup>. Reference masses used for peak identification were found in various other papers<sup>37, 43, 44</sup>.

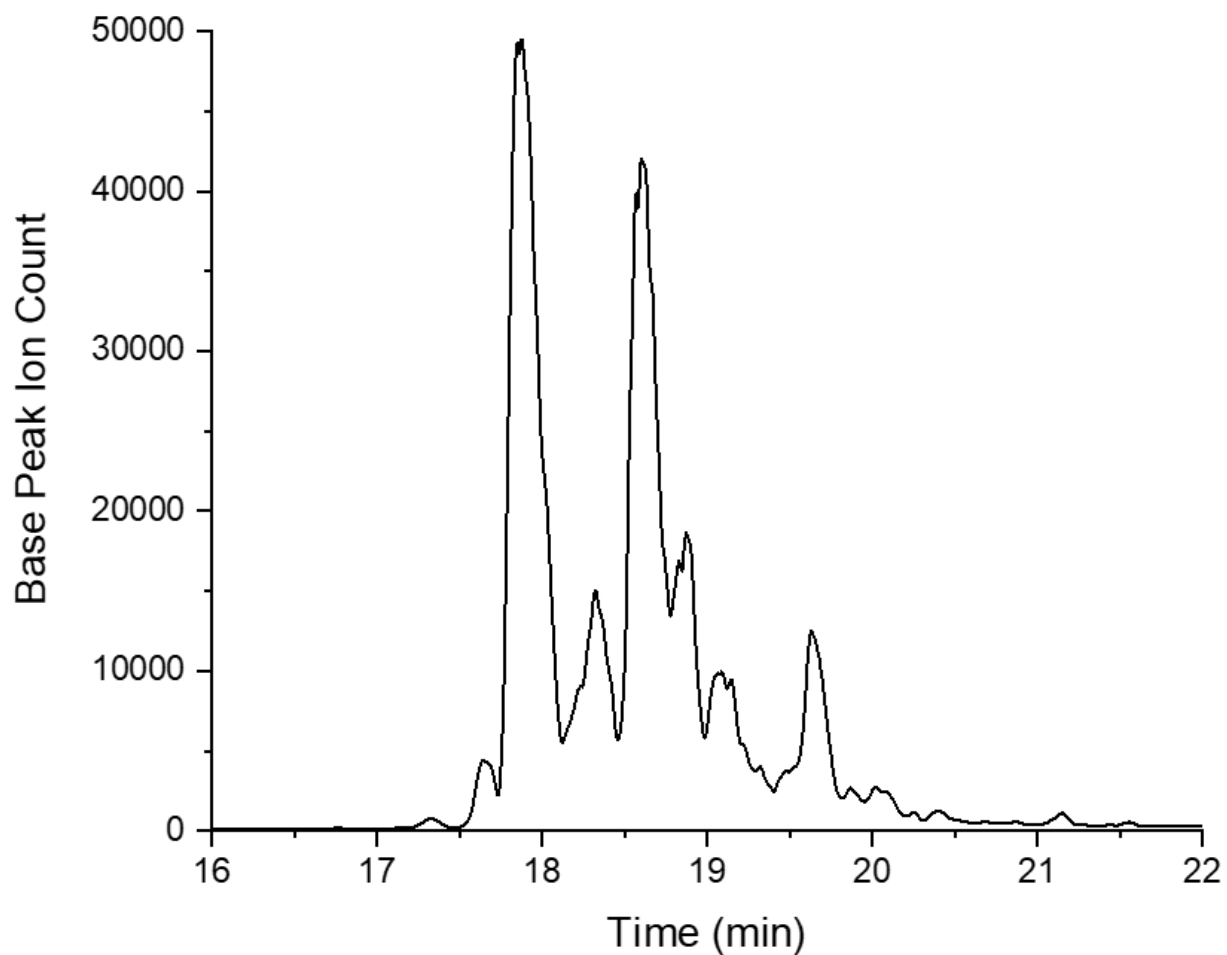


Figure 4.17. Chromatogram from nanoHILIC-MS separation of the *IdeS*-digested NIST mAb standard. Mass-confirmed glycoform identities are presented in Table 4.1. A gradient of 78-63% ACN + 0.1% FA, 0.025% TFA was run over 30 minutes.



Table 4.1. Glycovariants identified in the NIST mAb standard with retention time corresponding to chromatogram in Figure 4.17. Expected mass calculated based upon observed m/z for main (G0F) glycoform. Structure and percent composition based upon results from a NIST interlaboratory investigation<sup>34</sup>.

Component Name	Glycan Structure	Retention Time (min)	%	Observed m/z	Calculated Mass (Da)	Expected Mass (Da)
G0-N		17.27	0.43	1556.1	24898	24889
Man3F		17.28	0.14	1552.4	24838	24832
G0F-N		17.56	2.13	1565.2	25043	25035
G0		17.66	0.19	1568.8	25101	25092
G0F		17.83	39.10	1577.4	25238	25238
Man5		18.14	0.73	1563.7	25019	25010
G0F + C-terminal Lysine		18.21	--	1586.1	25377	25366
G1F-N		18.47	2.20	1575.4	25207	25197
G1F		18.59	38.37	1588.2	25411	25400

Table 4.1 continued

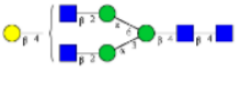
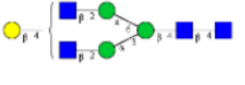
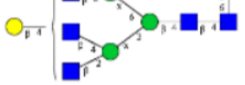

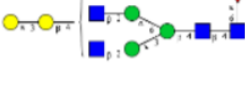
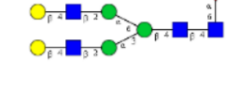

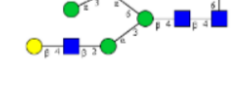
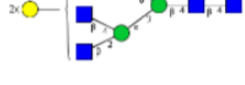
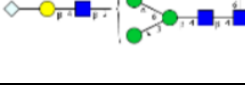
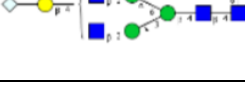
G1F (isomer)		18.88	--	1588.2	25410	25400
G1F + C-terminal Lysine		18.94	--	1596.2	25539	25528
G1F+N		19.24	0.51	1600.8	25612	25604
G1F-N+1aGal		19.42	0.89	1585.5	25368	25359
G1F+1aGal		19.47	1.61	1598.2	25571	25563
G2F		19.64	7.51	1598.3	25573	25563
Man5G1 hybrid		19.79	0.23	1586.4	25382	25375
Man5G1F hybrid		19.89	0.18	1594.6	25514	25521
G2F+N		19.93	0.24	1611.0	25776	25766
G1FS-N (NeuGc)		19.96	1.01	1594.4	25511	25504
G1FS (NeuGc)		20.21	0.35	1607.4	25718	25708

Table 4.1 continued

Man7		20.22	0.55	1583.8	25341	25334
G2F+1aGal		20.39	1.80	1608.5	25736	25725
G3F		20.74	0.32	1621.3	25941	25928
G1FS (NeuGc)		20.82	0.35	1606.5	25704	25708
G2FS2 (NeuGc)		20.87	0.45	1617.0	25872	25870
G2F+2aGal		21.15	0.89	1618.6	25897	25887
G2F+N+2aGal		21.49	0.11	1631.4	26103	26090
G2FS-1aGal (NeuGc)		21.55	0.46	1627.5	26040	26032

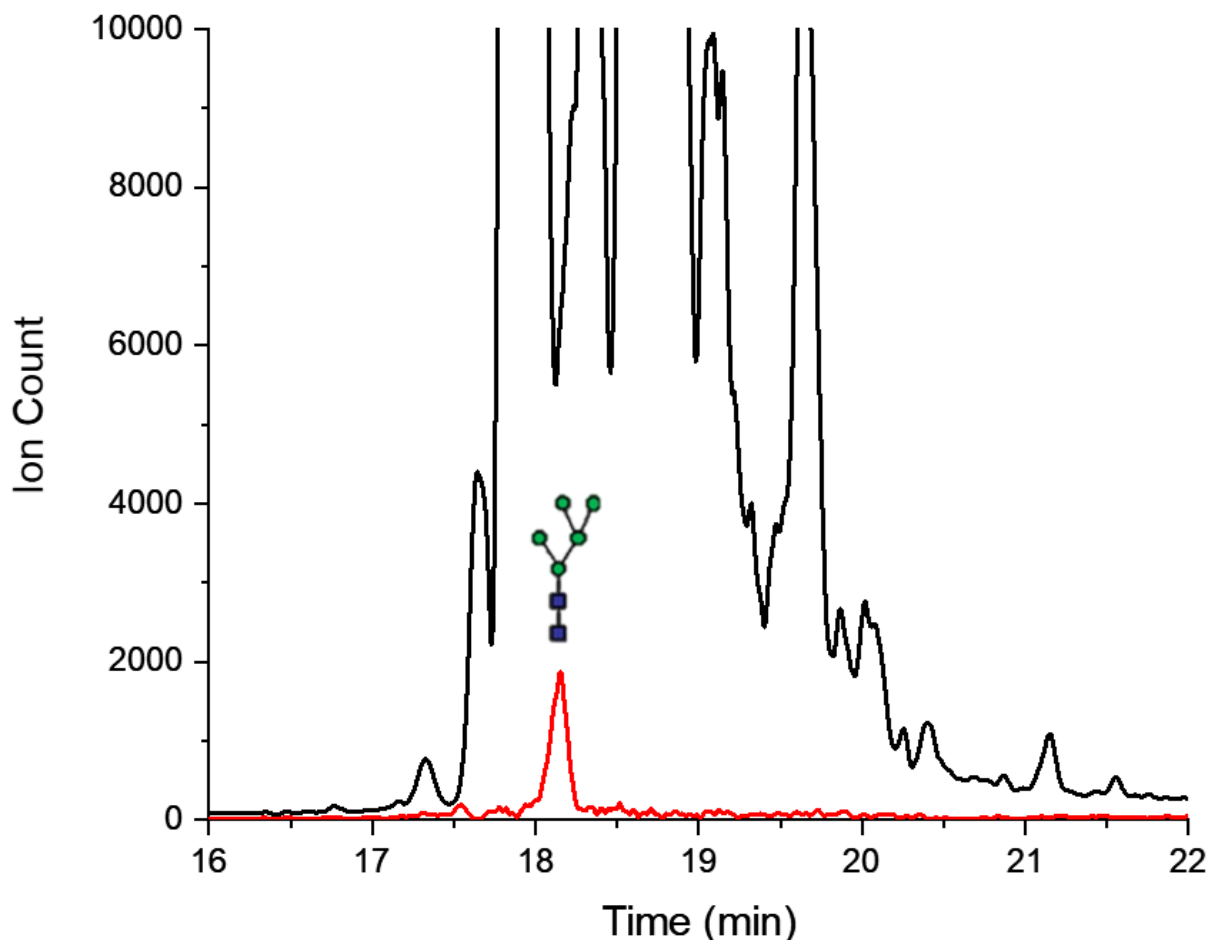


Figure 4.18. Extracted ion chromatogram for the Man5 glycoform (red) present the NIST mAb standard set against the base-peak chromatogram (black) from the same analysis

#### 4.4 Conclusion

A nanoHILIC-MS platform was developed, enabling baseline separation of the five major glycoforms plus isomers of the model protein RNase B, and 28 glycoforms of the Fc fragment of the NIST mAb standard. Using mass spectrometry-based detection methods, the glycovariants were detected and identified based on comparison of their observed masses with those presented in previous literature. Clearly the tools exist to apply this to a more pharmaceutically-relevant sample such as a therapeutic mAb or antibody-drug conjugate. This should be a more straightforward task than identifying the constituents of the complex NIST mAb sample, as the glycan profile for a drug substance has fewer glycoforms by necessity. It may also be possible to avoid the 30-minute *IdeS* protease digestion step utilized in this analysis through the rational

design and development of a further-refined polymer brush layer, which would increase the efficacy of this powerful method to an even greater level.

#### 4.5 References

1. Liu, Q.; Cobb, J. S.; Johnson, J. L.; Wang, Q.; Agar, J. N., Performance Comparisons of Nano-LC Systems, Electrospray Sources and LC-MS-MS Platforms. *Journal of Chromatographic Science* **2014**, 52 (2), 120-127.
2. Lehmann, W. D., *Protein phosphorylation analysis by electrospray mass spectrometry a guide to concepts and practice*. RSC Pub.: Cambridge, 2010.
3. Juraschek, R.; Dülcks, T.; Karas, M., Nanoelectrospray—More than just a minimized-flow electrospray ionization source. *Journal of the American Society for Mass Spectrometry* **1999**, 10 (4), 300-308.
4. Kiontke, A.; Oliveira-Birkmeier, A.; Opitz, A.; Birkemeyer, C., Electrospray Ionization Efficiency Is Dependent on Different Molecular Descriptors with Respect to Solvent pH and Instrumental Configuration. *PLOS ONE* **2016**, 11 (12), e0167502.
5. Olumee, Z.; Callahan, J. H.; Vertes, A., Droplet Dynamics Changes in Electrostatic Sprays of Methanol–Water Mixtures. *The Journal of Physical Chemistry A* **1998**, 102 (46), 9154-9160.
6. Marginean, I.; Tang, K.; Smith, R. D.; Kelly, R. T., Picoelectrospray Ionization Mass Spectrometry Using Narrow-Bore Chemically Etched Emitters. *Journal of The American Society for Mass Spectrometry* **2014**, 25 (1), 30-36.
7. Gargano, A. F. G.; Roca, L. S.; Fellers, R. T.; Bocxe, M.; Domínguez-Vega, E.; Somsen, G. W., Capillary HILIC-MS: A New Tool for Sensitive Top-Down Proteomics. *Analytical Chemistry* **2018**, 90 (11), acs.analchem.8b00382-acs.analchem.8b00382.
8. Jung, M. C. Major Sources of Post-column Peak Broadening in nanoLC. <https://www.waters.com/webassets/cms/library/docs/720006526en.pdf> (accessed March 20, 2020).
9. Wilson, S. R.; Vehus, T.; Berg, H. S.; Lundanes, E., Nano-LC in proteomics: recent advances and approaches. *Bioanalysis* **2015**, 7 (14), 1799-1815.
10. Vanderlinden, K.; Broeckhoven, K.; Vanderheyden, Y.; Desmet, G., Effect of pre- and post-column band broadening on the performance of high-speed chromatography columns under isocratic and gradient conditions. **2016**, 1442, 73-82.
11. Davey, A.; Drazin, P., The stability of Poiseuille flow in a pipe. *Journal of Fluid Mechanics* **1969**, 36 (2), 209-218.

12. Kano, T., Density Oscillators. In *Pattern Formations and Oscillatory Phenomena*, Elsevier: 2013; pp 119-163.
13. Aris, R., On the dispersion of a solute in a fluid flowing through a tube. *Proceedings of the Royal Society of London. Series A. Mathematical and Physical Sciences* **1956**, 235 (1200), 67-77.
14. Gritti, F.; Guiochon, G., On the minimization of the band-broadening contributions of a modern, very high pressure liquid chromatograph. **2011**, 1218 (29), 4632-4648.
15. Krouglova, T.; Vercammen, J.; Engelborghs, Y., Correct Diffusion Coefficients of Proteins in Fluorescence Correlation Spectroscopy. Application to Tubulin Oligomers Induced by Mg<sup>2+</sup> and Paclitaxel. **2004**, 87 (4), 2635-2646.
16. Einstein, A., Zur Elektrodynamik bewegter Körper. *Annalen der Physik* **1905**, 322 (10), 891-921.
17. Edward, J. T., Molecular volumes and the Stokes-Einstein equation. *Journal of Chemical Education* **1970**, 47 (4), 261.
18. Snyder, L. R., *Introduction to modern liquid chromatography*. 3rd ed. / John W. Dolan. ed.; Hoboken, New Jersey : Wiley: 2010.
19. Gresho, P. M.; Sani, R. L., On pressure boundary conditions for the incompressible Navier-Stokes equations. *International Journal for Numerical Methods in Fluids* **1987**, 7 (10), 1111-1145.
20. Thompson, J. W.; Kaiser, T. J.; Jorgenson, J. W., Viscosity measurements of methanol-water and acetonitrile-water mixtures at pressures up to 3500 bar using a novel capillary time-of-flight viscometer. *Journal of Chromatography A* **2006**, 1134 (1-2), 201-209.
21. Nishimura, J.; Oka, S., The steady flow of a viscous fluid through a tapered tube. *Journal of the Physical Society of Japan* **1965**, 20 (3), 449-453.
22. Sundquist, A., Dynamic line integral convolution for visualizing streamline evolution. *IEEE Transactions on Visualization and Computer Graphics* **2003**, 9 (3), 273-282.
23. Zhang, Z.; Marshall, A. G., A universal algorithm for fast and automated charge state deconvolution of electrospray mass-to-charge ratio spectra. *Journal of the American Society for Mass Spectrometry* **1998**, 9 (3), 225-233.
24. Michalske, T. A.; Freiman, S. W., A Molecular Mechanism for Stress Corrosion in Vitreous Silica. *Journal of the American Ceramic Society* **1983**, 66 (4), 284-288.
25. Gaspar, A.; Piyasena, M. E.; Gomez, F. A., Fabrication of fritless chromatographic microchips packed with conventional reversed-phase silica particles. *Analytical Chemistry* **2007**, 79 (20), 7906-7909.

26. FabRICATOR Instructions-Jan 2020. <https://www.genovis.com/wp-content/uploads/instructions-fabricator-jan-2020.pdf> (accessed March 15, 2020).
27. Nanospray Flex Series – Ion Source – User Guide (Revision B). <https://assets.thermofisher.com/TFS-Assets/CMD/manuals/Man-60053-97127-Nanospray-Flex-User-Man6005397127-EN.pdf> (accessed March 14, 2020).
28. Noga, M.; Sucharski, F.; Suder, P.; Silberring, J., A practical guide to nano-LC troubleshooting. **2007**, *30* (14), 2179-2189.
29. Angus, P. D. A.; Demarest, C. W.; Catalano, T.; Stobaugh, J. F., Aspects of column fabrication for packed capillary electrochromatography. **2000**, *887* (1-2), 347-365.
30. Ehlert, S.; Rösler, T.; Tallarek, U., Packing density of slurry-packed capillaries at low aspect ratios. **2008**, *31* (10), 1719-1728.
31. Gy, R., Stress Corrosion of Glass. In *Physical Aspects of Fracture*, Bouchaud, E.; Jeulin, D.; Prioul, C.; Roux, S., Eds. Springer Netherlands: Dordrecht, 2001; pp 305-320.
32. Wiederhorn, S. M.; Bolz, L. H., Stress Corrosion and Static Fatigue of Glass. **1970**, *53* (10), 543-548.
33. Kasapgil, E.; Atici, E. G.; Cicek, R.; Anac, I.; Erbil, H. Y., Superhydrophobic polysiloxane filament growth on non-activated polymer coatings. *RSC advances* **2016**, *6* (78), 74921-74928.

34. Lorna De Leoz, M. A.; Duewer, D. L.; Fung, A.; Liu, L.; Kei Yau, H.; Potter, O.; Staples, G. O.; Furuki, K.; Frenkel, R.; Hu, Y.; Susic, Z.; Zhang, P.; Altmann, F.; Grünwald-Gruber, C.; Shao, C.; Zaia, J.; Evers, W.; Pengelley, S.; Suckau, D.; Wiechmann, A.; Resemann, A.; Jabs, W.; Beck, A.; Froehlich, J. W.; Huang, C.; Li, Y.; Liu, Y.; Sun, S.; Wang, Y.; Seo, Y.; Joo An, H.; Reichardt, N.-C.; Echevarria Ruiz, J.; Archer-Hartmann, S.; Azadi, P.; Bell, L.; Lakos, Z.; An, Y.; Cipollo, J. F.; Pucic-Bakovic, M.; Štambuk, J.; Lauc, G.; Li, X.; George Wang, P.; Bock, A.; Hennig, R.; Rapp, E.; Creskey, M.; Cyr, T. D.; Nakano, M.; Sugiyama, T.; Amy Leung, P.-K.; Link-Lenczowski aa, P.; Jaworek aa, J.; Yang ab, S.; Zhang ab, H.; Kelly ac, T.; Klapoetke ac, S.; Cao ac, R.; Young Kim ad, J.; Kyoung Lee ad, H.; Yeon Lee ad, J.; Shin Yoo ad, J.; Kim ae, S.-R.; Suh ae, S.-K.; de Haan af, N.; Falck af, D.; M Lageveen-Kammeijer af, G. S.; Wuhrer af, M.; Emery ag, R. J.; Kozak ag, R. P.; Phing Liew ag, L.; Royle ag, L.; Urbanowicz ag, P. A.; Packer ah, N. H.; Song ah, X.; Everest-Dass ah, A.; Lattová ai, E.; Cajic aj, S.; Alagesan ak, K.; Kolarich ak, D.; Kasali al, T.; Lindo al, V.; Chen am, Y.; Goswami am, K.; Gau an, B.; Amunugama ao, R.; Jones ao, R.; Stroop ap, C. J. M.; Kato aq, K.; Yagi ar, H.; Kondo ar, S.; Yuen at, C. T.; Harazono au, A.; Shi av, X.; Magnelli av, P. E.; Kasper aw, B. T.; Mahal aw, L.; Harvey ax, D. J.; ay, F.; Rudd ay, P. M.; Saldova ay, R.; Hecht az, E. S.; Muddiman az, D. C.; Kang ba, J.; Bhoskar bb, P.; Menard bb, D.; Saati bb, A.; Merle bc, C.; Mast bd, S.; Tep bd, S.; Truong bd, J.; Nishikaze be, T.; Sekiya be, S.; Shafer bf, A.; Funaoka bg, S.; Toyoda bg, M.; de Vreugd bh, P.; Caron bi, C.; Pradhan bi, P.; Chiang Tan bi, N.; Mechref bj, Y.; Patil bk, S.; Rohrer bk, J. S.; Chakrabarti bl, R.; Dadke bl, D.; Lahori bl, M.; Zou bm, C.; Cairo bm, C.; Reiz bm, B.; Whittal bm, R. M.; Lebrilla bn, C. B.; Wu bn, L.; Guttman bo, A.; Szigeti bo, M.; Kremkow bp, B. G.; Lee bp, K. H.; Sihlbom bq, C.; Adamczyk br, B.; Jin br, C.; Karlsson br, N. G.; Örnros br, J.; Larson bs, G.; Nilsson bs, J.; Meyer bt, B.; Wiegandt bt, A.; Komatsu bu, E.; Perreault bu, H.; Bodnar bu, E. D.; Said bv, N.; Francois bv, Y.-N.; Leize-Wagner bv, E.; Maier bw, S.; Zeck bw, A.; R Heck bx, A. J.; Yang bx, Y.; Haselberg by, R.; Qing Yu bz, Y.; Alley bz, W.; Leone ca, J. W.; Yuan ca, H.; Stein, S. E.; Author, C. *NISTmAb Glycosylation Interlaboratory Study Supplementary Information NIST Interlaboratory Study on Glycosylation Analysis of Monoclonal Antibodies: Comparison of Results from Diverse Analytical Methods*.
35. Janin-Bussat, M.-C.; Tonini, L.; Huillet, C.; Colas, O.; Klinguer-Hamour, C.; Corvaia, N.; Beck, A., Cetuximab Fab and Fc N-Glycan Fast Characterization Using IdeS Digestion and Liquid Chromatography Coupled to Electrospray Ionization Mass Spectrometry. In *Glycosylation Engineering of Biopharmaceuticals: Methods and Protocols*, Beck, A., Ed. Humana Press: Totowa, NJ, 2013; pp 93-113.
36. Schiel, J. E.; Tarlov, M. J.; Choquette, S. J. *Report of Investigation: Reference Material 8671*; NIST: 2016; pp 1-16.
37. Faid, V.; Leblanc, Y.; Bihoreau, N.; Chevreux, G., Middle-up analysis of monoclonal antibodies after combined IgD and IdeS hinge proteolysis: Investigation of free sulfhydryls. *Journal of Pharmaceutical and Biomedical Analysis* **2018**, *149*, 541-546.



38. Gallagher, D. T.; Galvin, C. V.; Karageorgos, I., Structure of the Fc fragment of the NIST reference antibody RM8671. *Acta Crystallographica Section F Structural Biology Communications* **2018**, 74 (9), 524-529.
39. Harris, L. J.; Skaletsky, E.; McPherson, A., Crystallographic structure of an intact IgG1 monoclonal antibody 1 Edited by I. A. Wilson. *Journal of Molecular Biology* **1998**, 275 (5), 861-872.
40. Lu, J.; Trnka, M. J.; Roh, S.-H.; Robinson, P. J. J.; Shiau, C.; Fujimori, D. G.; Chiu, W.; Burlingame, A. L.; Guan, S., Improved Peak Detection and Deconvolution of Native Electrospray Mass Spectra from Large Protein Complexes. *Journal of the American Society for Mass Spectrometry* **2015**, 26 (12), 2141-2151.
41. Lehotay, S. J.; Mastovska, K.; Amirav, A.; Fialkov, A. B.; Martos, P. A.; Kok, A. D.; Fernández-Alba, A. R., Identification and confirmation of chemical residues in food by chromatography-mass spectrometry and other techniques. **2008**, 27 (11), 1070-1090.
42. Ryman, J. T.; Meibohm, B., Pharmacokinetics of Monoclonal Antibodies. *CPT: Pharmacometrics & Systems Pharmacology* **2017**, 6 (9), 576-588.
43. Hilliard, M.; Alley, W. R.; Jr; McManus, C. A.; Yu, Y. Q.; Hallinan, S.; Gebler, J.; Rudd, P. M., Glycan characterization of the NIST RM monoclonal antibody using a total analytical solution: From sample preparation to data analysis. *mAbs* **2017**, 9 (8), 1349-1349.
44. Prien, J. M.; Stöckmann, H.; Albrecht, S.; Martin, S. M.; Varatta, M.; Furtado, M.; Hosselet, S.; Wang, M.; Formolo, T.; Rudd, P. M.; Schiel, J. E., Orthogonal Technologies for NISTmAb N-Glycan Structure Elucidation and Quantitation. In *State-of-the-Art and Emerging Technologies for Therapeutic Monoclonal Antibody Characterization Volume 2. Biopharmaceutical Characterization: The NISTmAb Case Study*, American Chemical Society: 2015; Vol. 1201, pp 185-235.

## CHAPTER 5. FUTURE DIRECTIONS

### 5.1 Superficially Porous Particles

The lab-made columns presented earlier in this text all employed non-porous silica nanoparticles, which provide an excellent alternative to fully-porous particles for separation of large molecules in light of the significant *C-term* introduced by porous particles. A middle ground between these particle morphologies is a superficially-porous particle (SPP), which incorporates a non-porous particle core with a “shell” of smaller particles to give it a porous outer layer (illustrated in Figure 1.9). Two advantages are presented by the core-shell particle relative to nonporous particles: greater analyte capacity due to the higher surface area, and lower column backpressure due to the larger overall particle diameter.

Work has begun on testing the performance of SPPs coated with a polymer brush layer, and an improved capacity has already been demonstrated for columns packed with these particles as compared to their non-porous counterparts (Figure 5.1). The analyte capacity increase provided by these SPP columns provides a distinct advantage. Figure 5.1 paints a clear picture that increasing the on-column mass of RNase B quickly introduces asymmetry and peak overlap for columns packed with non-porous particles, while the effect is lessened with the SPPs. Even under conditions where there is no obvious asymmetry to indicate overloading, a correlation between injected mass and peak width has been observed<sup>1</sup>, so it stands to reason that increasing analyte capacity using particles with a greater surface area may yield narrower peaks even under “non-overloading” conditions.

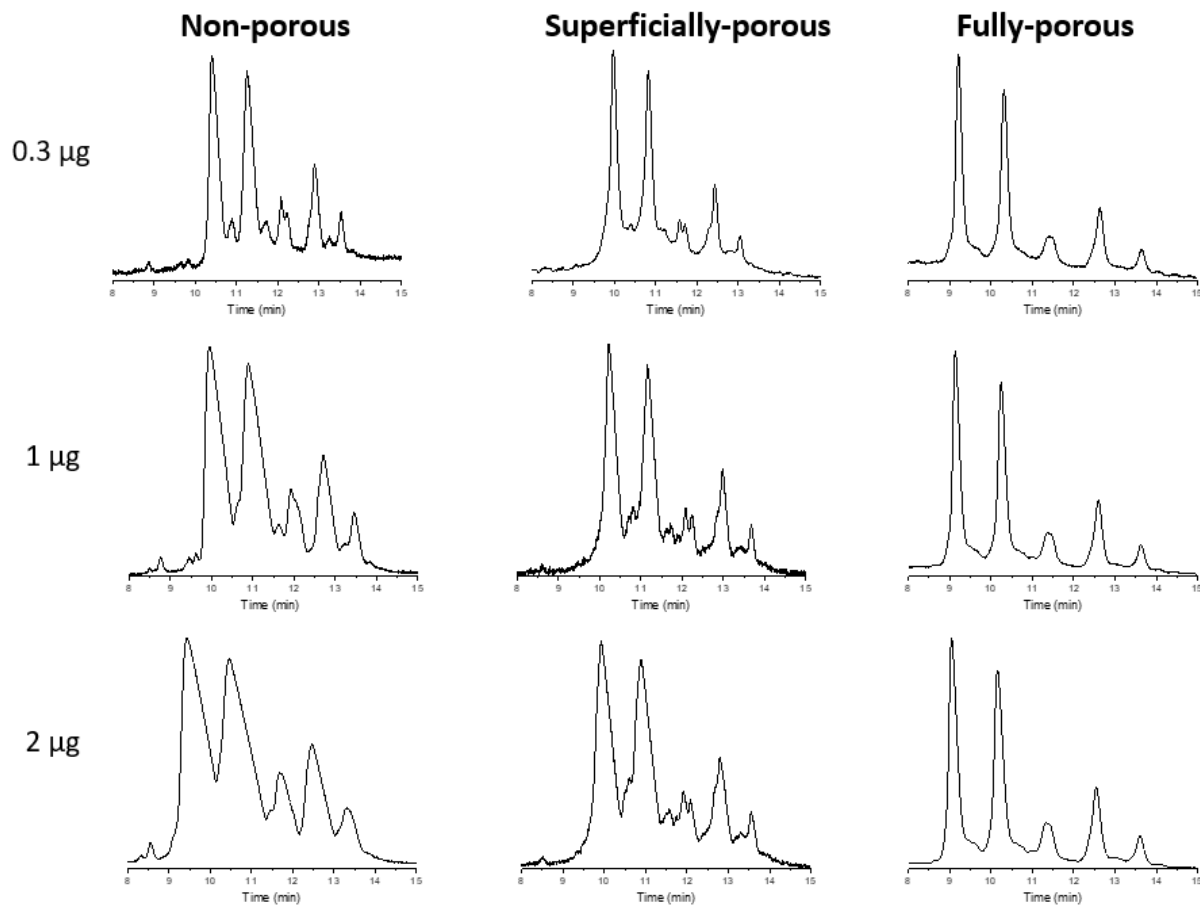


Figure 5.1. Chromatograms from separation of RNase B using columns with varying particle morphology—non-porous (left), superficially-porous (right), and fully-porous (right) with varying analyte mass—0.3  $\mu\text{g}$  (bottom), 1  $\mu\text{g}$  (middle), and 2  $\mu\text{g}$  (top)

Refinement of the brush layer synthesis may further improve capacity; much of the pore space is closed off after applying the polymer layer using current methods. The blockage of the smaller pores can be viewed directly using Scanning Electron Microscopy (SEM), as shown in Figure 5.2 and Figure 5.3. These images are for two different particles, by necessity, but are representative.

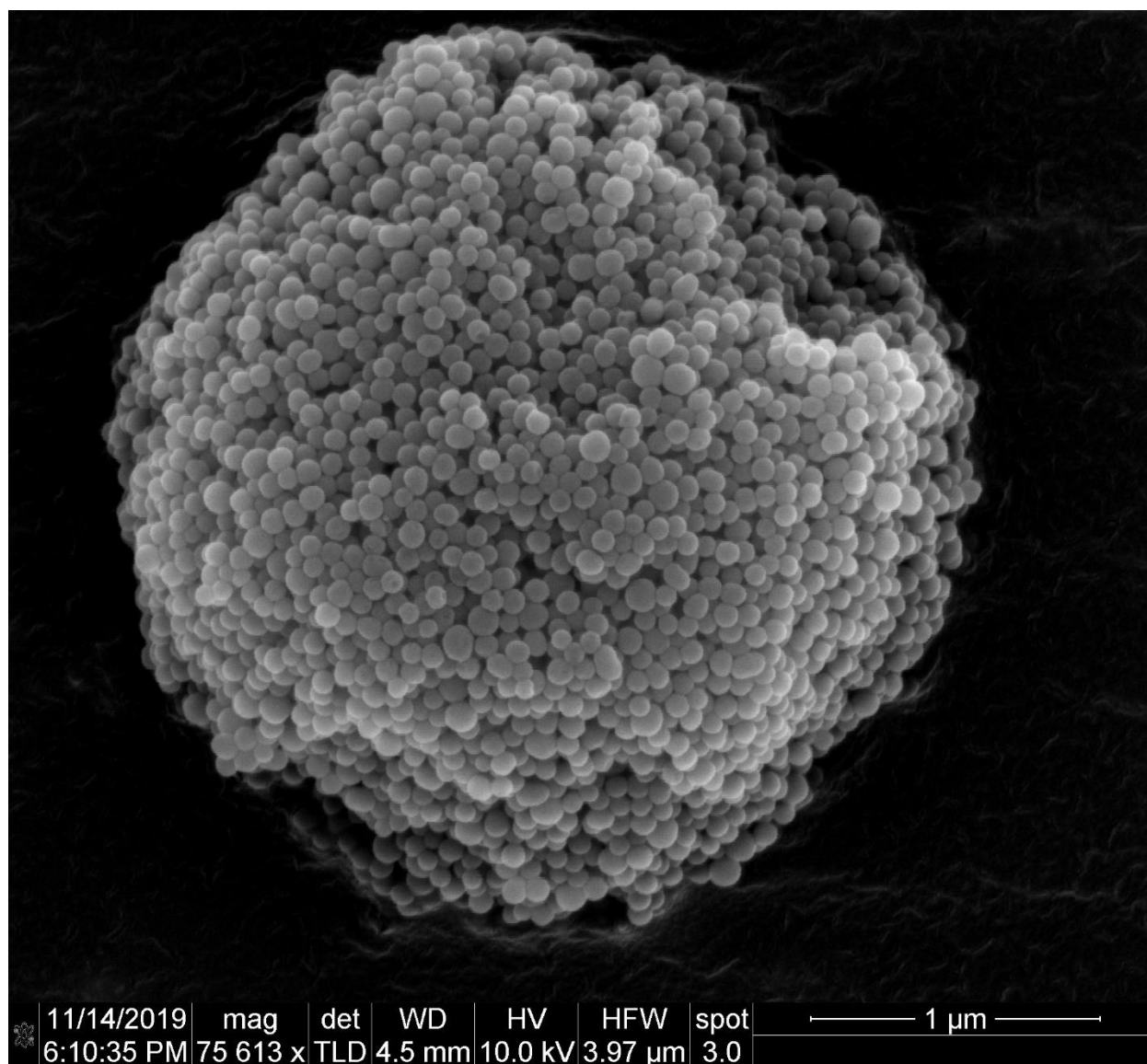


Figure 5.2. SEM micrograph of a superficially-porous particle before polymer modification

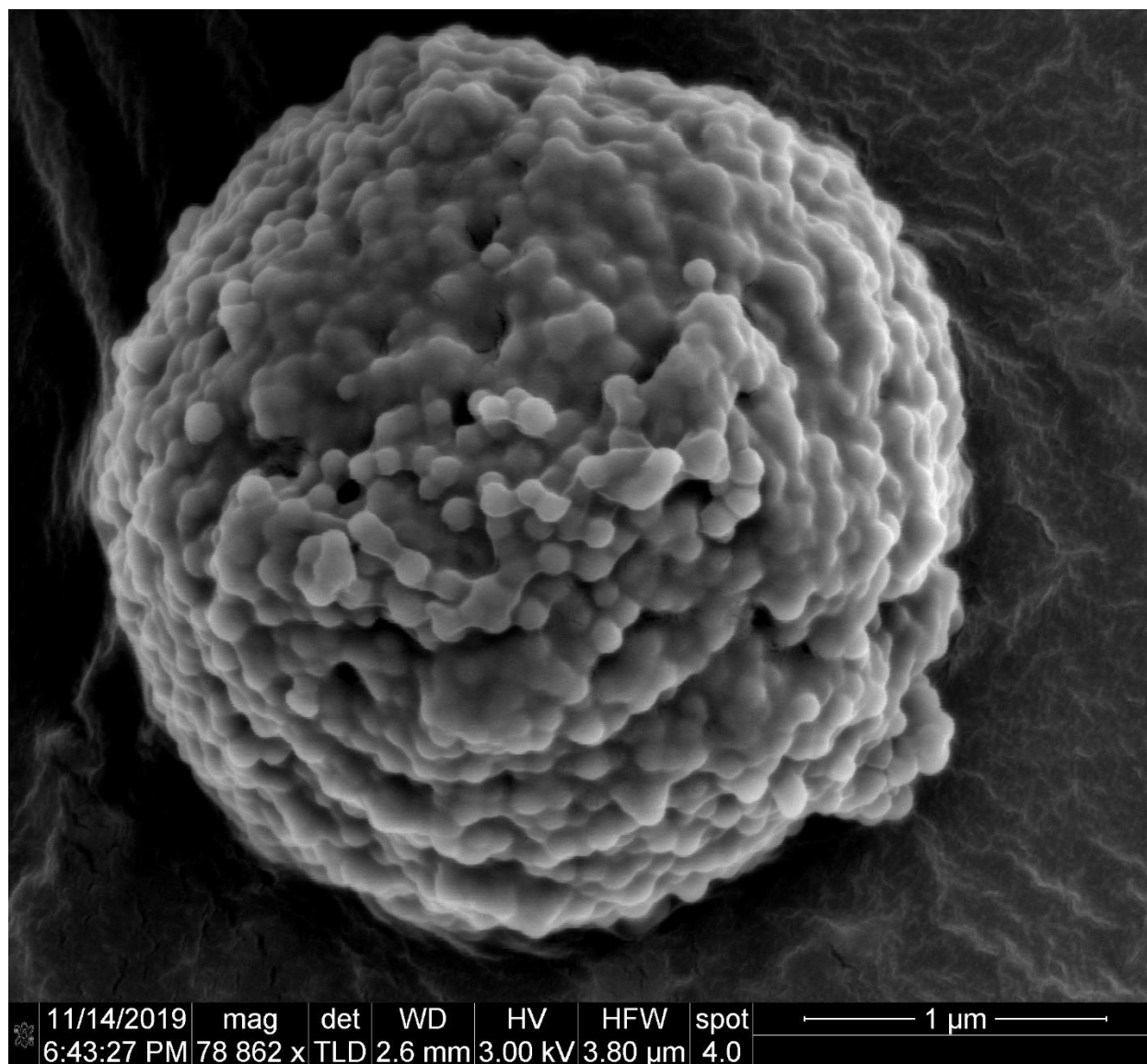


Figure 5.3. SEM micrograph of a superficially-porous particle after coating with a PHMAAm brush layer

## 5.2 Copolymer Bonded Phase

The main drawback of using a polyacrylamide bonded phase is its susceptibility to hydrolysis<sup>2</sup>. This phenomenon is accelerated in acidic conditions<sup>2</sup>, making its capacity for hydrolysis even more of a concern due to the acidic modifiers typically used in LC mobile phases. The addition of a hydroxymethyl group in the monomer, as shown in Figure 5.5, improves stability. The methyl group makes the resulting PHMAAm bonded phase less hydrophilic, therefore it does

not offer the selectivity provided by PAAm brush layers. The lower selectivity is illustrated by the reduced spacing between trendlines in Figure 5.4.

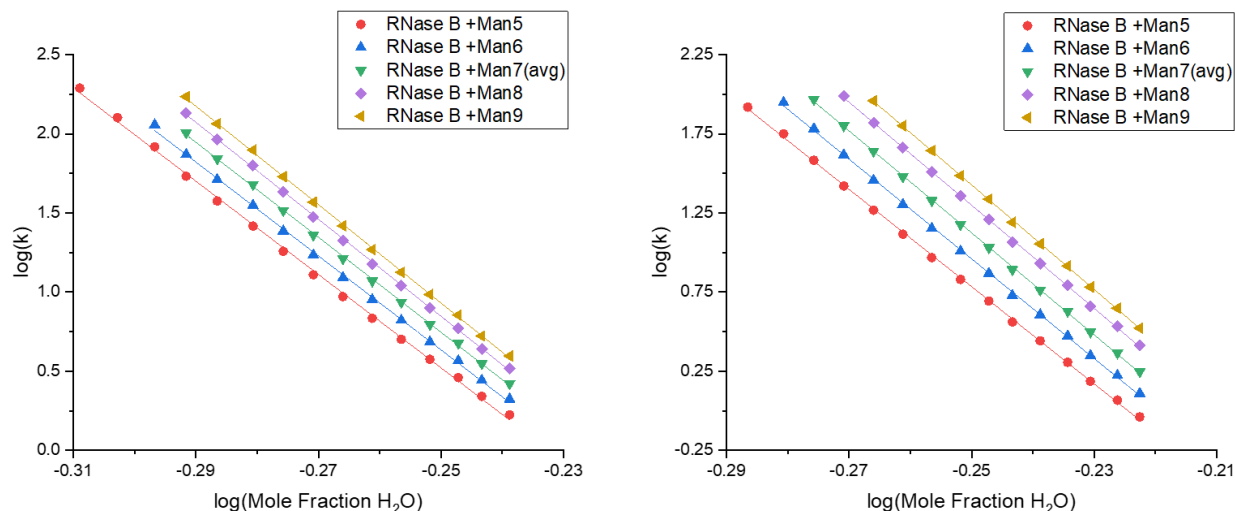


Figure 5.4. Snyder Plots for RNase B glycoforms separated using PHMAAm (left) and PAAm (right) bonded phases

A better balance of performance vs. longevity may be possible by replacing the PAAm with a random copolymer integrating both acrylamide (AAm) and N-(hydroxymethyl)-acrylamide (HMAAm) monomers in the bonded phase synthesis (Figure 5.5). It should be noted that what has been previously referred to as a PHMAAm brush-layer can be more accurately described as a copolymer containing 10-30% AAm monomer. The wide range of estimated AAm content is due to its presence as an impurity in the HMAAm monomer solution, as reported by the manufacturer<sup>3</sup>. Work is now underway to optimize the ratios of AAm and HMAAm for copolymer brush layers on non-porous and superficially-porous particles for improved glycoprotein separations.

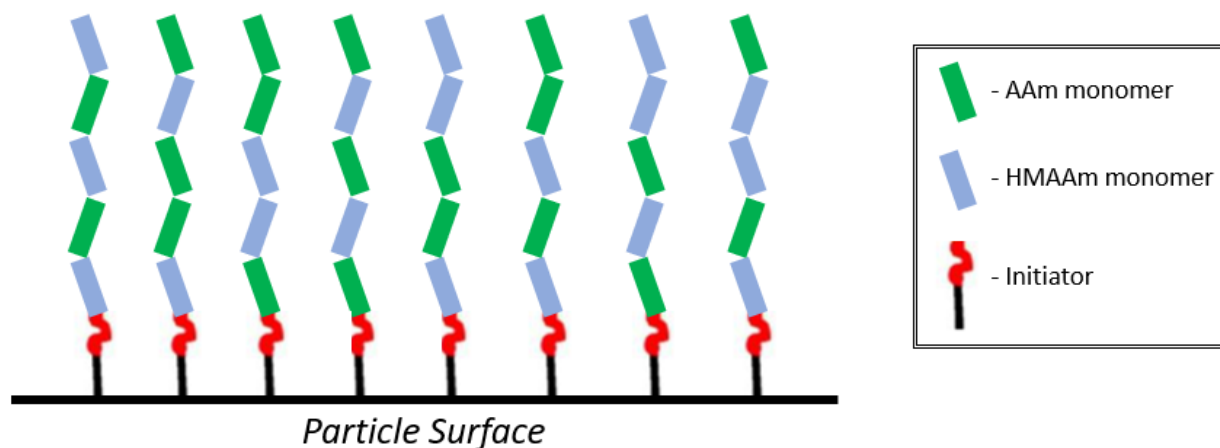


Figure 5.5. Diagram of a random copolymer comprised of AAm and HMAAm monomers

### 5.3 Analysis of Therapeutic mAb Samples and Glycoprotein Biomarkers

The nanoHILIC-MS platform has been developed and refined to the point where it can provide impressive resolution with a complex sample such as the NIST mAb standard. Future work will put it to use in a sample of pharmaceutical interest. Targets are plentiful, but the “low-hanging fruits” that should be first investigated are the pharmaceutically-relevant ADCs and therapeutic mAbs. As discussed in the introductory chapter, the effects of aberrant glycosylation can be life-threatening so the sample profile of a pharmaceutical drug substance should be considerably less complex than that of the NIST mAb. As such, there are known to be fewer peaks to resolve and identify, making this application promising.

Analytical targets for glycosylation analysis are not limited to pharmaceutically-relevant molecules; there are clinically-relevant glycoprotein analytes of great interest as well. Specific sialic acid-containing glycoforms of alpha fetoprotein (AFP) and prostate-specific antigen (PSA) have been implicated in malignant tumor growth and are thus potent biomarkers. Unlike the therapeutic proteins, however, these samples present a daunting analytical challenge. The number of major glycoforms of AFP is disputed, ranging from 6 to 11 as reported by various literature sources<sup>4-6</sup>. PSA is an even more challenging analyte, with approximately 56 glycoforms that would need to be separated<sup>7, 8</sup>. Further, there are other PTMs commonly present for the glycovariants which may broaden the peaks across the nanoHILIC chromatogram<sup>9</sup>. Preliminary results for AFP and PSA have yielded minimal separation with poor resolution, with examples provided in Figure 5.6 and Figure 5.7.

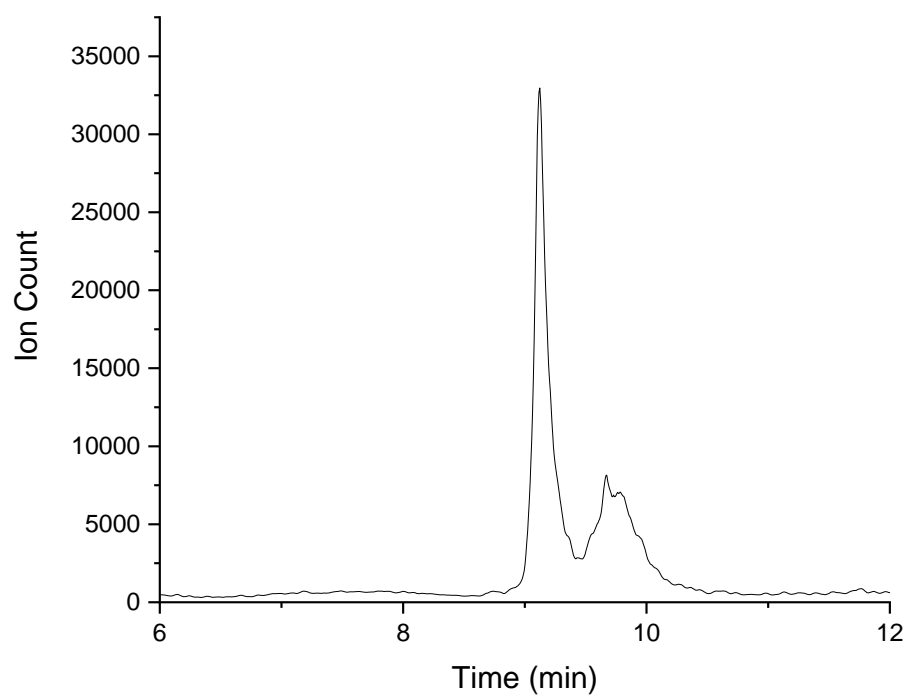


Figure 5.6. nanoHILIC-MS base peak chromatogram for separation of AFP glycovariants, using a gradient of 75% - 60% ACN (+0.1% FA, 0.025% TFA) over 30 minutes



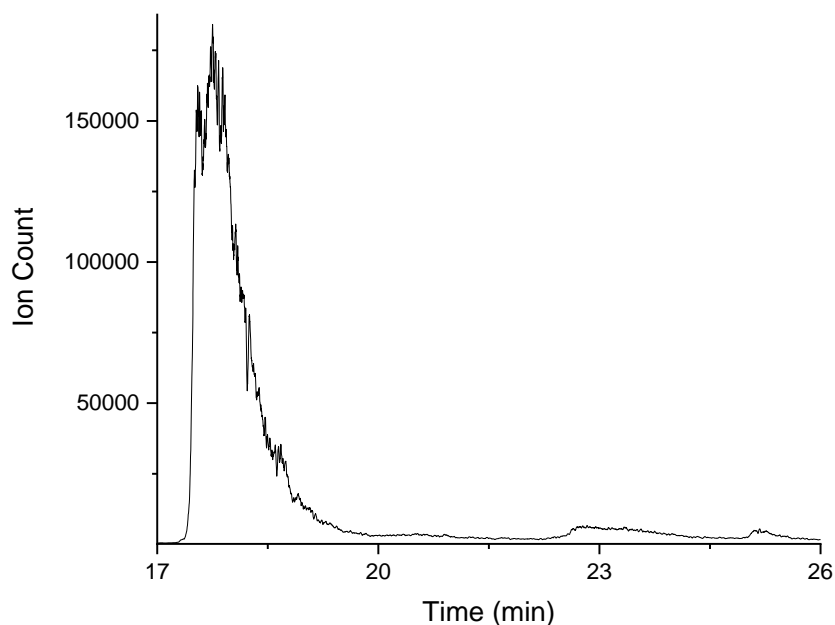


Figure 5.7. nanoHILIC-MS base peak chromatogram for separation of PSA glycovariants, using a gradient of 75% - 60% ACN (+0.1% FA, 0.025% TFA) over 30 minutes

With sample prep to reduce complexity, e.g. fraction collection from ion chromatography, the detection and quantitation of cancer-related intact glycoproteins using the nanoHILIC-MS platform may indeed be feasible.

#### 5.4 References

1. Zhang, Z.; Wu, Z.; Wirth, M. J., Polyacrylamide brush layer for Hydrophilic Interaction Liquid Chromatography of intact glycoproteins. *J Chromatogr A* **2013**, *1301*, 156-61.
2. Smets, G.; Hesbain, A., Hydrolysis of polyacrylamide and acrylic acid-acrylamide copolymers. *Journal of Polymer Science* **1959**, *40* (136), 217-226.
3. SAFETY DATA SHEET: N-(Hydroxymethyl)acrylamide solution. [https://www.sigmaaldrich.com/MSDS/MSDS/PrintMSDSAction.do?name=msdspd\\_20037512182661](https://www.sigmaaldrich.com/MSDS/MSDS/PrintMSDSAction.do?name=msdspd_20037512182661) (accessed March 15, 2020).
4. Johnson, P. J.; Poon, T. C. W.; Hjelm, N. M.; Ho, C. S.; Ho, S. K. W.; Welby, C.; Stevenson, D.; Patel, T.; Parekh, R.; Rr, T., Glycan composition of serum alpha-fetoprotein in patients with hepatocellular carcinoma and non-seminomatous germ cell tumour. *British Journal of Cancer* **1999**, *81* (7), 1188.

5. Johnson, P. J.; Poon, T. C.; Hjelm, N. M.; Ho, C. S.; Blake, C.; Ho, S. K., Structures of disease-specific serum alpha-fetoprotein isoforms. *British journal of cancer* **2000**, 83 (10), 1330-1337.
6. Ichikawa, E.; Kuriyama, S.; Yuji, J.; Masaki, T.; Uchida, N.; Nishioka, M.; Taketa, K., Further resolution of  $\alpha$ -fetoprotein glycoforms by two-dimensional isoelectric focusing and lectin affinity electrophoresis. **2006**, 27 (17), 3480-3487.
7. Scott, E.; Munkley, J., Glycans as Biomarkers in Prostate Cancer. *International journal of molecular sciences* **2019**, 20 (6), 1389.
8. Song, E.; Mayampurath, A.; Yu, C. Y.; Tang, H.; Mechref, Y., Glycoproteomics: Identifying the glycosylation of prostate specific antigen at normal and high isoelectric points by LC-MS/MS. *Journal of Proteome Research* **2014**, 13 (12), 5570-5580.
9. Semeniuk, D. J.; Boismenu, R.; Tam, J.; Weissenhofer, W.; Murgita, R. A., Evidence that Immunosuppression is an Intrinsic Property of the Alpha-Fetoprotein Molecule. In *Immunobiology of Proteins and Peptides VIII: Manipulation or Modulation of the Immune Response*, Atassi, M. Z.; Bixler, G. S., Eds. Springer US: Boston, MA, 1995; pp 255-269.



*Annual Review of Analytical Chemistry*  
Making Sharper Peaks for  
Reverse-Phase Liquid  
Chromatography of Proteins

Charles R. Bupp and Mary J. Wirth

Department of Chemistry, Purdue University, West Lafayette, Indiana 47907, USA;  
email: mwirth@purdue.edu

Annual Rev. Anal. Chem. 2020.13. Downloaded from www.annualreviews.org  
Access provided by CASA Institution Identity on 03/15/20. For personal use only.

Ann. Rev. Anal. Chem. 2020.13:13.1–13.18

The *Annual Review of Analytical Chemistry* is online at  
anchem.annualreviews.org

<https://doi.org/10.1146/annurev-anchem-061318-115009>

Copyright © 2020 by Annual Reviews.  
All rights reserved

#### Keywords

high-performance liquid chromatography, HPLC, efficiency, mAbs, proteomics, fundamentals

#### Abstract

Protein separations have gained increasing interest over the past two decades owing to the dramatic growth of proteins as therapeutics and the completion of the Human Genome Project. About every decade, the field of protein high-performance liquid chromatography (HPLC) seems to mature, having reached what appears to be a theoretical limit. But then scientists well versed in the basic principles of HPLC have invented a way around the limit, generating another decade of exciting progress. There is still the need for higher resolution and better compatibility with mass spectrometry because it is an essential tool for identification of proteins and their modifications. To make advances, the fundamental principles need to be understood. This review covers recent advances and current needs in the context of the principles that underlie the many contributions to peak broadening.

13.1

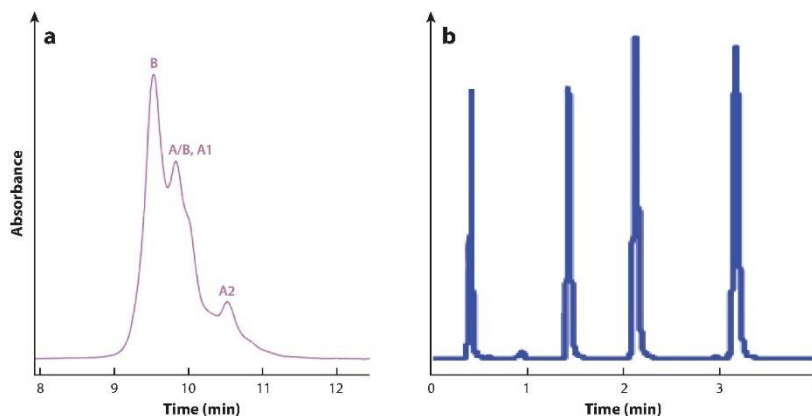


Review in Advance first posted on  
February 28, 2020. (Changes may  
still occur before final publication.)

## 1. INTRODUCTION

The analysis of protein mixtures has emerged as an area of intense research and invention owing to two main drivers. First, the advent of genetic engineering gave rise to a new class of pharmaceuticals, termed biologics, which are made of proteins. Most notable are the therapeutic monoclonal antibodies (mAbs), which target diseases with high specificity (1, 2). Five mAbs are now among the top 15 drugs in terms of sales (3). Second, the Human Genome Project spawned the field of proteomics, which entails the study of changes in gene expression due to metabolism, disease, therapeutics, or environment (4, 5). The analysis of proteins for both pharmaceuticals and proteomics relies on a chemical separation combined with mass spectrometry. There has been much research activity and advancement in the technology for both separations and mass spectrometry of proteins to address the many challenges in protein analysis. This review focuses on advances in protein separations.

**Figure 1** illustrates the state of reverse-phase liquid chromatography (RPLC) of protein in the early twenty-first century, when fully porous particles 3.5  $\mu\text{m}$  in diameter and 300  $\text{\AA}$  in pore size were used (6). The protein is an IgG2 mAb, a subtype that readily undergoes disulfide scrambling, and the chromatogram shows incomplete resolution of perhaps four peaks. For comparison, an RPLC separation of small molecules using a similar column and the same particle size is shown over the same total time range of 4 min (7). The difference is striking, with the protein peaks much broader and closer together. The broader peaks are caused by slower mass transport due to the larger size of proteins. The protein peaks are closer together because these are all variants of the same IgG2 protein. They differ only in regard to which cysteines form disulfide bonds, thereby giving little difference in retention time. If the peaks were as narrow as those of the small molecules, the variants might be resolved.



**Figure 1**

Comparison of reverse-phase liquid chromatography (RPLC) chromatograms for proteins and small molecules using similar Agilent columns. (a) IgG2 monoclonal antibody (mAb) separation of disulfide isoforms using a ZORBAX 300SB-C8 column (2.1  $\times$  150 mm in column dimension with a 3.5- $\mu\text{m}$  particle size and 300- $\text{\AA}$  pore size). Adapted with permission from Reference 6. Copyright 2016, Elsevier. (b) Separation of alkylphenones using the Eclipse XDB-C18 (2.1  $\times$  100 mm in column dimension with a 3.5- $\mu\text{m}$  particle size and 80- $\text{\AA}$  pore size). Adapted with permission from Reference 7 and Agilent Technologies, Inc.

13.2 Bupp • Wirth



Review in Advance first posted on  
February 28, 2020. (Changes may  
still occur before final publication.)

The IgG2 example illustrates a general problem for protein separations: A given protein can have many variants which elute similarly. Variants arise from posttranslational modifications, oxidations, rearrangements, substitutions, and other processes. For protein drugs, variants can have lower drug efficacy and stronger adverse effects; hence, reporting their abundances is required by regulatory agencies. While this example only shows a handful of variants, about two dozen processes affect mAb charge, and there are dozens of positions on the mAb in which such changes can occur (8). In addition, dozens of glycosylation variants exist (9). Aggregation and fragmentation also occur (10). In short, a sample that has one intended protein sequence made by genetic engineering, which ought to be as pure of a protein sample as possible, can have a hundred different variants. The problem is compounded in proteomics, where there are many different proteins. Although the term variants is used for protein drugs, for proteomics, Smith & Kelleher (11) gave the name proteoforms to such species originating from expression of the same gene. The relative abundances of proteoforms are generally the desired information in proteomics. Due to this extreme complexity of samples, improved resolution in protein high-performance liquid chromatography (HPLC) is needed.

## 2. FACTORS THAT AFFECT CHROMATOGRAPHIC RESOLUTION

Resolution  $R_s$  in chromatography is defined by the ratio of peak separation  $\Delta X$  and the peak width at the base  $4\sigma$ , where  $\sigma$  is the standard deviation:

$$R_s = \frac{\Delta X}{4\sigma}. \quad 1.$$

In detail, the resolution is described by terms summarized in **Table 1**: plate height  $H$  as the ratio of peak variance  $\sigma^2$  to column length  $L$ ; plate number  $N$ ; selectivity  $\alpha$  as the ratio of equilibrium constants  $K$  for two analytes being separated; and the retention factor  $k$ , which is  $K$  scaled by the ratio of the stationary phase and mobile phase volumes  $V_s/V_m$ .

$$R_s = \frac{\sqrt{L/H}}{4} \left( \frac{\alpha - 1}{\alpha} \right) \left( \frac{k}{1+k} \right). \quad 2.$$

The equation shows that the resolution increases with the square root of the column length. The length dependence will become important later in this review when the use of smaller particles is discussed because the pressure limits of the instrument limits the column length. The plate height describes how much a peak will spread as it moves along the column. The equation further shows that resolution can only be obtained if  $\alpha > 1$ ; therefore, the choice of appropriate bonded phase and mobile phase is required. The last term,  $k/(1+k)$ , requires the separation medium to have an adequate surface area relative to the volume of mobile phase in the column. Reducing peak broadening needs to be accomplished without correspondingly decreasing  $L$ ,  $\alpha$ , or  $k$ .

**Table 1** Definition of terms to describe resolution in chromatography

Term	Definition
Plate height	$H = \sigma^2/L$
Plate number	$N = L/H$
Selectivity	$\alpha = K_2/K_1 (\geq 1)$
Retention factor	$k = K \cdot V_s/V_m$



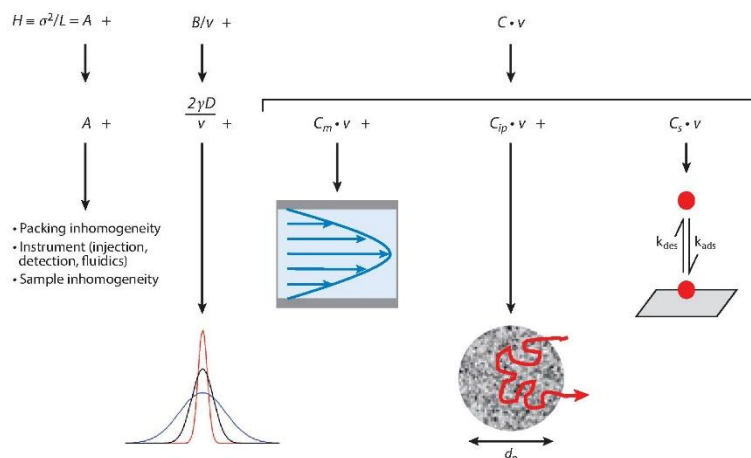


Figure 2

Illustration of the contributions to peak broadening in high-performance liquid chromatography (HPLC).

### 3. CONTRIBUTIONS TO PLATE HEIGHT IN PROTEIN CHROMATOGRAPHY

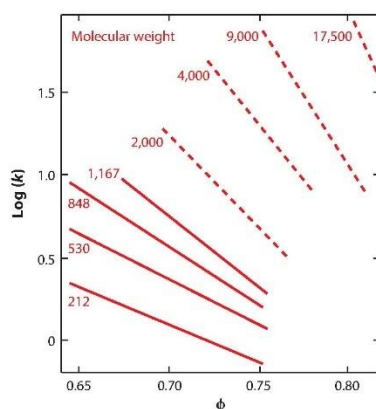
**Figure 2** illustrates the physical phenomena that cause broadening of chromatographic peaks. The van Deemter model suffices here, although more accurate models exist (12). The first term,  $A$ , lumps together all contributions to broadening that are approximately independent of flow rate. The  $B$  term is from diffusion along the separation axis. Because the  $C$  term is due to slow mass transport of protein, its effect on  $H$  increases with velocity. Multiple phenomena contribute to  $C$ : (a) the distribution of velocities owing to the parabolic Poiseuille flow profile between particles, dictated by  $\omega_m$ ; (b) the delay in transport owing to the need for diffusion in and out of porous particles, dictated by  $\omega_p$ ; and (c) slow desorption of the analyte from the bonded phase back into the mobile phase, dictated by  $\tau_{des}$ . Since variances are additive for independent variables, these contributions sum to give the van Deemter equation:

$$H = A + \frac{B}{v} + C \cdot v = A + \frac{2\gamma D}{v} + \omega_m \frac{d_p^2}{D} v + \omega_p \frac{d_p^2}{D} v + \frac{2k}{(1+k)} \tau_{des} v. \quad 3.$$

A plot of plate height versus velocity,  $v$ , reveals the values of  $A$ ,  $B$ , and  $C$  if the velocity range is sufficient. Although the literature is rife with van Deemter plots for small molecules, these are scarce for proteins. The reason is that the van Deemter equation applies to isocratic separations, i.e., separations where the mobile phase has a constant composition, whereas protein HPLC is invariably performed with gradient elution. **Figure 3**, which depicts plots of  $\log(k)$  versus fraction of organic phase,  $\phi$ , in the case of RPLC, helps to explain why gradient elution is needed. For small molecules, the slope is low, so one mobile phase composition will elute a wide range of compounds. For proteins, the slope is high and the intercepts differ, so a range of compositions is usually needed for elution on a reasonable timescale. The van Deemter equation does not apply to gradient elution because the velocity of the protein changes as it travels through the column







**Figure 3**

Plot of  $\log(k)$  versus the fraction of acetonitrile, for a mobile phase of acetonitrile/water, illustrating why gradient elution is widely used for reverse-phase liquid chromatography (RPLC) of protein but less so for small molecules. The dashed lines are representative rather than directly from data for those molecular weights. Adapted with permission from Reference 13. Copyright 1983, American Chemical Society.

(13), whereas the van Deemter model requires a constant velocity of the protein. Gradient elution also gives compression in the width of the peak because the leading side travels more slowly than the trailing side of the peak, where the solvent is stronger (14). As a result of both of these factors, peak widths for gradient elution generally remain constant even for long elution times, in contrast to peaks for isocratic elution, which broaden with elution time. Consequently, one cannot directly obtain efficiency data from most of the data in the literature for protein separations.

**Figure 4a** shows an informative van Deemter plot for a protein, published by Wu et al. (15). The figure compares van Deemter plots for two columns using particles of the same 1.5- $\mu\text{m}$  diameter, one porous and the other nonporous, to assess the contribution from intraparticle diffusion. There is no rise in plate height at low velocity, indicating that the value of  $B/v$  is much smaller than  $A$  and  $C \cdot v$  over the velocity range. For the velocities typically used in protein separations, from 0.1 to 0.3 cm/s, the main contribution to the plate height is  $C$ . The plot illustrates that using nonporous particles significantly lowers the value of  $C$ , with  $C \sim 34$  ms and  $\sim 20$  ms for the porous versus nonporous particles, respectively. For small molecules, **Figure 4b** shows  $C$  as more than an order of magnitude smaller, owing mainly to the diffusion coefficients of small molecules being much larger. The data, while noisy, report  $A \sim 7$   $\mu\text{m}$  for the proteins. For the small molecule,  $A$  must be smaller because the minimum  $H$  is typically on the order of 10  $\mu\text{m}$  (16). A discussion of the  $A$  term shows that it has no dependence on molecular size or diffusion coefficient, and it is for a different reason that the  $A$  term is high for proteins in this case.

The factors contributing to  $A$ ,  $B$ , and  $C$ , and the expected numbers for these are detailed in the next subsections.

### 3.1. Contributions to Broadening from the $A$ Term

The lower limit for plate height in protein RPLC is dictated by the  $A$  term in the van Deemter equation. While decreasing the flowrate can progressively lower the plate height by lessening the



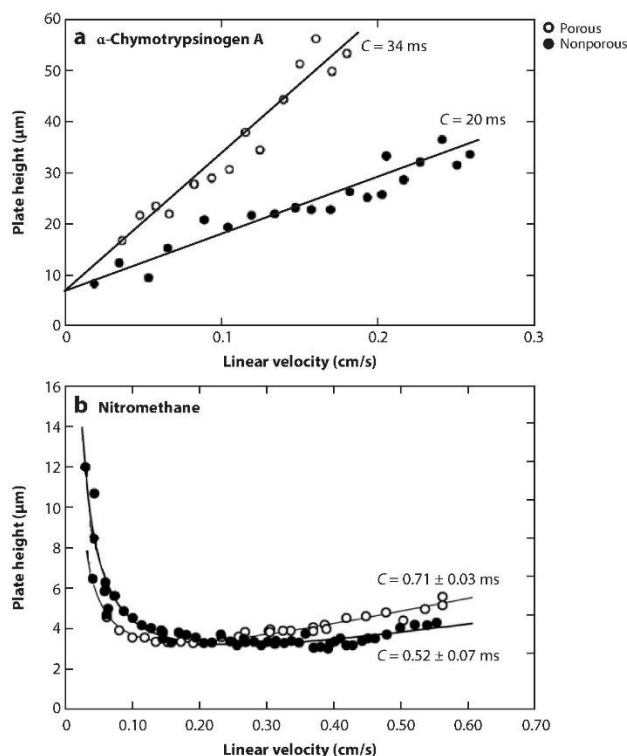


Figure 4

(a) van Deemter plots for the protein  $\alpha$ -chymotrypsinogen A, and (b) van Deemter plots for unretained nitromethane. The plots compare porous (open circles) and nonporous (filled circles) particles, each with  $C_{18}$  on 1.5- $\mu\text{m}$  particles. The estimated values of  $C$  are indicated on the graphs. Adapted with permission from Reference 15. Copyright 2006, Elsevier.

impact of the  $C$  term, the contributions from extra-column effects and eddy diffusion establish an absolute minimum value for  $H$ .

**3.1.1. Broadening by the instrument.** In Figure 4, the largest contribution to  $A$  is the peak dispersion from the instrument itself. Its contribution is magnified for proteins compared to small molecules because protein separations are done using narrower column i.d. to allow for analysis of smaller amounts of valuable sample. The instrument used by Wu et al. (15) has the current industry standard for low dispersion,  $\sigma_V \sim 2 \mu\text{L}$ . The column is also typical for proteins, with a short length of 50 mm and a narrow i.d. of 2.1 mm, making the column volume low. The porosity,  $\epsilon$ , of the column is the ratio of the liquid volume to the geometric volume of the column, and this is typically 0.4. The limit has been shown by Schure et al. (17) to be 0.36 for randomly packed





particles. If the column contributed nothing to broadening, then a peak broadened to 2  $\mu\text{L}$  by the instrument would give a plate height of 5.4  $\mu\text{m}$  if the column has a 2.1 mm i.d. and length of 50 mm, with  $\varepsilon = 0.4$  and  $k = 2$ . The calculation is shown in Equation 4 for clarity:

$$A_{\text{instr}} = \frac{\left(0.002 \text{ cm}^3 / \pi \cdot (\text{i.d.}/2)^2 \text{ cm}^2 \cdot \varepsilon\right)^2}{L \cdot (1+k)^2} = 5.4 \times 10^{-4} \text{ cm.} \quad 4.$$

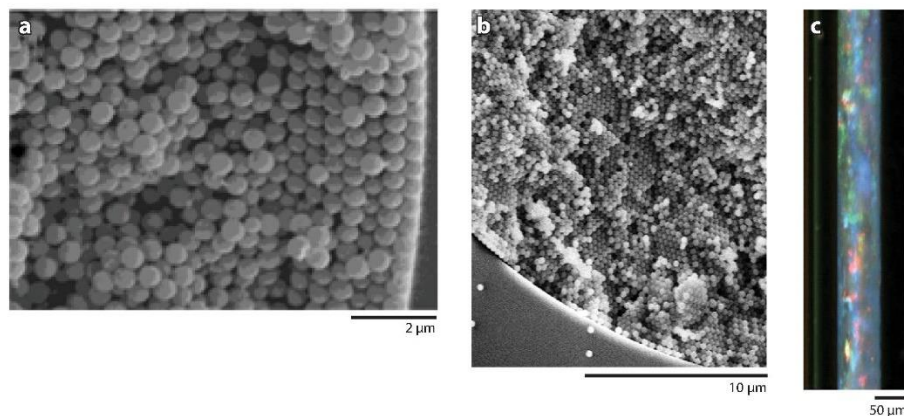
The calculation illustrates that under the best circumstance of only 2  $\mu\text{L}$  of dispersion from the instrument, it can contribute significantly to the overall  $A$  term at low velocity. Considering that the typical linear velocity is on the order of 0.25 cm/s (at 0.2 mL/min),  $k$  is usually larger than 2, and the plate height in **Figure 4** is 35  $\mu\text{m}$  for the nonporous particles, it is clear that the  $A$  term from the instrument itself contributes little to peak broadening in a typical separation with a high performance instrument. Longer columns, in turn, would make the contribution even less significant.

While we conclude that the  $A$  term has only a small contribution to peak broadening for this low-dispersion instrument, the  $A$  term will become more important as the  $C$  term is decreased through advances in column materials. Further, one has a choice in configuring the instrument, which can easily increase its dispersion to become significant. There are three main contributions of the instrument to broadening, as detailed by de Vos et al. (18): (a) the injected volume, (b) the tubing inner diameter, and (c) the detection volume. These factors need to be considered when broadening from the instrument is a limitation to efficiency.

**3.1.2. Nonuniform column packing.** The textbook description of the  $A$  term is the heterogeneity of the packed bed. Advances in the engineering of column packing have made it typically less significant than the instrument contribution, but future advances could make heterogeneity of the packed bed a significant factor again. Farkas & Guiochon (19) showed that packed beds are radially heterogeneous in packing density, giving slower flow near the walls. Radial heterogeneity of packing is visually depicted for a capillary in **Figure 5a** for 1- $\mu\text{m}$  silica particles (20). The image from scanning electron microscopy (SEM) shows that the packing density is highest near the wall, giving more resistance to flow near the wall and, hence, a higher mobile phase velocity away from the walls. Our group showed that packing under sonication reduces the  $A$  term to the nanometer scale for capillaries (21), and this is illustrated by the SEM image in **Figure 5b** for the case of 0.5- $\mu\text{m}$  nonporous silica particles. **Figure 5c** is a photograph of a capillary packed with mild sonication to maximize domain size, showing strong opalescence associated with crystalline packing. In summary, the 2.1-mm i.d. columns typically used for analytical protein separations currently give a relatively small  $A$  term, as evidenced by the van Deemter plot of **Figure 4**.

**3.1.3. Effect of protein heterogeneity on measurement of  $A$ .** The inevitable existence of proteoforms in the sample can make the column efficiency appear worse than it is. This is illustrated mathematically in **Supplemental Figure 1** by using synthetic Gaussians. If the proteoforms have slightly different retention factors, but not different enough to elute beyond the standard deviation of other proteoforms, the collection of peaks gives one broad peak that is wider than what the true column efficiency would give. A van Deemter plot in **Supplemental Figure 1** using the synthetic Gaussians illustrates that such a heterogeneous sample would report the correct value of  $C$ , but an erroneously high value of  $A$  by increasing the intercept. This is a possible way of assessing heterogeneity of a peak. We reported an unexpectedly high  $A$  term of 21  $\mu\text{m}$  for a hydrophilic interaction liquid chromatography (HILIC) separation of protein glycoforms (22). It perplexed us at the time, but this simulation gives a likely explanation for the high  $A$  term.





**Figure 5**

Images of nonporous silica packed in capillaries. (a) A scanning electron microscope (SEM) image of slurry-packed 1- $\mu\text{m}$  particles shows denser packing near the wall. Adapted with permission from Reference 20. Copyright 2004, American Chemical Society. (b) An SEM micrograph of 0.5- $\mu\text{m}$  particles packed with sonication, showing face-centered cubic domains well away from the wall. Adapted with permission from Reference 31. Copyright 2012, American Chemical Society. (c) Color photograph of a capillary packed in the same way as in panel b, showing the opalescence characteristic of crystalline packing of silica particles. Adapted with permission from Reference 30. Copyright 2013, American Chemical Society.

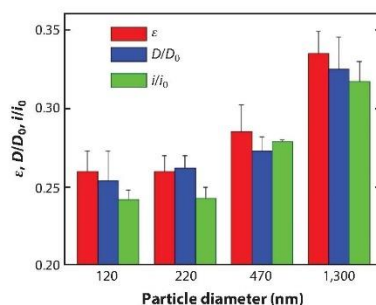
### 3.2. Contribution from the $B$ Term: Diffusion Through Porous Media

**Figure 2** illustrated that the  $B$  term in the van Deemter equation is caused by molecular diffusion along the separation axis. Using the Stokes equation  $\sigma^2 = 2Dt$  and the mobile phase velocity  $v = L/t_m$ , one arrives at  $\sigma^2 = 2D/v$  if diffusion only occurs in the mobile phase, i.e., during the time  $t_m$  it takes for the mobile phase to travel the length of the column. One adjustment needs to be made: The diffusion is obstructed because the volume of the mobile phase is not fully accessible to the analyte.

$$H_B = \frac{2\gamma D}{v}. \quad 5.$$

The obstruction factor is typically written as  $\gamma$ , which is a fraction between 0 and unity. Knox & McLaren (23) used gas chromatography measurements to show that  $\gamma = 0.6$  for nonporous glass beads, with variations in the next significant figure. The equation neglects diffusion of adsorbed analytes, which can be a large factor for small molecules (24). Proteins do not diffuse detectably when adsorbed, presumably due to the multiplicity of interactions with the bonded phase, therefore, Equation 5 only includes  $D$  for proteins in the mobile phase. For  $\gamma = 0.6$  and for a protein having  $D = 10^{-6}$  cm<sup>2</sup>/s,  $H_B = 0.1$   $\mu\text{m}$  at the relatively low linear velocity of 0.1 cm/s. This is below the noise on a van Deemter plot, explaining why there is no visible contribution of the  $B$  term for the protein in the van Deemter plot of **Figure 4a**. This section could be ended here, but diffusion is the molecular property that controls much of the  $C$  term, so it is important to understand how diffusion is obstructed in porous media. Most pertinent to the discussion is





**Figure 6**

Data for capillary porosity measured by flow properties for four different capillaries (red bars), each packed with different particle diameters. The ratio of the diffusion coefficient inside the packed capillary to that for an open capillary is shown for each case (blue bars). The ratio of the ionic current through the packed capillary to that through an open capillary is shown for each case (green bars). The error bars in all cases represent error from replicate capillaries. All data agree within error, indicating that the obstruction factor is the porosity. Adapted with permission from Reference 27. Copyright 2013, American Chemical Society.

that diffusion into and out of porous particles, which is soon shown to contribute significantly to broadening, is also obstructed.

In the materials literature, the obstruction factor is taken to be the porosity,  $\epsilon$ , scaled by a tortuosity factor,  $q$ , which is approximately 0.7 (25). This concept applies broadly to mass transport, first recognized by James Clerk Maxwell in the nineteenth century for electric current through porous media (26). Our group tested the idea of porosity unifying the obstruction of diffusion and of ionic current in chromatographic media (27). A series of capillaries packed with particles of varying diameter was prepared. The value of  $\gamma$  was measured optically by diffusion of a small molecule, fluorescein, in the packed capillary versus in an open capillary. The porosity for each capillary was determined by measuring back pressure,  $\Delta P$ , as a function of mobile phase velocity, and calculating  $\epsilon$  through the Kozeny-Carman equation:

$$\frac{\Delta P}{L} = \frac{180 \cdot \eta \cdot (1 - \epsilon)^2}{d_p^2 \cdot \epsilon^3} v. \quad 6.$$

Further, ionic current was measured in the same packed versus open capillaries. There were no frits to add to the overall porosity. The three independent measurements of porosity were shown to agree, as illustrated in the graph of **Figure 6**. The experimental error obscures the small predicted effect of tortuosity on  $\gamma$ , hence  $\epsilon$  is a reasonable approximation for  $\gamma$ . One can see that the porosity gradually increases with particle size since the larger particles do not pack as tightly, which also serves to illustrate why there is no set value of  $\gamma$  (24).

The obstruction factor can become much smaller than  $\epsilon \cdot q$  when the interstitial space approaches the sizes of the molecules, which often happens for proteins (27). A predictable decrease in diffusion is observed, which will be discussed in more detail in Section 3.3.2. The van Deemter plots of **Figure 4** showed that the most urgent factor that needs attention is the  $C$  term. The plots also give a preview of one way to decrease the  $C$  term: use nonporous particles. This is detailed in the next subsection.





### 3.3. Contributions to the $C$ Term

At higher flowrates, mass transport effects become the main contributors to peak broadening. While the advent of superficially porous and sub-2- $\mu\text{m}$  particles has lessened its impact, the  $C$  term remains a key consideration when working to reduce peak widths.

**3.3.1. Poiseuille flow profile.** The contribution from the Poiseuille flow profile,  $C_m$ , depicted in Figure 2, is unavoidable under pressure driven flow. It is the only contribution to  $C$  when particles are nonporous and desorption is fast. Since  $C_m$  appears to be significant based on the van Deemter plots of Figure 4, even for these sub-2- $\mu\text{m}$  particles, one might wonder if there is any room for improvement. Yan & Wang (28) used numerical simulations to determine how low of a plate height one could theoretically obtain if  $B$  and  $C_m$  were the only contributors to plate height. The simulations were for particles packed with face-centered cubic arrangement and no retention. The results indicated that the minimum plate height at optimal velocity is proportional to particle diameter when only  $B$  and  $C_m$  contribute to  $H$ :

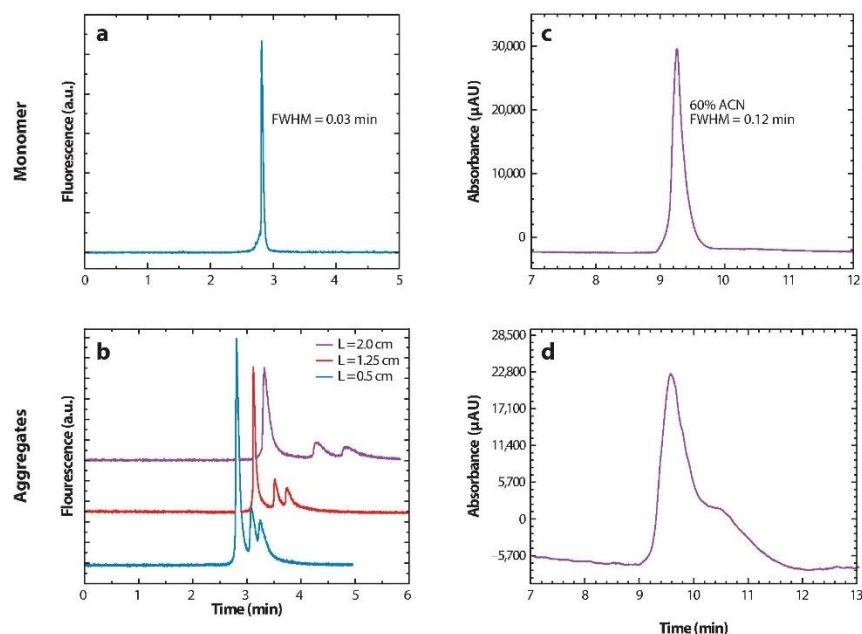
$$H_{\min} = 0.084 \cdot d_p. \quad 7.$$

Using this equation for 1.5- $\mu\text{m}$  particles,  $H_{\min} = 140$  nm, which predicts approximately 100-fold improvement in efficiency compared to that depicted in Figure 4a, offering potentially 10 times higher resolution for protein separations. Yan and Wang further showed in the same paper that slip flow decreases the factor in Equation 7 from 0.084 to 0.059 by virtue of decreasing the velocity distribution. Schure et al. (17) showed that the minimum plate height increases only by about factor of two when particles are randomly packed; therefore, crystalline packing is not a requirement for large improvements in plate height. Theory thus points to the possibility of much higher efficiency.

One might then ask why people do not use even smaller nonporous particles to gain higher surface area to decrease overloading and to gain even lower plate heights. Particles of 0.5  $\mu\text{m}$  would have a threefold-higher surface area than 1.5- $\mu\text{m}$  particles and also give a minimum plate height predicted by Equation 7 to be only 42 nm. Nonporous particles of 0.47  $\mu\text{m}$  have been investigated in capillaries to assess the possible advantage. By using trifunctional silanes to hold the particles together (29), no frit was needed. Further, instrumental broadening was greatly decreased by injection via diffusion and then using on-column fluorescence microscopy for detection. Figure 7 confirms that a dramatic improvement is gained for separation of a monoclonal antibody and its aggregates, comparing the 0.5- $\mu\text{m}$  particles in a capillary to porous 1.7- $\mu\text{m}$  particles in a 2.1/50-mm column (30). The resolution is about fourfold higher for the 0.5- $\mu\text{m}$  particles. This could be further improved by injecting a smaller amount of protein because the asymmetric peaks indicate overloading for the 0.5- $\mu\text{m}$  nonporous particles. Nonetheless, the improvement is already dramatic.

A plate height as small as 15 nm was observed for separation of labeled bovine serum albumin with a capillary packed with 0.47- $\mu\text{m}$  particles (31). The plate height corresponds to  $0.032 \cdot d_p$ , which is more than twofold smaller than that predicted by the theory represented in Equation 7. The theory did not take into account the size of the protein, which causes further obstruction since the volume available to the protein is decreased. This was investigated quantitatively, showing that the obstruction factor has a second term that become significant for such small particles (27). The value of  $R$  is the local radius of the interstitial space, and  $r$  is the radius of the protein. Using the idea that diffusion stops when the protein is in contact with the surface, we introduced the factor





**Figure 7**

Separation of an IgG4 monoclonal antibody (mAb) and its aggregates, comparing 0.5- $\mu\text{m}$  nonporous particles with 1.7- $\mu\text{m}$  porous particles. For the 0.5- $\mu\text{m}$  nonporous silica, the samples are (a) monomer and (b) monomer with aggregates, for varying separation length. For the commercial stainless steel column, the same samples are studied: (c) monomer and (d) monomer with aggregates. Adapted with permission from Reference 30. Copyright 2013, American Chemical Society. Abbreviations: ACN, acetonitrile; FWHM, peak width at half-height.

$[(R - r)/R]^2$  to account for the volume fraction accessible to the protein when not in contact with the surface:

$$\gamma = \varepsilon \cdot \left( \frac{R - r}{R} \right)^2. \quad 8.$$

The parentheses have the same factor as in Giddings' (32) textbook description of the equilibrium constant for size exclusion chromatography, which equals the accessible volume fraction. The value of  $R$  is assumed to be the hydrodynamic radius of the medium, which is the radius an open capillary would have if it had the same surface area to volume ratio as the packed bed (33):

$$R = \frac{d_p}{3} \frac{\varepsilon}{1 - \varepsilon}. \quad 9.$$

Using Equation 9 to obtain  $R$  for Equation 8, which describes obstructed diffusion well (27), would reduce the proportionality constant to in Equation 7 to 0.068, still giving twofold disagreement between experiment and the numerical simulations. Beyond obstruction of diffusion, another



consequence of finite protein size relative to the interstitial space is that the protein cannot diffuse all the way to the intersection points between particles due to its nonzero dimensions. These regions contribute the most to the plate height because they are furthest from the center of the flow stream. The numerical simulations that gave Equation 7 do not account for this factor in plate height; hence, Equation 7 is an overestimate of  $H_{\min}$ .

Smaller particles 350 nm in diameter were shown to obstruct diffusion by an order of magnitude (21), which is more obstruction than indicated by Equations 8 and 9. Denaturation of the protein to increase its radius is one possible explanation for the surprise. Another explanation is that the model for  $R$  in Equation 9 is not sufficiently accurate to avoid large errors in subtracting similar numbers in Equation 8. The 350-nm particles also gave a measured  $A$  term of  $0 \pm 1$  nm in electrochromatography, and no  $C$  term was detectable (21). It would be interesting to investigate these very small particles for IIPLC.

These studies show that when the interstitial space approaches molecular dimensions, extremely low plate heights are possible. But using such small particle increases back pressure. The back pressure problem is partially alleviated because these materials give slip flow, mentioned earlier, which enhances flow rate when the fluid is nonwetting on the surface (34). A fivefold enhancement in flow rate was shown for water in capillaries packed with hydrophobic 0.5- $\mu\text{m}$  particles, and flow rate enhancement was shown to be inversely proportional to particle diameter (35). Smaller particles would also increase surface area. New instrumentation would need to be designed to accrue the advantages of submicrometer silica particles in HPLC.

**3.3.2. Intraparticle diffusion.** The van Deemter plots of **Figure 4** compared porous and nonporous particles for a protein separation. Assuming that the only difference in  $C$  is from intraparticle diffusion, the plots illustrate visually that intraparticle diffusion contributes about twice as much to the  $C$  term as other contributions to  $C$ . This has made intraparticle diffusion a target for improving protein separations, and this improvement is much of the story of HPLC so far in the twenty-first century. Equation 3 described broadening from intraparticle diffusion as increasing with the ratio  $d_p^2/D$ , as one would intuitively expect from Stoke's law ( $\sigma^2 = 2Dt$ ), but with the proportionality factor  $\omega_{ip}$ :

$$H_{ip} = \omega_{ip} \frac{d_p^2}{D} v. \quad 10.$$

Horváth & Lin (36) derived an expression for  $\omega_{ip}$  in terms of retention factor, the ratio of intraparticle porosity to total porosity  $\psi$  and tortuosity  $q$ :

$$\omega_{ip} = \frac{\psi}{30 \cdot q \cdot (1 + \psi)^2}. \quad 11.$$

Assuming tortuosity to be 0.7, as in the earlier discussion of obstructed diffusion,  $C_{ip}$  is calculated to be 4 ms for the 1.5- $\mu\text{m}$  particles and the usual approximation of  $D = 10^{-6}$ . The van Deemter plots in **Figure 4a** allow an estimation of  $C_{ip}$ . For the fully porous and nonporous particles, the estimated  $C$  values from the graph are 34 ms and 12 ms, respectively. The difference between the two  $C$  terms, 22 ms, equals the value of  $C_{ip}$  since contributions to  $H$  are additive. This assumes that the others factors affecting  $C$  are the same for the two columns. The disparity between the prediction from Equation 10 and the data in **Figure 4a** could be because of the data being obtained under conditions of retention, whereas the equation was derived for no retention. In addition, the equation does not account for obstruction due to the nonzero size of the protein relative to the pores.

13.12 Bupp • Wirth



Review in Advance first posted on  
February 28, 2020. (Changes may  
still occur before final publication.)

Equation 10 illustrates why sub-2- $\mu\text{m}$  particles were introduced, and commercial columns were shown to approach the theoretically predicted improvements in efficiency (16). The back pressure increases with the inverse square of particle diameter, as illustrated by Equation 6. This necessitated the development of instruments with higher pump pressures. Instruments had pressure limits on the order of 4,000 psi, which is insufficient for the submicrometer particles. Newer instruments delivered pressures on the order of 10,000 psi, and the technique was initially called ultraperformance liquid chromatography (UPLC), then was called UHPLC, and is often called HPLC once again. With particle diameters being half that of the 3.5- $\mu\text{m}$  particles used with the HPLC instruments, logic would dictate that HPLC instruments should have delivered 16,000 psi. Only in the last few years have they reached such pressures; therefore, shorter columns, e.g., 5 cm, became common in UHPLC until recently. Equation 1 shows resolution to be proportional not just to  $H^{1/2}$  but to  $(H/L)^{1/2}$ . Because of pressure limits, the larger particles outperform smaller particles in resolution by virtue of column length. This is why larger particles are commonly used in proteomics. What the smaller particles do offer is speed: Resolution per minute is higher. Also, sensitivity is higher with shorter columns because peaks broaden in proportion to  $L^{1/2}$ .

Instruments with increasing pressure have been introduced over the last decade. These can also cause problems: Higher pressure changes retention times for proteins due to denaturation (37, 38). Despite the higher pressure now available commercially, particle diameter has not decreased significantly. One reason is because frictional heating decreases efficiency, and this is noticeable for efficient small-molecule separations (39–41). The power  $W$  used to force liquid to flow through the column by the pressure  $P$  at a volume flow rate  $Q$  releases the energy in the form of heat:

$$W = P \cdot Q. \quad 12.$$

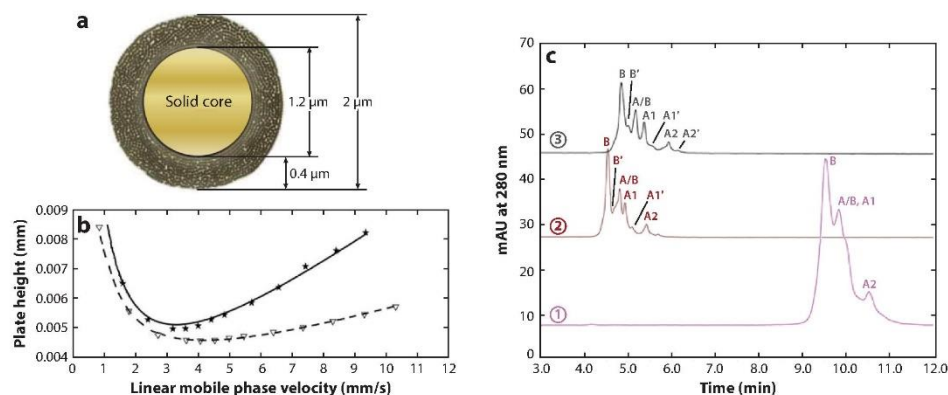
The walls of stainless steel columns remain close to the thermostat temperature due to the high thermal conductivity of metal, giving rise to a temperature gradient from the center of the packed bed to the walls. Both the equilibrium constant for adsorption and the mobile phase viscosity depend on temperature, thus imparting a radial heterogeneity of retention times across the column, thereby decreasing column efficiency. Frictional effects are not noticeable for proteins because mass transport contributes more than frictional heating (37). Frictional heating is decreased for slip flow, which occurs with submicrometer nonporous particles; for example, for a flow enhancement of 5 from slip flow, the frictional heating calculated from Equation 12 would be decreased by a factor of 5. The difficulty of making ever smaller porous particles, along with the onset of frictional heating for porous particles, has so far slowed the work in making smaller particles.

A bigger factor that has slowed efforts in making smaller porous particles was the commercialization of fused-core particles, illustrated in **Figure 8a**. These particles decrease the distance for diffusion through the pores, giving a decrease in variance through Stokes' law. Because the distance for intraparticle diffusion is no longer strapped to particle size, larger particles can be used to allow longer columns without requiring higher pressures. The surface area is lower than that of totally porous particles but still higher than that for nonporous particles. These are also called superficially porous particles, which is a lengthier name, or core-shell particles, a term that is ambiguous because it is used in another context in materials science.

A van Deemter plot in **Figure 8b** compares fused-core particles of various diameters with totally porous particles to illustrate that these give lower  $C$  terms than sub-2- $\mu\text{m}$  totally porous particles despite being larger in diameter (42). Specifically, comparing the curves for the totally porous 1.7- $\mu\text{m}$  particles (stars), with the 2.0- $\mu\text{m}$  fused-core particles for which the shell is shown







**Figure 8**

(a) Idealized illustration of the structure of a typical fused-core particle, with an impermeable core surrounded by a porous shell. (b) van Deemter plots for a small molecule (naphthalene) for various fused-core particles in comparison to 1.7- $\mu\text{m}$  totally porous particles. (c). Comparison of mAb A disulfide isoform separation using different RP-UHPLC columns, from bottom to top: ① ZORBAX 300SB-C8 column (2.1  $\times$  150 mm in column dimension with a 3.5- $\mu\text{m}$  particle size and 300- $\text{\AA}$  pore size); ② HALO Protein C4 column (2.1  $\times$  150 mm in dimension with a 3.4- $\mu\text{m}$  particle size, 0.2- $\mu\text{m}$  shell thickness, and 400- $\text{\AA}$  pore size); and ③ HALO Protein C4 column (2.1  $\times$  150 mm in column dimension with a 2.7- $\mu\text{m}$  particle size and 1,000- $\text{\AA}$  pore size). Panels a and b adapted with permission from Reference 42. Copyright 2014, Elsevier. Panel c reprinted from adapted with permission from Reference 6. Copyright 2017, Elsevier. Abbreviations: mAb, monoclonal antibody; RP-UHPLC, reverse-phase ultrahigh-performance liquid chromatography.

to be 0.4  $\mu\text{m}$  thick (triangles), the  $C$  term is nearly fivefold lower for the fused core particles. This demonstrates the effect of the shorter diffusion distance in the fused particles. The minimum plate height is lower by almost a factor of two, and the optimal velocity is higher, giving more separation speed. The 2.7- $\mu\text{m}$  fused-core particles give similar efficiency to the 1.7- $\mu\text{m}$  totally porous particles but would allow a longer column length of  $(2.7/1.7)^2 = 2.5$ -fold for the same back-pressure, giving 2.5-fold more plates. It is clear why the fused-core particles are currently a dominant technology.

In the past, particles with an average pore size of 300  $\text{\AA}$  had been considered to be wide-pore particles, and these were widely used for protein RPLC. In size-exclusion chromatography, antibodies are mostly excluded from these particles. By the same token, they would be excluded from 300- $\text{\AA}$  RPLC particles, and likely even more excluded since denaturation by the organic solvent would increase their sizes. With the growth of mAbs in the pharmaceutical industry, it has become necessary to increase pore size, and this advance has been made recently. Fused-core particles with pore diameters large as 1,000  $\text{\AA}$  are now commercially available. The effect of pore diameter on the same mAb separation introduced in Figure 1 is shown in Figure 8c. The progressively wider pores, from 300 to 400 to 1,000  $\text{\AA}$ , show progressively more proteoforms. One wonders whether wider pores yet would reveal even more.

### 3.4. Slow Desorption and Reduction of Tailing

Giddings' textbook (32) provides an equation for the contribution to the plate height due to slow desorption from the bonded phase  $H_s$ . The equation was derived using the random walk model

13.14 Bupp • Wirth



Review in Advance first posted on  
February 28, 2020. (Changes may  
still occur before final publication.)



and first order desorption kinetics, showing that  $H_i$  is proportional to the desorption time constant  $\tau_{des}$ :

$$H_i = 2 \cdot \frac{k}{(1+k)^2} \tau_{des} v. \quad 13.$$

Values for  $\tau_{des}$  of proteins are not well known, although single-molecule spectroscopy is beginning to provide these data (43). Temperature studies of RPLC separations of mAbs show little if any change in peak width as temperature is changed from 40°C to 80°C (44), suggesting that  $C_s$  might not be a limiting factor for efficiency. Further, in these same studies, selectivity decreases twofold from lowest to highest temperature over this range, indicating that lower temperature should give better resolution. Nevertheless, people use 80°C for mAb separations despite the lower resolution because quantitation is better, as indicated by a slight loss in peak area as temperature is lowered. In the results shown earlier for 0.5- $\mu$ m particles, the mAb separation was run at room temperature, yet no accumulation of protein was observed on the material in the fluorescence images. It could be that the trifunctional silanes yield less protein loss. Another possibility is suggested by the work of Eschelbach & Jorgenson (45): Higher pressure gives higher protein recovery. A third possibility is that the protein is lost on the frits or tubing rather than on the particles. The latter is documented to be the case in size exclusion chromatography, which is performed at lower temperatures (46). Advances will likely bring RPLC of mAbs closer to room temperature for higher resolution, and it will be interesting to see how many proteoforms in **Figure 8** will then be identified.

No discussion of  $C_s$  in RPLC would be complete without a mention of mixed-mode adsorption in RPLC, which has been studied extensively for small molecules. On the silica surface, the low-abundance, isolated silanols that have low  $pK_a$  cause tailing because these give large equilibrium constants so that typical HPLC concentrations are in the nonlinear part of the Langmuir adsorption isotherm (47). The isolated silanols also cause peak broadening even under nonoverloading conditions (47). The isolated silanols were shown to be due to topographical asperities (48); combining spectroscopic imaging and atomic force microscopy, no strong sites are observed in topographically smooth regions (49, 50). The trifunctional silanes discussed earlier were shown to block the dissociation of isolated silanols even on low quality silica that has large amounts of isolated silanols, provided that the amount of adsorbed water is controlled (51). The unusually high efficiency of the mAb separation shown in **Figure 7**, obtained using trifunctional silanes and high quality silica, indicates that the  $C_s$  term can be made negligible.

The isolated silanols, by virtue of their high acidity, have necessitated the use of trifluoroacetic acid (TFA) in RPLC to neutralize the isolated silanols, thus minimizing peak broadening. TFA causes much lower sensitivity when using electrospray ionization for mass spectrometry due to its amphiphilic structure and its propensity for ion pairing with proteins. For mass spectrometry, formic acid or acetic acid are preferred, but these have  $pK_a$  values that are several units above that for TFA, giving much poorer HPLC resolution due to peak broadening. Difluoroacetic acid has been used as a compromise; the resulting HPLC performance is almost as good as that of TFA, but ion suppression is nearly as poor as that of TFA. Polymer particles avoid this problem, but their high compressibility precludes a small-particle format.

A new type of bonded phase enables RPLC to be performed for mAbs at neutral pH, i.e., native RPLC (52). This was used to separate intact antibody-drug conjugates and perform mass spectrometry without the use of TFA. The bonded phase is a polymer grown on silane initiators by atom-transfer radical polymerization, which provides a thick barrier between the protein and the silica surface (53). This combines the incompressibility of silica particles with the ability of polymer surfaces to be used without TFA, allowing high-sensitivity mass spectrometry. The future could bring other new types of bonded phases for better compatibility with mass spectrometry.



#### 4. CONCLUDING REMARKS

We have seen a big advance in HPLC approximately every decade. In the 1960s it was silanes as molecularly thin, covalently bonded phases that did not wash away. In the 1970s it was 5- $\mu\text{m}$  particles for higher efficiency. Type B silica to allow efficient protein separations marked the 1980s (54). In the 1990s, LC-MS of proteins had become possible, and in the 2000s, sub-2- $\mu\text{m}$  particles became available for faster separations. Today, it is fused-core particles with 1,000-Å pores that have markedly improved resolution in protein chromatography. The one thing that has remained constant over the half century of HPLC is that an understanding of the fundamental principles enables people to think more clearly about what the current limitations are, enabling creative and realistic thinking about how to make the next major advance. It will be exciting to see what the next decade, and for many readers, the next half century, will bring.

#### DISCLOSURE STATEMENT

The authors are not aware of any affiliations, memberships, funding, or financial holdings that might be perceived as affecting the objectivity of this review.

#### ACKNOWLEDGMENTS

The writing of this review and some of the experiments discussed herein were supported by the US National Institutes of Health under grant R01 GM121910.

#### LITERATURE CITED

1. Beck A, Wurch T, Bailly C, Corvaia N. 2010. Strategies and challenges for the next generation of therapeutic antibodies. *Nat. Rev. Immunol.* 10:345–52
2. Alley SC, Okeley NM, Senter PD. 2010. Antibody–drug conjugates: targeted drug delivery for cancer. *Curr. Opin. Chem. Biol.* 14:529–37
3. Philippidis A. 2019. Top 15 best-selling drugs of 2018. *Genet. Eng. Biotechnol. News* 39, March 11. <https://www.genengnews.com/a-lists/top-15-best-selling-drugs-of-2018/>
4. Hawkrige AM, Muddiman DC. 2009. Mass spectrometry-based biomarker discovery: toward a global proteome index of individuality. *Annu. Rev. Anal. Chem.* 2:265–77
5. Toby TK, Fornelli L, Kelleher NL. 2016. Progress in top-down proteomics and the analysis of proteoforms. *Annu. Rev. Anal. Chem.* 9:499–519
6. Wei BC, Zhang B, Boyes B, Zhang YT. 2017. Reversed-phase chromatography with large pore superficially porous particles for high throughput immunoglobulin G<sup>2</sup> disulfide isoform separation. *J. Chromatogr. A* 1526:104–11
7. Kim E. 2008. *Rapid resolution—practical considerations—series 6. LC columns and consumables*. Presented at Agilent Technologies, May 14. Agilent Technol., Santa Clara, CA. [https://www.agilent.com/cs/library/eseminars/public/Rapid\\_Resolution\\_Practical\\_Considerations.pdf](https://www.agilent.com/cs/library/eseminars/public/Rapid_Resolution_Practical_Considerations.pdf)
8. Du Y, Walsh A, Ehrick R, Xu W, May K, Liu HC. 2012. Chromatographic analysis of the acidic and basic species of recombinant monoclonal antibodies. *MAbs* 4:578–85
9. Hilliard M, Alley WR, McManus CA, Yu YQ, Hallinan S, et al. 2017. Glycan characterization of the NIST RM monoclonal antibody using a total analytical solution: from sample preparation to data analysis. *MAbs* 9:1349–59
10. Neergaard MS, Nielsen AD, Parshad H, Van de Weert M. 2014. Stability of monoclonal antibodies at high-concentration: head-to-head comparison of the IgG<sub>1</sub> and IgG<sub>4</sub> subclass. *J. Pharm. Sci.* 103:115–27
11. Smith LM, Kelleher NL. 2018. Proteoforms as the next proteomics currency. *Science* 359:1106–7
12. Gritti F, Guiochon G. 2013. The van Deemter equation: assumptions, limits, and adjustment to modern high performance liquid chromatography. *J. Chromatogr. A* 1302:1–13



13. Snyder LR, Stadalius MA, Quarry MA. 1983. Gradient elution in reversed-phase HPLC separation of macromolecules. *Anal. Chem.* 55:1412–30
14. Gritti F. 2016. General theory of peak compression in liquid chromatography. *J. Chromatogr. A* 1433:114–22
15. Wu NJ, Liu YS, Lee ML. 2006. Sub-2  $\mu\text{m}$  porous and nonporous particles for fast separation in reversed-phase high performance liquid chromatography. *J. Chromatogr. A* 1131:142–50
16. de Villiers A, Lestremieu F, Szucs R, Gélébart S, David F, Sandra P. 2006. Evaluation of ultra performance liquid chromatography: part I. Possibilities and limitations. *J. Chromatogr. A* 1127:60–69
17. Schure MR, Maier RS, Kroll DM, Davis HT. 2004. Simulation of ordered packed beds in chromatography. *J. Chromatogr. A* 1031:79–86
18. De Vos J, Broeckhoven K, Eeltink S. 2016. Advances in ultrahigh-pressure liquid chromatography technology and system design. *Anal. Chem.* 88:262–78
19. Farkas T, Guiochon G. 1997. Contribution of the radial distribution of the flow velocity to band broadening in HPLC columns. *Anal. Chem.* 69:4592–600
20. Patel KD, Jerkovich AD, Link JC, Jorgenson JW. 2004. In-depth characterization of slurry packed capillary columns with 1.0- $\mu\text{m}$  nonporous particles using reversed-phase isocratic ultrahigh-pressure liquid chromatography. *Anal. Chem.* 76:5777–86
21. Wei BC, Malkin DS, Wirth MJ. 2010. Plate heights below 50 nm for protein electrochromatography using silica colloidal crystals. *Anal. Chem.* 82:10216–21
22. Zhang Z, Wu Z, Wirth MJ. 2013. Polyacrylamide brush layer for Hydrophilic Interaction Liquid Chromatography of intact glycoproteins. *J. Chromatogr. A* 1301:156–61
23. Knox JH, McLaren L. 1964. A new gas chromatographic method for measuring gaseous diffusion coefficients and obstructive factors. *Anal. Chem.* 36:1477–82
24. Miyabe K, Guiochon G. 2010. Surface diffusion in reversed-phase liquid chromatography. *J. Chromatogr. A* 1217:1713–34
25. Weissberg HL. 1963. Effective diffusion coefficient in porous media. *J. Appl. Phys.* 34:2636
26. Maxwell JC. 1873. *A Treatise on Electricity and Magnetism*. Oxford, UK: Clarendon
27. Rogers BJ, Wirth MJ. 2013. Obstructed diffusion in silica colloidal crystals. *J. Phys. Chem. A* 117:6244–49
28. Yan X, Wang Q. 2013. Numerical investigation into the effects of ordered particle packing and slip flow on the performance of chromatography. *J. Sep. Sci.* 36:1524–29
29. Wirth MJ, Fairbank RWP, Fatunmbi HO. 1997. Mixed self-assembled monolayers in chemical separations. *Science* 275:44–47
30. Rogers BJ, Birdsall RE, Wu Z, Wirth MJ. 2013. RPLC of intact proteins using sub-0.5  $\mu\text{m}$  particles and commercial instrumentation. *Anal. Chem.* 85:6820–25
31. Wei B, Rogers BJ, Wirth MJ. 2012. Slip flow in colloidal crystals for ultraefficient chromatography. *J. Am. Chem. Soc.* 134:10780–82
32. Giddings JC. 1991. *Unified Separation Science*. New York: Wiley Intersci.
33. Bird RB, Stewart WE, Lightfoot EN. 2007. *Transport Phenomena*. New York: John Wiley & Sons. 2nd ed.
34. Navier CLMH. 1823. Mémoire sur les lois du mouvement des fluides. *Mem. Acad. Sci. Inst. France* 6:389–440
35. Rogers BJ, Wirth MJ. 2013. Slip flow through colloidal crystals of varying particle diameter. *ACS Nano* 7:725–31
36. Horváth C, Lin IJJ. 1978. Band spreading in liquid-chromatography: general plate height equation and a method for evaluation of individual plate height contributions. *J. Chromatogr.* 149:43–70
37. Fekete S, Fekete J, Guillaume D. 2014. Estimation of the effects of longitudinal temperature gradients caused by frictional heating on the solute retention using fully porous and superficially porous sub-2  $\mu\text{m}$  materials. *J. Chromatogr. A* 1359:124–30
38. Makarov AA, Schafer WA, Helmy R. 2015. Use of pressure in reversed-phase liquid chromatography to study protein conformational changes by differential deuterium exchange. *Anal. Chem.* 87:2396–402
39. de Villiers A, Lauer H, Szucs R, Goodall S, Sandra P. 2006. Influence of frictional heating on temperature gradients in ultra-high-pressure liquid chromatography on 2.1 mm ID columns. *J. Chromatogr. A* 1113:84–91

